On transport properties of Majorana fermions in superconductors: free & interacting

Gnezdilov, N.V.

On transport properties of Majorana fermions in superconductors: free & interacting

Proefschrift

ter verkrijging van
de graad van Doctor aan de Universiteit Leiden,
op gezag van Rector Magnificus prof. mr. C.J.J.M. Stolker,
volgens besluit van het College voor Promoties
te verdedigen op woensdag 12 Juni 2019
klokke 15.00 uur

door

Nikolay Vladislavovich Gnezdilov

geboren te Novosibirsk, Rusland in 1991

Promotores: Prof. dr. C. W. J. Beenakker
Prof. dr. S. I. Mukhin (National University of Science and Technology, Moscow, Russia)

Promotiecommissie: Dr. A. R. Akhmerov (TU Delft)
Prof. dr. A. Brinkman (Universiteit Twente)
Dr. A. Boyarski
Prof. dr. E. R. Eliel
Prof. dr. H. Schiessel

Casimir PhD Series Delft-Leiden 2019-19
ISBN 978-90-8593-405-9
An electronic version of this thesis can be found at `https://openaccess.leidenuniv.nl`

Front cover: Spectral function of the SYK impurity lattice with the lines of zeros. Chiral Majorana mode propagating along the edge of a two-dimensional topological superconductor, with a graphene fragment in the lower left corner. Back cover: Tunneling spectroscopy of a black hole chip (SYK quantum dot), on the background of a graph of the low-high voltage duality derived in this thesis. The author's name is tilted representing the "rotating" Holstein-Primakoff approach proposed in this thesis.

To my parents.
Моим родителям.

Contents

Chapter 1

Introduction

1.1 Preface

Majorana fermions are *charge neutral* fermionic modes that equal their own antiparticles [1] and originate from a real solution of the complex Dirac equation [2]. Those recently attracted a lot of attention in the context of subgap states in superconductors [3–11]. In superconducting systems, oppositely charged electron and hole quasiparticle excitations can be naturally thought as particle-antiparticle partners. The particle-hole symmetry relates the creation operator of the quasiparticle excitation $\gamma_E^\dagger$ at energy E to its annihilation operator γ_{-E} at the opposite energy. The p-wave superconducting pairing allows for the subgap solutions of the Bogoliubov-De Gennes (BdG) Hamiltonian at $E = 0$ on vortices in two dimensions [3–5, 8] or as the bound states at the ends of a one-dimensional nanowire [6, 9], which makes the superconductor *topologically non-trivial* [10, 12]. These solutions realize Majorana zero modes $\gamma_0^\dagger = \gamma_0$ (often referred to as Majoranas) that obeys the anticommutation relation $\{\gamma_i, \gamma_j\} = 2\delta_{ij}$. It follows from the reality of Majorana zero modes ($\gamma_i^\dagger = \gamma_i$) that *two* of those are needed to encode a *single* complex fermion, so that each Majorana enters as an *equal-weight superposition* of the electron and hole excitations. This results in 2^N degeneracy of the ground state described by $2N$ Majoranas, non-Abelian exchange statistic of the latter ones [4, 5, 13], and makes them especially attractive in the perspective of topological quantum computation [6, 14, 15].

Once Majorana zero modes are stacked together with sufficient overlap, they form a subgap chiral edge Majorana mode. The left panel in Fig.

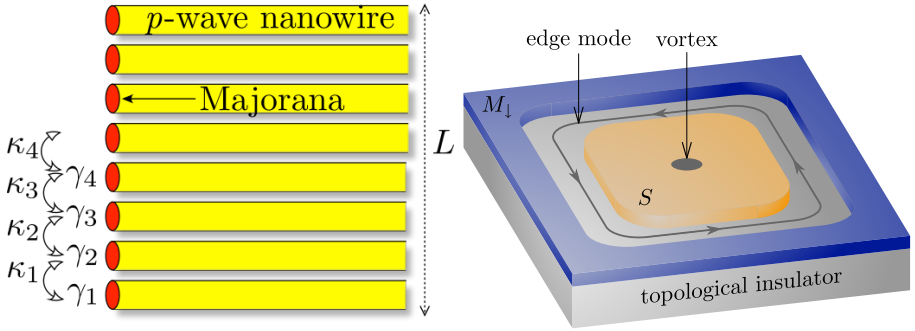

Figure 1.1. *Left panel*: A stack of superconducting nanowires [6] that form a dispersive (see Fig. 1.2) Majorana subgap edge state. The figure is taken from M. Diez, I. C. Fulga, D. I. Pikulin, J. Tworzydło, and C. W. J. Beenakker, New Journal of Physics **16**, 063049 (2014). *Right panel*: 3D topological insulator in proximity to superconductor and ferromagnet hosts Majorana edge mode. The figure is reprinted with permission from A. R. Akhmerov, Johan Nilsson, and C. W. J. Beenakker, Phys. Rev. Lett. **102**, 216404 (2009). Copyright 2009 by the American Physical Society.

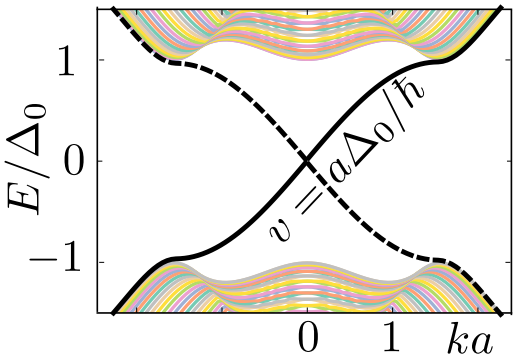

Figure 1.2. Dispersion of a chiral p-wave superconductor drawn from the tight-binding model defined on the infinite stripe geometry (lattice constant a). The bulk of the system is gapped, while the Majorana edge states have the linear dispersion with a slope proportional to the bulk gap Δ_0.

1.1 schematically shows an array of p-wave nanowires [6] that hosts a Majorana edge state. Also, a surface of a three-dimensional topological insulator [10, 16–18] in proximity to superconductor and ferromagnet is predicted to form a Majorana edge mode along the boundary between a ferromagnet and superconductor [19, 20], as it is shown in the right panel

of Fig. 1.1. Moreover, Majorana edge modes at the interface between quantum anomalous Hall insulator and an s-wave superconductor [21] have been recently reported to be observed in experiment [22].

Chiral Majorana edge states in p-wave superconductors with a spin-triplet $p_x + ip_y$ pair potential [4, 7], whose dispersion is shown in Fig 1.2, can be thought as a superconducting analog of chiral edge modes of the quantum Hall effect. However, because Majorana fermions are charge neutral, quantized electrical signatures of the Majorana edge mode are lacking. On the other hand, a temperature gradient is predicted to drive a heat current along the edge carried by Majorana fermions, so that the thermal conductance G is quantized at the electronic quantum $G_0 = \pi^2 k_B^2 T/3h$ times one-half.[1] Study of electrical alternatives to the heat conductance measurements is the goal of Chapters 2 and 3.

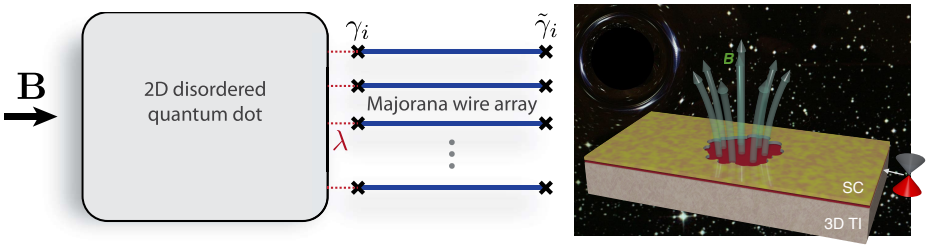

Figure 1.3. *Left panel*: An array of the superconducting nanowires in the magnetic field strongly coupled through a disordered quantum dot. The figure is reprinted with permission from Aaron Chew, Andrew Essin, and Jason Alicea, Phys. Rev. B **96**, 121119(R) (2017). Copyright 2017 by the American Physical Society. *Right panel*: Disordered surface of 3D TI in proximity to a s-wave superconductor in the magnetic field. The figure is reprinted with permission from D. I. Pikulin and M. Franz, Phys. Rev. X **7**, 031006 (2017). Copyright 2017 by the American Physical Society.

The edge states of topological superconductors discussed above are described by the low energy non-interacting theories. In contrast, the second part of the thesis is devoted to the strongly interacting Majorana zero-modes and to the Sachdev-Ye-Kitaev (SYK) model in particular [27, 28]. The interactions are supposed to be so strong, that the quasiparticle description of the model is no longer possible. However, the SYK model is exactly solvable in the large N limit and establishes connections between

[1] The thermal conductance $G = 1/2 \times G_0$ is due to the central charge $c = 1/2$ of the field theory of Majorana edge mode [4, 23–26].

non-Fermi liquids, black hole horizons, and many-body quantum chaos [27, 29, 30].

The SYK model can be realized as a low energy theory of an array of superconducting nanowires in the topological phase [6, 9] once those are strongly coupled through a disordered quantum dot in the magnetic field oriented in the plane of the quantum dot [31]. Additionally, a surface of a three-dimensional topological insulator with an irregular opening in proximity to a superconductor is proposed [32] to be described by the SYK model at low energies (see Fig. 1.3). Chapters 5, 6, and 7 are addressed to direct and indirect transport signatures of the non-quasiparticle nature of the SYK model to characterize these systems.

1.2 Electrical signatures of Majorana surface states

Topological superconductors are analogous to topological insulators [10, 16–18]: Both combine an excitation gap in the bulk with gapless states at the surface, without localization by disorder as long as time-reversal symmetry is preserved. However, the nature of the surface excitations is entirely different: In a topological insulator these are Dirac fermions, relativistic electrons or holes of charge $\pm e$, while a topological superconductor has charge-neutral Majorana fermions on its surface. A transport experiment that aims to detect the Majorana surface states cannot be as routine as electrical conduction — the direct analog for Majorana fermions of the electrical conductance of Dirac fermions is the thermal conductance G_{thermal}. The challenge of low-temperature thermal measurements is one reason why Majorana surface states have not yet been detected in a transport experiment on candidate materials for topological superconductivity [33–37].

There exists a purely electrical alternative to thermal detection of Majorana fermions [38]. Particle-hole symmetry enforces that a Majorana fermion at the Fermi level is an equal-weight electron-hole superposition, so while the average charge is zero, the charge fluctuations have a quantized variance of

$$\operatorname{Var} Q = \tfrac{1}{2}(+e)^2 + \tfrac{1}{2}(-e)^2 = e^2. \tag{1.1}$$

Quantum fluctuations of the charge can be detected electrically in a shot noise measurement. For a single fully transmitted Majorana mode particle hole symmetry enforces a one-to-one relationship between the zero

temperature shot noise power P and the thermal conductance,

$$P/P_0 = G/G_0 = \tfrac{1}{2}\,\mathrm{Tr}\, tt^\dagger, \quad P_0 = e^3V/h, \tag{1.2}$$

where t is the rank-one transmission matrix between two contacts along the edge (biased at voltage $V > 0$, see Fig. 1.4). By definition [2] [39, 40],

$$P = \int_{-\infty}^{\infty} dt\, \langle \delta I(0)\delta I(t)\rangle = \tau^{-1}\,\mathrm{Var}\, Q, \tag{1.3}$$

the shot noise power is the correlator of the current fluctuations and gives the variance of the charge transferred between the contacts in a time τ. Eq. (1.2) implies that $\mathrm{Var}\, Q$ has the universal value $\frac{1}{2}P_0\tau$ for a fully transmitted Majorana mode. These produce a quantized shot noise power P of $\frac{1}{2}e^2/h$ per eV of applied bias [38]. The factor 1/2 reminds us that a Majorana fermion is "half a Dirac fermion".

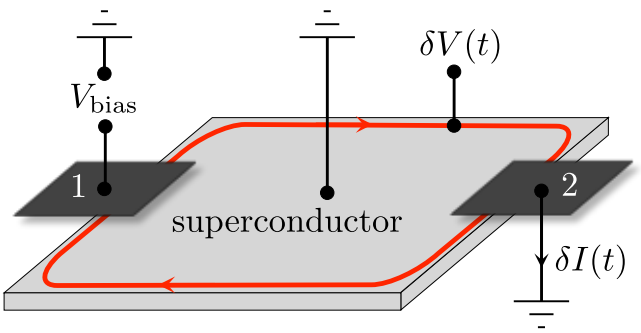

Figure 1.4. Nonlocal current and voltage measurement to detect the charge-neutral Majorana edge mode in a two-dimensional topological superconductor. A bias voltage V excites the edge mode, producing a fluctuating current $\delta I(t)$ and voltage $\delta V(t)$, detected at a remote contact. Because the bulk of the superconductor is grounded, these nonlocal signals are evidence for conduction by gapless edge excitations.

In Chapter 3 of this thesis, we extend the shot noise quantization to the higher moments of charge fluctuations of a single Majorana edge-mode. We explore the relation between the thermal conductance and electrical

[2] The dissipated power in a contact resistance $R = 1/G$, measured in a frequency band width Δf, equals $P_{\mathrm{diss}} = 2RP\Delta f$. To avoid the factor of two, an alternative definition of P has a factor of two in front of the integral in Eq. (1.3). With our definition, the Johnson-Nyquist formula for thermal noise is $P_{\mathrm{thermal}} = 2k_{\mathrm{B}}TG$, while $P_{\mathrm{diss}} = 4k_{\mathrm{B}}T\Delta f$.

shot noise for the *surface* of a three-dimensional topological superconductor in Chapter 2.

1.3 The Sachdev-Ye-Kitaev model in solid state systems

The extreme case of strongly-correlated Majorana zero-modes is under scrutiny in the second part of the thesis. We are going to be focused on the SYK model, which describes N Majoranas with randomized infinite-range interaction in $0+1$ dimensions. It was proposed by Kitaev [27] as a simplified version of the disordered quantum Heisenberg model studied earlier by Sachdev and Ye [28], so that the system would not have a replica symmetry breaking [41, 42] in the large N limit [43, 44]. The SYK Hamiltonian [27, 29, 30] reads

$$H = \frac{1}{4!} \sum_{i,j,k,l=1}^{N} J_{ijkl} \gamma_i \gamma_j \gamma_k \gamma_l \,, \tag{1.4}$$

where γ_i are Majorana zero-modes: $\gamma_i^\dagger = \gamma_i$ and $\{\gamma_i, \gamma_j\} = 2\delta_{ij}$. The couplings J_{ijkl} can be drawn independently from Gaussian distribution with zero mean $\overline{J_{ijkl}} = 0$ and finite variance $\overline{J_{ijkl}^2} = 3!J^2/N^3$.

The SYK model comprises several perculiar properties [27, 29, 30]:

1. it possesses an exact large N solution at *strong* coupling J lacking quasiparticles;

2. emergent conformal symmetry in the infrared;

3. it saturates the upper bound on quantum chaos [45], which is also the case for holographic duals of black hole horizons [46].

Both 1 and 2 can be understood in terms of two-point Green's function found in the long time limit $1 \ll J\tau \ll N$:

$$G(\tau, \tau') = -N^{-1} \sum_{i=1}^{N} \langle \mathcal{T} \gamma_i(\tau) \gamma_i(\tau') \rangle = -\left(4\pi J^2\right)^{-1/4} \frac{\operatorname{sgn}(\tau - \tau')}{\sqrt{|\tau - \tau'|}} \,. \tag{1.5}$$

In frequency representation, the Green's function (1.5) scales as a power-law $1/\sqrt{\omega}$, that has a branch cut rather then quasiparticle like pole struc-

ture. The result (1.5) originates from the solution of a saddle-point equation:

$$J^2 \int d\tau' G(\tau,\tau') G(\tau',\tau'')^3 = -\delta(\tau-\tau'')\,. \tag{1.6}$$

Equation (1.6) remains invariant under time reparametrization $\tau \mapsto f(\tau)$:

$$G(\tau,\tau') \mapsto \left[\partial_\tau f(\tau)\partial_{\tau'} f(\tau')\right]^{\Delta} G\left(f(\tau), f(\tau')\right)\,, \tag{1.7}$$

where $f(\tau)$ is an arbitrary monotonic differentiable function due to the conformal invariance and $\Delta = 1/4$ is an anomalous fermionic scaling dimension [27, 29, 30, 47]. The absence of quasiparticles in the SYK model qualitatively describes the strange metal phase, that exists above the critical temperature in high-T_c superconductors [48, 49], including linear in temperature resistivity in the case of one-dimensional extension of the SYK model [50].

The property of maximal chaos 3 in the SYK model is usually formulated in terms of the so-called Out-Of-Time-Order-Correlation function (OTOC), first introduced by Larkin and Ovchinnikov [51]. It shows how fast the perturbation at time $t = 0$ given by the operator $V(0)$ spreads through the system to influence the later measurement $W(t)$ [45, 52]:

$$F(t) = \mathrm{Tr}\left(\mathrm{e}^{-\beta H}\left[W(t), V(0)\right]^2\right)\,. \tag{1.8}$$

It was recently shown by Maldacena, Shenker, and Stanford [45], that for a many-body quantum system OTOC can not grow faster then exponentially with a characteristic time-scale $t_L \geq \hbar/\left(2\pi k_B T\right)$ known as the Lyapunov time. The SYK model (1.4) is very nonlocal: All degrees of freedom are strongly coupled among each other. This leads to the exponential growth of the OTOC function [27, 29, 30]:

$$\sum_{i,j} \langle \gamma_i(0)\gamma_j(t)\gamma_i(0)\gamma_j(t)\rangle \propto \mathrm{e}^{\lambda_L t}\,, \tag{1.9}$$

that precisely saturates the upper bound on the Lyapunov time $\lambda_L = 1/t_L = 2\pi k_B T/\hbar$ [45]. This is why the SYK model is often refereed as a maximal scrambler.

A possibility to study all these intriguing properties in physical observables inspired a few proposals of realizing the SYK model in a condensed matter platform as a low-energy effective description of an interacting

quantum system [31, 32, 53–55]. The SYK model with Majorana (real) zero-modes is claimed to be a low-energy theory of the Fu-Kane superconductor [8] in a magnetic field with a disordered opening [32], whereas Ref. [31] suggests to use N Majorana nanowires [9] coupled through a disordered quantum dot.

In Ref. [53] Chen *et al* suggested to use a graphene flake to realize the SYK model with the conventional (complex) fermionic zero-modes [3] (cSYK model) [47]:

$$H = \sum_{i,j,k,l=1}^{N} J_{ij;kl}\, c_i^\dagger c_j^\dagger c_k c_l \,, \tag{1.10}$$

where the couplings are hermitian and antisymmetric $J_{ij;kl} = J^*_{kl;ij} = -J_{ji;kl} = -J_{ij;lk}$. Graphene in a perpendicular magnetic field B is known to have Landau levels [57], which are quantized as $E_n \simeq \hbar v\sqrt{2n\, eB/\hbar c}$ with integer n. The 0th Landau level is degenerate [4] and robust [58] under disorder unless the chiral symmetry is broken. Thus, one gets fermionic zero-modes separated from the higher bands by the gap controlled by the magnetic field. As those are robust under disorder, the authors propose to make the boundary of the flake sufficiently irregular. This would make the wave functions of 0th Landau levels $\Phi_i(\mathbf{r})$ random in the real space. Inclusion of the Coulomb interaction $V(\mathbf{r}-\mathbf{r}')$ would enable one to project the interaction term on the basis of 0th Landau levels, so that the projection is governed by the following overlap:

$$J_{ij;kl} = \int d\mathbf{r} \int d\mathbf{r}'\, \Phi_i^*(\mathbf{r})\Phi_j^*(\mathbf{r}')V(\mathbf{r}-\mathbf{r}')\Phi_k(\mathbf{r})\Phi_l(\mathbf{r}') \,, \tag{1.11}$$

that makes the low-energy theory zero dimensional [5] with the cSYK effective Hamiltonian (1.10). The comparison of the generated overlap to

[3] The features of the SYK model mentioned in Section 1.3 are valid for both models with real (Majorana) and complex fermions. The difference is that for the cSYK model the two-point function (1.5) contains the asymmetry parameter of the non-Fermi liquid [56] if the system is away from the charge neutrality point (chemical potential $\neq 0$). We briefly address this issue in the Appendix of Chapter 5. Another distinction between Dirac and Majorana cases is that the right hand side of the reparametrisation prescription (1.7) for complex fermions is multiplied by $g(\tau)/g(\tau')$, where the function $g(\tau)$ appears because of $U(1)$ gauge invariance [47].

[4] Degeneracy of 0th Landau level is proportional to the amount of magnetic flux that flows through the system.

[5] The system can be thought as a strongly interacting disordered *quantum dot*.

the expected Gaussian distribution is shown in Fig 1.5. It is stated that the cSYK model well describes the low-energy theory of the disordered graphene flake of the characteristic size $l \simeq 0.15$ μm that hosts $N \simeq 100$ zero-modes at field strength $B \sim 20$ T [53]. Another proposal for realization of the cSYK model (1.10) with ultracold gases was made by Danshita *et al* [54]. However, all the proposals require for a large number of stable fermionic zero modes separated from the higher bands with a notable gap, sufficient amount of disorder in the system to randomize the wave functions of the zero-modes in the real space, and dominating two-body interaction to be projected on the basis of zero-modes.

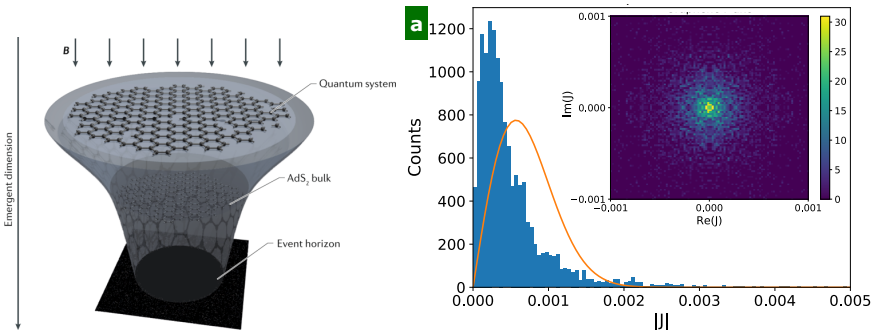

Figure 1.5. *Left panel*: *Holography in a lab.* Strongly interacting disordered graphene quantum dot described by $0+1$-dimensional cSYK model (1.10) at the boundary of $1+1$-dimensional anti-de Sitter space with a black hole [55]. The figure is reprinted by permission from Springer Nature: Marcel Franz and Moshe Rozali, Nature Reviews Materials **3**, 491–501 (2018). Copyright 2018 by Springer Nature. *Right panel*: Statistics of the effective coupling $J_{ij;jk}$ (1.11) for the disordered graphene flake. The figure is reprinted with permission from Anffany Chen, R. Ilan, F. de Juan, D. I. Pikulin, and M. Franz, Phys. Rev. Lett. **121**, 036403 (2018). Copyright 2018 by the American Physical Society.

To characterize the "black hole on a chip" discussed in Refs. [31, 32, 53] propose to measure the local density of states of the SYK quantum dot in a tunneling spectroscopy. The differential tunneling conductance at weak coupling

$$G = \frac{dI}{dV} \propto \mathrm{Im}G^R(V) \propto V^{-1/2} \tag{1.12}$$

reproduces the scaling of the SYK saddle-point solution (1.5) for the voltages in the range of $J/N \ll V \ll J$. The scaling of the differential

conductance (1.5) reveals the emergent conformal symmetry of the SYK model.

1.4 This thesis

Bellow, I briefly highlight the main results presented in the thesis.

1.4.1 Chapter 2

In the first chapter we compare the thermal conductance G_{thermal} (at temperature T) and the electrical shot noise power P_{shot} (at bias voltage $V \gg k_{\text{B}}T/e$) of Majorana fermions on the two-dimensional surface of a three-dimensional topological superconductor. We present analytical and numerical calculations to demonstrate that, for a local coupling between the superconductor and metal contacts, $G_{\text{thermal}}/P_{\text{shot}} = \mathcal{L}T/eV$ (with $\mathcal{L}$ the Lorenz number). This relation is ensured by the combination of electron-hole and time-reversal symmetries, irrespective of the microscopics of the surface Hamiltonian, and provides for a purely electrical way to detect the charge-neutral Majorana surface states. A surface of aspect ratio $W/L \gg 1$ has the universal shot-noise power $P_{\text{shot}} = (W/L) \times (e^2/h) \times (eV/2\pi)$.

1.4.2 Chapter 3

It was found in Ref. [38], that the Majorana fermions propagating along the edge of a topological superconductor with $p_x + ip_y$ pairing deliver a shot noise power of $\frac{1}{2} \times e^2/h$ per eV of voltage bias. In this chapter we calculate the full counting statistics of the transferred charge and find that it becomes trinomial in the low-temperature limit, distinct from the binomial statistics of charge-e transfer in a single-mode nanowire or charge-$2e$ transfer through a normal-superconductor interface. All even-order correlators of current fluctuations have a universal quantized value, insensitive to disorder and decoherence. These electrical signatures are experimentally accessible, because they persist for temperatures and voltages large compared to the Thouless energy.

1.4.3 Chapter 4

There exists an analogy of topological superconductors reveals while considering graphene superlattice shown in Fig. 1.6. Dirac electrons in

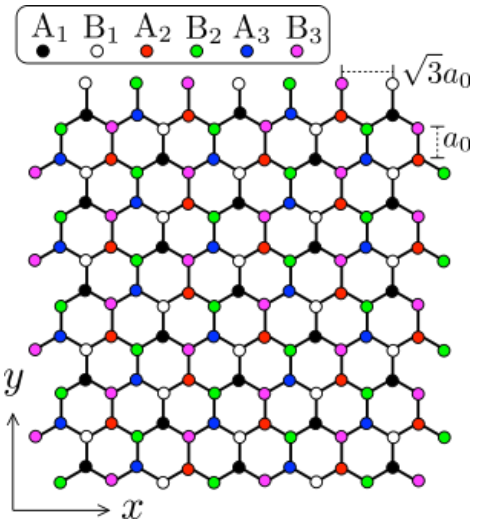

Figure 1.6. Graphene superlattice with a periodic potential modulation. Different colors distinguish the carbon atoms on the A and B sublattice, each of which has an ionic potential V_{A_n}, V_{B_n}, $n = 1, 2, 3$, induced by the substrate.

graphene have a valley degree of freedom that is being explored as a carrier of information. In that context of "valleytronics" one seeks to coherently manipulate the valley index. In this chapter we show that reflection from a superlattice potential can provide a valley switch: Electrons approaching a pristine-graphene–superlattice-graphene interface near normal incidence are reflected in the opposite valley. We identify the topological origin of this valley switch, by mapping the problem onto that of Andreev reflection from a topological superconductor, with the electron-hole degree of freedom playing the role of the valley index. The valley switch is ideal at a symmetry point of the superlattice potential, but remains close to 100% in a broad parameter range.

1.4.4 Chapter 5

In this chapter we study how the non-Fermi liquid behavior of the closed system in equilibrium manifests itself in an open system out of equilib-

rium. We calculate the current-voltage characteristic of a quantum dot, described by the complex-valued SYK model, coupled to a voltage source via a single-channel metallic lead (coupling strength Γ). A one-parameter scaling law appears in the large-N conformal regime, where the differential conductance $G = dI/dV$ depends on the applied voltage only through the dimensionless combination $\xi = eVJ/\Gamma^2$. Low and high voltages are related by the duality $G(\xi) = G(\pi/\xi)$. This provides for an unambiguous signature of the conformal symmetry in tunneling spectroscopy.

1.4.5 Chapter 6

We study the observable properties of quantum systems which involve a quantum continuum as a subpart. We show in a very general way that in any system, which consists of at least two isolated states coupled to a continuum, the spectral function of one of the states exhibits an isolated zero at the energy of the other state. Several examples of quantum systems exhibiting such isolated zeros are discussed. Although very general, this phenomenon can be particularly useful as an indirect detection tool for the continuum spectrum in the lab realizations of quantum critical behavior.

1.4.6 Chapter 7

In this chapter we demonstrate that a single fermion quantum dot acquires odd-frequency Gor'kov anomalous averages in proximity to strongly correlated Majorana zero-modes, described by the SYK model. Despite the presence of finite anomalous pairing, superconducting gap vanishes for the intermediate coupling strength between the quantum dot and Majoranas. The increase of the coupling leads to smooth suppression of the original quasiparticles.

1.4.7 Chapter 8

In the last chapter we consider another model with infinity ranged interaction. We found analytically a first-order quantum phase transition in a Cooper pair box array of N low-capacitance Josephson junctions capacitively coupled to resonant photons in a microwave cavity. The Hamiltonian of the system maps on the extended Dicke Hamiltonian of N spins 1/2 with infinitely coordinated frustrating interaction. This interaction arises from the gauge-invariant coupling of the Josephson-junction phases

to the vector potential of the resonant photons field. In the $N \gg 1$ semi-classical limit, we found a critical coupling at which the ground state of the system switches to one with a net collective electric dipole moment of the Cooper pair boxes coupled to a super-radiant equilibrium photonic condensate. This phase transition changes from the first to second order if the frustrating interaction is switched off. A self-consistently "rotating" Holstein-Primakoff representation for the Cartesian components of the total superspin is proposed, that enables one to trace both the first- and the second-order quantum phase transitions in the extended and standard Dicke models, respectively.

Chapter 2

Wiedemann-Franz-type relation between shot noise and thermal conduction of Majorana surface states in a three-dimensional topological superconductor

2.1 Introduction

In a two-dimensional (2D) topological superconductor, studied in Ref. [59], there is only a single Majorana edge mode, but a three-dimensional (3D) topological superconductor has a large number N of Majorana surface modes connecting a pair of metal contacts (see Fig. 2.1). In the absence of inter-mode coupling this would give a shot noise power of

$$P_{\rm shot} = \tfrac{1}{2} N \mathcal{T} P_0, \quad P_0 = eV \frac{e^2}{h}, \tag{2.1}$$

The contents of this chapter have been published and reprinted with permission from N. V. Gnezdilov, M. Diez, M. J. Pacholski, and C. W. J. Beenakker, Phys. Rev. B **94**, 115415 (2016).

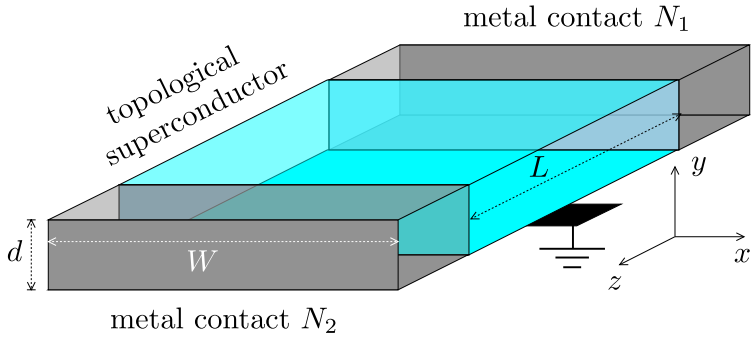

Figure 2.1. Schematic of a superconductor between a pair of normal-metal contacts. The thermal conductance $G_{\text{thermal}} = J/\delta T$ is obtained by applying a temperature difference T, $T+\delta T$ between the contacts and measuring the resulting heat current J. For the shot noise measurement one would bias contact N_1 at voltage V, while keeping the superconductor and N_2 grounded. The electrical current I_2 into contact N_2 fluctuates with noise power P_{shot}. Both $G_{\text{thermal}} \propto T$ and $P_{\text{shot}} \propto V$ are governed by the Majorana surface states of the topological superconductor.

for a mode-averaged transmission probability $\mathcal{T}$. Because the thermal conductance equals [7]

$$G_{\text{thermal}} = \tfrac{1}{2} N \mathcal{T} G_0, \quad G_0 = \mathcal{L} T \frac{e^2}{h}, \tag{2.2}$$

with $\mathcal{L} = \frac{1}{3}(\pi k_{\text{B}}/e)^2$ the Lorenz number, uncoupled Majorana modes have a one-to-one relationship between shot noise and thermal conduction.

We would expect this relationship to break down as a result of intermode scattering: A pair of coupled Majorana modes is equivalent to a single Dirac fermion mode, which can be in an eigenstate of charge at $\operatorname{Var} Q = 0$. The thermal conductance would not be affected, as long as $\mathcal{T}$ remains the same, but P_{shot} would be reduced. Much to our surprise, we discovered in numerical simulations of a 3D topological superconductor that $P_{\text{shot}}/P_0 = G_{\text{thermal}}/G_0$ with high accuracy. This is remarkable even in the absence of any disorder, since the modes at top and bottom surfaces are coupled when they reach the metal contact.

We have found that it is the combination of electron-hole and time-reversal symmetry that preserves the relationship between electrical and thermal conduction in a 3D topological superconductor, provided the conversion from Majorana to Dirac fermions at the metal electrode is local

in space. The general argument is presented in Secs. 2.2 and 2.3. The implication is that the shot noise power has a universal limit

$$P_{\text{shot}} = \frac{1}{2\pi}\frac{W}{L}P_0, \tag{2.3}$$

for a surface of aspect ratio $W/L \gg 1$, with corrections from poor coupling to the metal contacts that we calculate in Secs. 2.4 and 2.5. A numerical test of our analytical predictions for a model Hamiltonian of a 3D topological superconductor is given in Sec. 2.6. We conclude in Sec. 2.7 with a discussion in the context of the Wiedemann-Franz relation between electrical and thermal conduction [60].

2.2 Surface-sensitive thermal and electrical conduction

2.2.1 Description of the geometry

We consider the geometry of Fig. 2.1, a superconductor S connecting two normal-metal contacts N_1 and N_2. The superconductor is topologically nontrivial, with a gapped bulk and a gapless surface. We compare two transport properties, one thermal and one electrical, both sensitive to the surface states.

For thermal transport we take the two-terminal thermal conductance

$$G_{\text{thermal}} = \lim_{\delta T\to 0}\frac{J}{\delta T}, \tag{2.4}$$

giving the heat current J flowing from contact N_1 at temperature $T+\delta T$ to contact N_2 at temperature T, in linear response for $\delta T \ll T$. The superconductor is a thermal insulator in the bulk, because of the excitation gap, but a thermal conductor on the surface, so G_{thermal} measures heat conduction along the surface.

For electrical transport both contacts are kept at the same temperature T. Contact N_1 is biased at voltage V relative to ground, while contact N_2 as well as the superconductor are grounded. Most of the charge current I_1 injected into the superconductor at N_1 is short-circuited to ground via the bulk, which is an ideal electrical conductor. At the remote contact N_2 a fluctuating current $I_2(t)$ remains due to surface conduction from N_1 to

N_2. Even if the time average $\langle I_2 \rangle$ vanishes, there will be time-dependent fluctuations $\delta I_2(t)$ with low-frequency noise power

$$P_{\text{shot}} = \int_{-\infty}^{\infty} dt \, \langle \delta I_2(0) \delta I_2(t) \rangle. \tag{2.5}$$

At low temperatures $k_{\text{B}}T \ll eV$ this is predominantly shot noise $\propto V$.

2.2.2 Scattering formulas

In a scattering formulation the thermal and electrical transport properties can be expressed in terms of the matrix $t(E)$ of transmission amplitudes from N_1 to N_2, at energy E relative to the Fermi level. The transmission matrix has a block structure in the electron-hole degree of freedom,

$$t = \begin{pmatrix} t_{ee} & t_{eh} \\ t_{he} & t_{hh} \end{pmatrix}. \tag{2.6}$$

The submatrix t_{ee} describes transmission of an electron as an electron, while t_{he} describes transmission of an electron as a hole.

At sufficiently small temperature and voltage the transmission matrix may be evaluated at the Fermi level ($E = 0$) and we have the Landauer-type formulas [12, 61, 62]

$$G_{\text{thermal}} = \tfrac{1}{2} G_0 \, \text{Tr} \, t^\dagger t, \tag{2.7}$$

$$P_{\text{shot}} = P_0 \, \text{Tr} \, (\tau_+ - \tau_-^2), \tag{2.8}$$

$$\tau_\pm = t_{ee}^\dagger t_{ee} \pm t_{he}^\dagger t_{he}. \tag{2.9}$$

Eq. (2.8) may equivalently be written in terms of the full transmission matrix,

$$P_{\text{shot}}/P_0 = \tfrac{1}{2} \, \text{Tr} \, (1 + \tau_z) t^\dagger t - \tfrac{1}{4} \, \text{Tr} \left[(1 + \tau_z) t^\dagger \tau_z t \right]^2, \tag{2.10}$$

with the help of the Pauli matrix $\tau_z = \left(\begin{smallmatrix} 1 & 0 \\ 0 & -1 \end{smallmatrix}\right)$ acting on the electron-hole degree of freedom.

2.2.3 Electron-hole symmetry enforced upper bound on the shot noise power

Electron-hole symmetry at the Fermi level equates

$$t = \tau_x t^* \tau_x, \tag{2.11}$$

with $\tau_x = \left(\begin{smallmatrix} 0 & 1 \\ 1 & 0 \end{smallmatrix}\right)$ the Pauli matrix that exchanges electrons and holes. It follows that

$$\begin{aligned} \operatorname{Tr} \tau_z t^\dagger t &= \tfrac{1}{2} \operatorname{Tr} \left(t \tau_z t^\dagger + t^* \tau_z t^{\mathrm{T}} \right) \\ &= \tfrac{1}{2} \operatorname{Tr} \left(t \tau_z t^\dagger + \tau_x t \tau_x \tau_z \tau_x t^\dagger \tau_x \right) = 0. \end{aligned} \tag{2.12}$$

Eqs. (2.7) and (2.10) can therefore be combined into

$$\begin{aligned} P_{\mathrm{shot}}/P_0 &= G_{\mathrm{thermal}}/G_0 - \delta p, \\ \delta p &= \tfrac{1}{4} \operatorname{Tr} \left[(1+\tau_z) t^\dagger \tau_z t \right]^2. \end{aligned} \tag{2.13}$$

Since $(1+\tau_z)^2 = 2(1+\tau_z)$ the term δp can be written as the trace of a positive definite matrix,

$$\delta p = \operatorname{Tr} X^2 \geq 0, \quad X = \tfrac{1}{4}(1+\tau_z) t^\dagger \tau_z t (1+\tau_z) = X^\dagger, \tag{2.14}$$

so the dimensionless shot noise power P_{shot}/P_0 is bounded from above by the dimensionless thermal conductance G_{thermal}/G_0.

In Ref. [38] it was demonstrated that this inequality becomes a strict *equality* for a rank-one transmission matrix t, as in 1D transmission via the unpaired Majorana edge mode of a 2D topological superconductor [59, 63]. Only particle-hole symmetry is needed in that case. In the next section we will show that the combination of particle-hole symmetry and time-reversal symmetry achieves approximate equality on the 2D surface of a 3D topological superconductor, irrespective of the rank of t.

2.3 Combined effects of electron-hole and time-reversal symmetries on the shot noise power

2.3.1 Surface Hamiltonian with tunnel coupling to metal contacts

The surface Hamiltonian of Majorana fermions in the x–z plane has the form [64]

$$H = v p_x \sigma_x + v p_z \sigma_z, \tag{2.15}$$

with velocity v, momentum operators $p_\alpha = -i\partial/\partial x_\alpha$, and Pauli matrices σ_α acting on the spin degree of freedom. (The 2×2 unit matrix is σ_0 and we have set $\hbar$ to unity.) We assume that there is no valley degeneracy of the

surface states, so the surface spectrum consists of a single nondegenerate cone with dispersion relation $E^2 = v^2 p^2$.

A disorder potential $V(x,z)\sigma_\alpha$ is forbidden by the combination of electron-hole symmetry and time-reversal symmetry,

$$H = -H^*, \quad H = \sigma_y H^* \sigma_y. \tag{2.16}$$

This insensitivity to impurity scattering is a unique property of a topological superconductor in symmetry class DIII [1] [65, 66]. A spatial modulation of the Fermi velocity $v(x,z)$ is allowed by symmetry [67], and this is the only source of scattering on the surface.

The normal metal has propagating modes labeled by a spin degree of freedom σ, electron-hole degree of freedom τ, and orbital degree of freedom ν. The superconducting surface has only evanescent modes at the Fermi level, because of the vanishing density of states. A Majorana fermion with spin σ' at point $\boldsymbol{r}$ is coupled to the metal by the coupling matrix element $\langle \sigma', \boldsymbol{r}|\Xi|\sigma,\tau,\nu\rangle$. The scattering matrix is given by [68]

$$S(E) = 1 + i\,\Xi^\dagger (H - \tfrac{1}{2} i\,\Xi\Xi^\dagger - E)^{-1}\Xi, \tag{2.17}$$

near the Fermi level where the energy dependence of the coupling matrix Ξ can be neglected.

The scattering matrix is unitary, $SS^\dagger = S^\dagger S = 1$, with electron-hole and time-reversal symmetries [2]

$$S(E) = \tau_x S^*(-E)\tau_x, \quad S(E) = \sigma_y S^{\mathrm{T}}(E)\sigma_y. \tag{2.18}$$

The corresponding symmetry relations for the coupling matrix are

$$\Xi = \Xi^* \tau_x, \quad \Xi = \sigma_y \Xi^* \sigma_y. \tag{2.19}$$

[1] Symmetry class DIII refers to a superconductor with broken spin-rotation symmetry. Class-CI superconductors with preserved spin-rotation symmetry may also host gapless surface states, but these are Dirac fermions rather than Majorana fermions and do not have the same protection against disorder scattering.

[2] The symmetry operations (2.18) on the scattering matrix are taken in a time-reversally symmetric basis of the propagating modes in the normal metal. If transverse momentum q is used to label the modes, these operations should be accompanied by $q \mapsto -q$.

2.3.2 Condition on the coupling matrix for equality of shot noise and thermal conductance

We now restrict ourselves to the Fermi level, $E = 0$, and determine a condition on the coupling matrix Ξ that ensures the equality $P_{\text{shot}}/P_0 = G_{\text{thermal}}/G_0$ of the dimensionless shot noise power and thermal conductance. According to Eqs. (2.13) and (2.14), a necessary and sufficient condition is that the electron-electron block X of the transmission matrix product $t^\dagger \tau_z t$ vanishes identically. Here we establish a *sufficient* condition involving only the coupling matrix:

$$\begin{aligned} &\Xi\tau_z\Xi^\dagger \equiv 0 \Rightarrow t^\dagger\tau_z t \equiv 0 \Rightarrow X \equiv 0 \\ &\Leftrightarrow P_{\text{shot}}/P_0 = G_{\text{thermal}}/G_0. \end{aligned} \tag{2.20}$$

No requirements are made on the rank of t, which may involve strong mode-mixing by the surface Hamiltonian.

The combination of the electron-hole and time-reversal symmetries (2.19) implies that

$$\Xi\tau_x = \sigma_y\Xi\sigma_y \Rightarrow \sigma_y\Xi\tau_z\Xi^\dagger = -\Xi\tau_z\Xi^\dagger\sigma_y, \tag{2.21a}$$

$$\Xi\tau_x = \Xi^* \Rightarrow \Xi\tau_z\Xi^\dagger = -(\Xi\tau_z\Xi^\dagger)^{\mathrm{T}}, \tag{2.21b}$$

so the matrix $\Xi\tau_z\Xi^\dagger$ is antisymmetric and it anticommutes with σ_y. Because the only 2×2 matrix with both these properties is identically zero, we conclude that $\Xi\tau_z\Xi^\dagger$ vanishes if it is block-diagonal in 2×2 matrices:

$$\Xi\tau_z\Xi^\dagger = 0 \text{ if } \langle\sigma', \boldsymbol{r}'|\Xi\tau_z\Xi^\dagger|\sigma, \boldsymbol{r}\rangle = \Gamma_{\sigma\sigma'}(\boldsymbol{r})\delta(\boldsymbol{r}-\boldsymbol{r}'). \tag{2.22}$$

The 2×2 matrix $\Gamma(\boldsymbol{r})$ acts on the spin degree of freedom of a Majorana fermion at position $\boldsymbol{r}$ on the superconducting surface. We will refer to the condition (2.22) as a *locality condition* on the coupling matrix product $\Xi\tau_z\Xi^\dagger$.

In the next section we will explicitly solve a simple model where the locality condition holds, but we argue that it is a natural assumption for a weakly disordered NS interface between the normal metal (N) and the topological superconductor (S). If the disorder mean free path is large compared to the superconducting coherence length, a Majorana fermion transmitted through the NS interface is locally converted into an electron-hole superposition via a 2×4 matrix K and then scattered nonlocally in the normal metal via a unitary matrix U without mixing electrons and holes — so U commutes with τ_z and $U\tau_z U^\dagger = \tau_z$. Substitution of $\Xi = KU$ gives the desired locality to $\Xi\tau_z\Xi^\dagger = K\tau_z K^\dagger$.

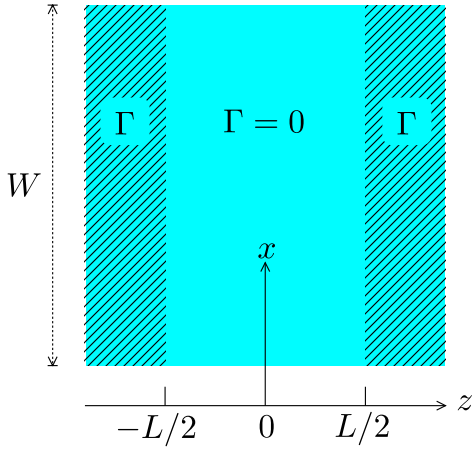

Figure 2.2. Superconducting surface layer in the x–z plane with tunnel coupling to a normal-metal in the region $|z| > L/2$ (shaded, tunnel rate Γ). This 2D scattering geometry effectively describes the transmission from N_1 to N_2 via the top or bottom surface of the 3D topological superconductor in Fig. 2.1. The extension d of the contact region is assumed to be sufficiently large that top and bottom surfaces can be treated independently. (Coupling of top and bottom surfaces is described in Fig. 2.3.)

2.4 Formulation and solution of the surface scattering problem

2.4.1 Reduction to an effectively 2D geometry

The transmission matrix t refers to a 3D scattering problem, and this is how we will calculate it numerically later on. For an analytical treatment a reduction to an effectively 2D geometry is desirable. Referring to Fig. 2.1, in a typical thin-film geometry one has $d \ll W$, so the contributions from the top and bottom surfaces in the x–z plane dominate over the contributions from the lateral surfaces in the y–z plane.

The normal-metal contact region in the x–y plane is connected to the superconducting surface in the x–z plane at $z = \pm L/2$. We ignore the curvature of the surface at this connection and replace the contact region by the region $|z| > L/2$ in the x–z plane. Tunneling into the metal electrode in the contact region is described by the effective Hamiltonian

$$\mathcal{H} = H - \tfrac{1}{2} i\Gamma(z)\sigma_0, \quad \Gamma(z) = \Gamma\theta(|z| - L/2), \tag{2.23}$$

with $\theta(s)$ the unit step function. If the tunnel barrier is sufficiently transparent (tunnel rate $\Gamma \gg v/d$), a particle approaching $z = \pm L/2$ via the top surface ($y = d/2$) will enter the metal contact before reaching the bottom surface ($y = -d/2$), so that we can treat top and bottom surfaces separately. This produces the effectively 2D geometry of Fig. 2.2, which we will analyze in the next subsection. The regime $\Gamma \lesssim v/d$, when top and bottom surfaces cannot be treated separately, is considered in Sec. 2.4.3.

2.4.2 Single-surface transmission matrix

The normal metal has a nonzero density of states at the Fermi level, with a set of M transverse momenta q (in the x-direction). At each q there are four propagating modes, including the spin and electron-hole degree of freedom. We collect the total number of $4M$ mode indices in the label α, with Pauli matrices σ_i, τ_i acting, respectively, on the spin and electron-hole degree of freedom. The scattering matrix element $S_{\alpha\alpha'}(z, z'; E)$ at energy E relates an outgoing mode α at z to an incoming mode α' at z'.

The full $4M \times 4M$ scattering matrix $S(z, z'; E)$ describes both transmission (when $z > L/2$ and $z' < -L/2$ or the other way around) and reflection (when $z, z' > L/2$ or $z, z' < -L/2$). In accord with Eq. (2.17) it is given by

$$S(z, z'; E) = \mathbb{1}\delta(z - z') + i\Gamma W^\dagger(z)\mathcal{G}(z, z'; E)W(z'), \tag{2.24}$$

in terms of a $2M \times 2M$ matrix Green's function $\mathcal{G}(z, z'; E)$,

$$(\mathcal{H} - E)\mathcal{G}(z, z'; E) = \mathbb{1}\delta(z - z'), \tag{2.25}$$

and a $2M \times 4M$ coupling matrix $W(z)$. The rank of the matrix $\mathcal{G}$ is only half the rank of S, because the Majorana fermions on the superconducting surface lack the electron-hole degree of freedom of the Dirac fermions in the normal metal. [3]

Particle conservation (unitarity) requires that

$$\int_{|z''|>L/2} dz''\, S(z, z''; E)S^\dagger(z', z''; E) = \mathbb{1}\delta(z - z'), \tag{2.26}$$

[3] The factor of two difference between the number of independent modes in the normal metal and the superconductor is the reason that the mode-matching approach of Ref. [69] cannot be applied here.

for $|z|, |z'| > L/2$, which is satisfied if

$$W(z)W^\dagger(z) = \mathbb{1}. \tag{2.27}$$

Although in the general treatment of the previous section we allowed for mode-mixing on the superconducting surface, for a tractable analytical calculation we now simplify to the Hamiltonian (2.15) with a uniform velocity v. Because other sources of scattering are excluded by the combination of electron-hole and time-reversal symmetry, the transverse momentum q is not coupled by the effective Hamiltonian (2.23) and $\mathcal{G}$ decomposes into 2×2 q-dependent blocks $\mathcal{G}(z, z'; q, E)$.

This matrix Green's function is calculated in Appendix 2.8.1. To obtain the transmission matrix from N_1 to N_2 we must take $z > L/2$ and $z' < -L/2$. At the Fermi level the result is

$$\mathcal{G}(z, z'; q, 0) = \frac{1}{2iv} \frac{\exp[-\xi(z - z' - L)]}{\xi \cosh Lq + q \sinh Lq} \begin{pmatrix} -\xi - \kappa & iq \\ iq & \xi - \kappa \end{pmatrix}, \tag{2.28a}$$

$$\xi = \sqrt{q^2 + \kappa^2}, \;\; \kappa = \tfrac{1}{2}\Gamma/v, \;\; z > L/2, \;\; z' < -L/2. \tag{2.28b}$$

The $4M \times 4M$ transmission matrix $t(z, z')$ at the Fermi level follows from Eq. (2.24),

$$\begin{aligned} t(z, z') &= \sum_q t(z, z'; q), \\ t(z, z', q) &= i\Gamma w^\dagger(z, q) \mathcal{G}(z, z'; q, 0) w(z', q), \end{aligned} \tag{2.29}$$

with a q-dependent $2 \times 4M$ coupling matrix $w(z, q)$. The unitarity constraint reads

$$w(z, q) w^\dagger(z, q') = \delta_{qq'} \sigma_0. \tag{2.30}$$

2.4.3 Transmission matrix for coupled top and bottom surfaces

The approach outlined above for the case of uncoupled top and bottom surfaces can be readily generalized to allow for a coupling of the two surfaces via the contact region. In the effective 2D representation the region of nonzero Γ now extends over a finite interval,

$$\Gamma(z) = \Gamma \left[\theta(|z| - L/2) - \theta(|z| - L/2 - d) \right]. \tag{2.31}$$

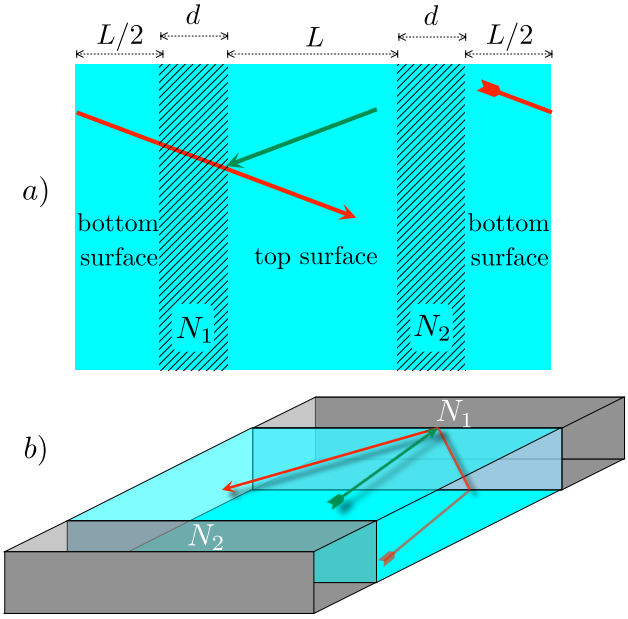

Figure 2.3. Panel a: Same as Fig. 2.2, but now with antiperiodic boundary conditions at $z = \pm(L + d)$ to include the effect of a coupling of top and bottom surface via the contact region of finite length d. Panel b shows the correspondence between trajectories in the 2D and 3D representation. Coupling of the red and green trajectories, at the same transverse momentum q, elevates the rank of the q-dependent transmission matrix from one to two.

A particle on the top surface crossing the contact region without being absorbed continues on the bottom surface. The corresponding 2D geometry is shown in Fig. 2.3. It has a finite extent $2L + 2d$ in the z-direction, with antiperiodic boundary conditions at $z = \pm(L + d)$ to account for a π Berry phase.

The calculation of the Green's function is given in Appendix 2.8.2. Instead of Eq. (2.28) we now have

$$\mathcal{G}(z, z'; q, 0) = \frac{1}{2iv} \frac{\cosh \xi s}{\xi \cosh Lq \cosh \xi d + q \sinh Lq \sinh \xi d} \times \begin{pmatrix} -\xi - \kappa \tanh \xi s & iq \tanh \xi s \\ iq \tanh \xi s & \xi - \kappa \tanh \xi s \end{pmatrix}, \tag{2.32a}$$

$$s = L + d - z + z' \in (-d, d),$$
$$-L/2 - d < z' < -L/2, \quad L/2 < z < L/2 + d. \tag{2.32b}$$

The single-layer result (2.28) is recovered in the limit $d \to \infty$.

The key distinction between the single-surface Green's function (2.28) and the coupled-surface result (2.32) is that — while both are 2×2 matrices — the latter is of rank two but the former is only of rank one (one of the two eigenvalues of the matrix (2.28) vanishes).

2.5 Thermal conductance and corresponding shot noise power

We use the 2D surface theory of the previous section to calculate the thermal conductance $G_{\rm thermal}$, including the effects of poor coupling to the metal contacts, strong coupling of top and bottom surfaces, and effects of a finite aspect ratio. Subject to the locality condition (2.22) these results apply as well to the shot noise power $P_{\rm shot} = G_{\rm thermal} \times P_0/G_0$.

2.5.1 Single surface

The thermal conductance (2.7) follows from the transmission matrix (2.29) upon integration,

$$G_{\rm thermal} = \tfrac{1}{2} G_0 \int_{L/2}^{\infty} dz \int_{-\infty}^{-L/2} dz' \,{\rm Tr}\, t^\dagger(z,z') t(z,z'). \tag{2.33}$$

Because of the unitarity condition (2.30) the coupling matrix drops out and only the 2×2 matrix Green's function enters. Substitution of the result (2.28) for a single surface gives

$$\begin{aligned} G_{\rm thermal}/G_0 &= \tfrac{1}{2}\Gamma^2 \sum_q \int_{L/2}^{\infty} dz \int_{-\infty}^{-L/2} dz' {\rm Tr}\, \mathcal{G}^\dagger(z,z';q,0)\mathcal{G}(z,z';q,0) \\ &= \tfrac{1}{2}\kappa^2 \sum_q (\xi \cosh Lq + q \sinh Lq)^{-2}. \end{aligned} \tag{2.34}$$

For $W \gg L$ the sum over transverse momenta may be replaced by an integration, $\sum_q \to (W/2\pi)\int_{-\infty}^{\infty} dq$, resulting in

$$G_{\rm thermal} = G_0 \frac{W}{2\pi} \int_0^{\infty} dq \, \frac{\kappa^2}{(\xi \cosh qL + q \sinh qL)^2}. \tag{2.35}$$

The coupling strength of the superconductor to the metal contacts is quantified by the product $\kappa L = \Gamma L/2v$. In the strong-coupling limit

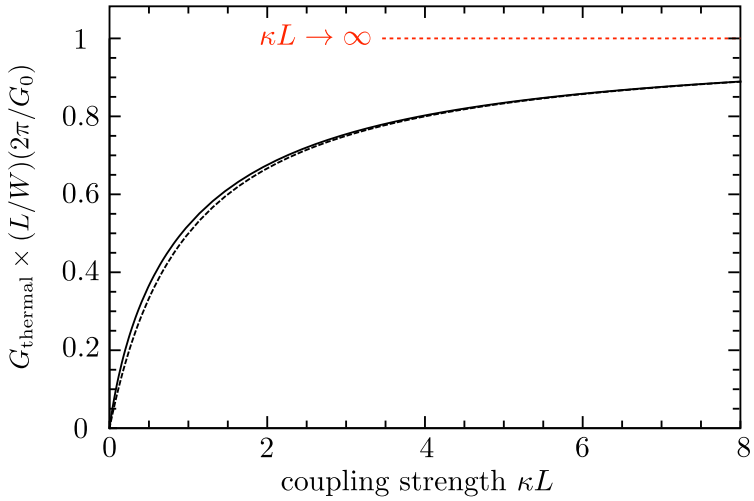

Figure 2.4. Thermal conductance of the surface of a 3D topological superconductor (aspect ratio $W/L \gg 1$) as a function of the coupling strength to the normal-metal contacts. The solid curve is calculated from Eq. (2.35), the dashed curve is the effective-length approximation (2.37). In the strong-coupling limit $G_{\rm thermal} \to (W/L)(G_0/2\pi)$.

$\kappa L \to \infty$ the thermal conductivity approaches the universal value

$$\frac{L}{W} G_{\rm thermal} \to \frac{1}{2\pi} G_0, \quad \text{for} \quad \kappa L \to \infty, \tag{2.36}$$

This is the Majorana fermion analogue [67, 70] of the Dirac fermion conductivity in graphene [69, 71]. The effect of a finite coupling strength can be understood in terms of an effective length $L_{\rm eff} = L + 1/\kappa$, so that

$$G_{\rm thermal} \approx \frac{1}{2\pi} G_0 \times \frac{W}{L_{\rm eff}} = \frac{G_0 W}{2\pi L} \frac{\kappa L}{1 + \kappa L}, \tag{2.37}$$

see Fig. 2.4.

2.5.2 Coupled surfaces

If we allow for coupling of the top and bottom surfaces via the metal contact, we would use the Green's function (2.32) instead of Eq. (2.28), to arrive at

$$G_{\rm thermal} = G_0 \frac{W}{2\pi} \int_0^\infty dq \, \frac{2\kappa^2 \sinh^2 \xi d}{(\xi \cosh qL \cosh \xi d + q \sinh qL \sinh \xi d)^2}. \tag{2.38}$$

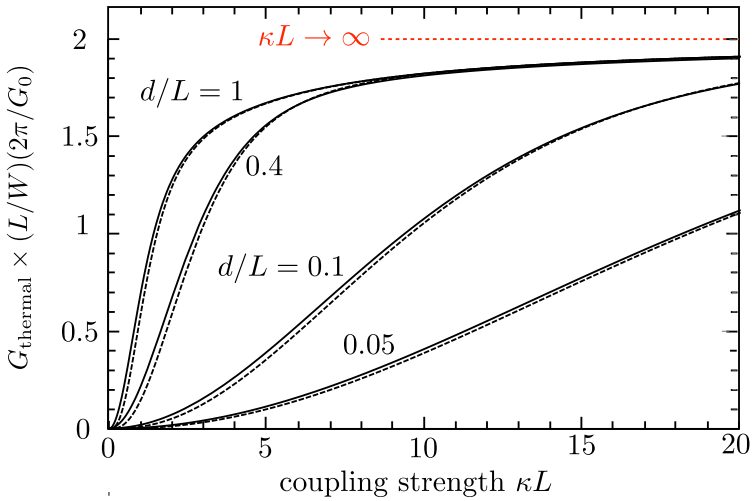

Figure 2.5. Thermal conductance for coupled top and bottom surfaces. For $d/L \gg 1$ we recover twice the single-surface plot in Fig. 2.4. The solid curves for finite d are calculated from Eq. (2.38), the dashed curves are the approximation (2.39).

There are now contributions from two surfaces in parallel, so $(L/W)G_{\rm thermal} \to 2 \times G_0/2\pi$ in the large-κ limit. As shown in Fig. 2.5, the finite-d effect is accurately described by a reduction factor $\tanh^2 \kappa d$,

$$G_{\rm thermal} \approx \frac{G_0 W}{2\pi L} \frac{2\kappa L \tanh^2 \kappa d}{1 + \kappa L}. \tag{2.39}$$

2.5.3 Finite aspect ratio

Deviations from the universal limit (2.36) of the thermal conductivity appear even for strong coupling to the metal contacts, if the aspect ratio of the surface area is not large enough. The relevant variable is the ratio $r = \mathcal{P}/L$ of the perimeter $\mathcal{P} = 2(W + d)$ of the metal contacts relative to their separation L.

Transverse momenta are quantized with antiperiodic boundary conditions, because of the π Berry phase,

$$q_n = (2n + 1)\pi/\mathcal{P}, \quad n = 0, \pm 1, \pm 2, \ldots. \tag{2.40}$$

For strong coupling to the contacts ($\kappa \gg 1/L, 1/d$) we find from Eq. (2.35)

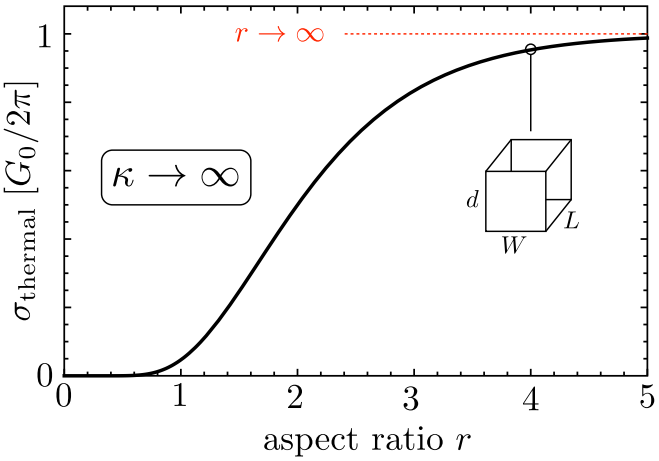

Figure 2.6. Thermal conductivity in the limit $\kappa \to \infty$ of strong coupling to the metal contacts, as a function of the aspect ratio $r = 2(W + d)/L$. The curve is calculated from Eq. (2.41). A cube has $r = 4$ and $\sigma_{\rm thermal} = 0.95 \times G_0/2\pi$.

the thermal conductivity $\sigma_{\rm thermal} = (L/\mathcal{P})G_{\rm thermal}$ as the sum

$$\sigma_{\rm thermal} = G_0 \sum_{n=-\infty}^{\infty} \frac{1}{2r\cosh^2[(2n+1)\pi/r]}. \tag{2.41}$$

As shown in Fig. 2.6, the universal limit is reached rather quickly; for a cube geometry, $L = W = d \Rightarrow r = 4$, we are only 5% below the universal limit.

2.5.4 Locality condition

In this model calculation the general locality condition (2.22) on the coupling matrix reads

$$w(z,q)\tau_z w^\dagger(z,q') = \delta_{qq'} R(z), \tag{2.42}$$

since $\delta_{qq'} \mapsto \delta(x - x')$ upon Fourier transformation. The 2×2 matrix R, acting on the spin degree of freedom, may depend on z but it should not depend on q. We only need to impose locality in x, because in Eq. (2.24) we have already taken a local coupling in z.

The electron-hole and time-reversal symmetry constraints

$$w(z,q) = w^*(z,-q)\tau_x, \quad w(z,q) = \sigma_y w^*(z,-q)\sigma_y \tag{2.43}$$

require that

$$R(z) = -R^{\mathrm{T}}(z) = -\sigma_y R(z)\sigma_y, \tag{2.44}$$

and this is only possible for a 2×2 matrix[4] if $R(z)\equiv 0$. Then Eq. (2.29) gives $t^\dagger(z,z')\tau_z t(z,z')\equiv 0$ and thus Eq. (2.13) implies the equality

$$P_{\mathrm{shot}}/P_0 = G_{\mathrm{thermal}}/G_0. \tag{2.45}$$

All the results presented above for the thermal conductance then apply also to the shot noise power.

Within the 2D model calculation of this section we cannot ascertain that the locality condition (2.42) holds. For that purpose we need to perform a fully 3D calculation, as we will do in the next section.

2.6 Numerical solution of the full 3D scattering problem

2.6.1 Model Hamiltonian

Our numerical simulation is based on the Bogoliubov-De Gennes Hamiltonian [10]

$$\begin{aligned} H(\mathbf{k}) = &\left(\frac{\mathbf{k}^2}{2m} + V(\boldsymbol{r}) - E_{\mathrm{F}}\right)\sigma_0\otimes\tau_z \\ &+ \Delta\left(k_z\sigma_z\otimes\tau_x - k_y\sigma_0\otimes\tau_y - k_x\sigma_x\otimes\tau_x\right), \end{aligned} \tag{2.46}$$

discretized on a cubic lattice (lattice constant a_0, hopping energy t_0). The disorder potential is V and the p-wave pair potential is Δ. This is a generic model of a 3D topological superconductor in symmetry class DIII, without spin-rotation symmetry but with electron-hole and time-reversal symmetries

$$H(\boldsymbol{k}) = -\tau_x H^*(-\boldsymbol{k})\tau_x, \quad H(\boldsymbol{k}) = \sigma_y H^*(-\boldsymbol{k})\sigma_y. \tag{2.47}$$

The geometry is that of Fig. 2.1, in the normal-metal regions we set $\Delta\equiv 0$. A tunnel barrier of height U_{barrier} (two lattice sites wide) is introduced at the NS interfaces $z=\pm L/2$. The scattering matrix is calculated using the Kwant toolbox [72] . We fixed the Fermi energy at $E_{\mathrm{F}} = 2.5\,t_0$ and took a relatively large pair potential $\Delta = 0.4\,E_{\mathrm{F}}$ to eliminate bulk conduction without requiring a large L.

[4] Any 2×2 antisymmetric matrix R is a scalar multiple of σ_y, so if we insist that R anticommutes with σ_y we must have $R\equiv 0$.

2.6.2 Translationally invariant system

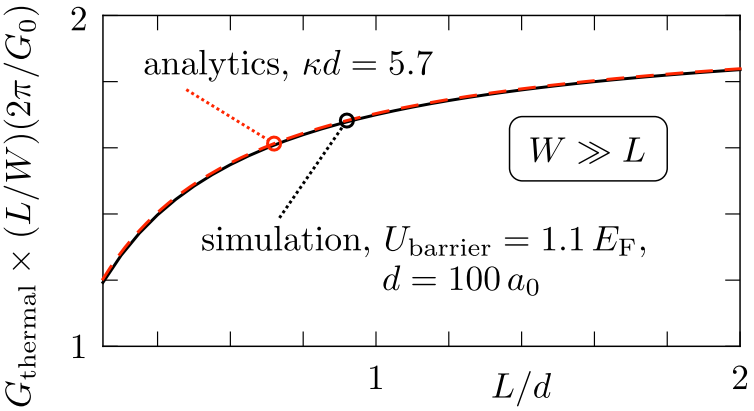

Figure 2.7. Comparison of the analytical result (2.38) for the thermal conductance with a numerical simulation of the Hamiltonian (2.46). The coupling strength κ at the NS interface is the single fit parameter for the comparison. These are calculations in the simplest case $V_0 = 0$, $B_0 = 0$, $\alpha_{\text{so}} = 0$, $W/L \to \infty$.

For a direct test of the analytical calculation from the previous section we first consider a translationally invariant system along the x-direction ($W \gg L, d \simeq 100a_0$, no disorder). Results are shown in Fig. 2.7. The analytical result Eq. (2.38) describes the numerics very well, with the coupling strength κ as the single fit parameter. This demonstrates the validity of the 2D representation of the 3D scattering problem, including the effect of coupling between top and bottom surfaces.

We next investigate the extent to which the relation (2.45) holds, still in the translationally invariant system, by adding to the Hamiltonian (2.46) the spin-orbit coupling

$$V_{\text{so}} = \alpha_{\text{so}} k_x \sigma_y \otimes \tau_z, \tag{2.48}$$

in order to mix the modes from top and bottom surface. (The same V_{so} is added to superconducting and normal regions.) Note that V_{so} preserves the electron-hole and time-reversal symmetries (2.47). We break time-reversal symmetry by imposing on the normal metal the magnetic field $\boldsymbol{B} = B_0\theta(|z| - L/2)\hat{x}$, in the gauge $\boldsymbol{A} = B_0\theta(|z| - L/2)\, y\hat{z}$.

As shown in Fig. 2.8, both a nonzero α_{so} and a nonzero B_0 are needed for a difference between dimensionless shot noise power and thermal conductance. The nonzero α_{so} is needed to couple the modes from top and

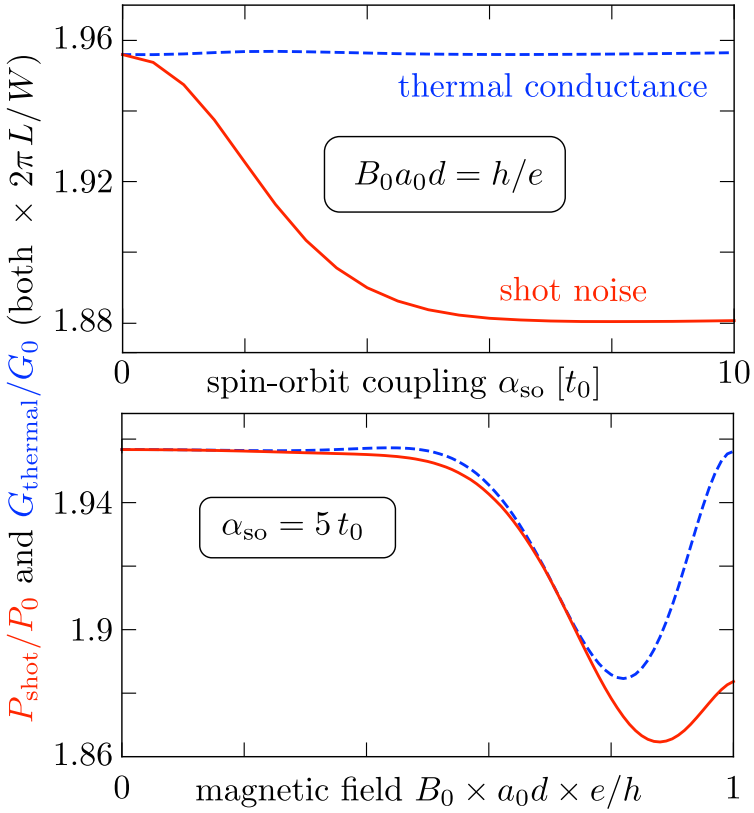

Figure 2.8. Numerical results for the shot noise power (red solid curves) and thermal conductance (blue dashed curves), in a superconductor with $L = d = 100\, a_0$, $W/L \to \infty$, $V_0 = 0$, $U_{\rm barrier} = 0$. The magnetic field and spin-orbit coupling are varied in, respectively, the bottom and top panel. This simulation demonstrates the inequality $P_{\rm shot}/P_0 \leq G_{\rm thermal}/G_0$, with equality if either B_0 or $\alpha_{\rm so}$ vanishes.

bottom surface — otherwise the transmission matrix would be of rank one and the equality (2.45) would hold irrespective of whether time-reversal symmetry is broken or not [38]. The nonzero B_0 is needed because of the argument from Sec. 2.3.2 that mode coupling in the presence of time-reversal symmetry is not effective at violating the relation between shot noise power and thermal conductance.

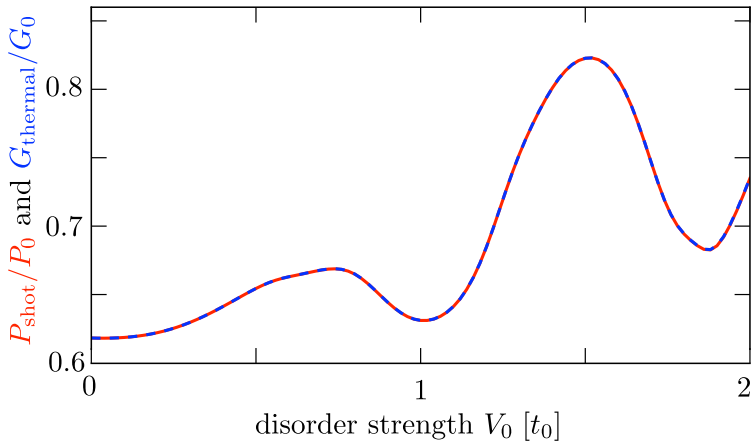

Figure 2.9. Numerical results for the shot noise power (red solid curve) and thermal conductance (blue dashed curve) as a function of the disorder potential strength V_0, in a superconductor with $L = d = W = 20\,a_0$ ($B_0 = 0$, $\alpha_{\rm so} = 0$, $U_{\rm barrier} = 0$). Shot noise and thermal conductance differ by less than 10^{-3}, even in the presence of significant disorder.

2.6.3 Disorder effects

We now break translational invariance by adding a disorder potential V, uniformly distributed in the interval $(-V_0, +V_0)$, randomly fluctuating from site to site throughout the superconductor. We also added disorder on the normal side of the NS interface (in a sheet of width $10a_0$). Because the calculations are now computationally more expensive we took a smaller superconductor, a cube of size $L = W = d = 20a_0$. Results are shown in Fig. 2.9.

Without disorder the thermal conductivity is close to the limit expected from Fig. 2.5 for a cube aspect ratio: $\sigma_{\rm thermal}/G_0 = 0.95/2\pi \Rightarrow G_{\rm thermal}/G_0 = 0.605$. Disorder has a significant effect, but the dimensionless shot noise and thermal conductance remain nearly indistinguishable.

2.7 Discussion

As a particle that is its own antiparticle, a Majorana fermion must be charge-neutral — but it need not be in an eigenstate of charge. This is a key distinction between a Majorana fermion as a fundamental particle such as a neutrino, or as a composite quasiparticle in a superconductor.

For the latter only the expectation value of the charge must vanish, so there may be quantum fluctuations of the charge. Here we have shown how we can exploit this property for a purely electrical detection of the Majorana surface states in a 3D topological superconductor, obviating the difficulty of thermal measurements.

We like to think of the relation

$$G_{\text{thermal}}/P_{\text{shot}} = \mathcal{L}T/eV, \quad \mathcal{L} \equiv \tfrac{1}{3}(\pi k_{\text{B}}/e)^2, \tag{2.49}$$

between thermal conductance and electrical shot noise power as the Majorana counterpart of the electronic Wiedemann-Franz relation

$$G_{\text{thermal}}/G_{\text{electrical}} = \mathcal{L}T \tag{2.50}$$

between thermal and electrical conductance [60]. The analogy is quite direct: Eq. (2.50) expresses the fact that a nonequilibrium electron transports energy and charge in a fixed ratio. The same holds for Eq. (2.49), with the electron charge $Q = e$ replaced by the Majorana charge variance $\operatorname{Var} Q = e^2$.

There exists an altogether different "Wiedemann-Franz type relation" for Majorana fermions, relating heat and *particle* currents rather than heat and *charge* currents:

$$G_{\text{thermal}}/G_{\text{particle}} = \tfrac{1}{2}G_0, \quad G_0 = \tfrac{1}{3}(\pi k_{\text{B}})^2\, T. \tag{2.51}$$

The "particle conductance" G_{particle} is not directly measurable (since Majorana fermions do not couple to the chemical potential), but it can be formally defined in terms of the Landauer formula $G_{\text{particle}} = N\mathcal{T}/h$ or in terms of an equivalent Kubo formula [60]. The factor $1/2$ is the "topological" or "central" charge $\mathcal{C} = 1/2$ of a Majorana fermion [4]. No such factor appears in Eq. (2.49), because both the thermal conductance and the shot noise power are proportional to $\mathcal{C}$, so it drops out of the ratio.

One direction for future research is to generalize the relation (2.49) to topological superconductors with more than a single species of Majorana fermions on their surface. This is a key difference with 3D topological insulators, which have a $\mathbb{Z}_2$ topological quantum number, so at most a single Dirac cone on the surface. In contrast, 3D topological superconductors have a $\mathbb{Z}$ topological quantum number, allowing for multiple Majorana cones [10, 16, 73].

Another direction to explore is how the class-DIII topological superconductors with Majorana surface states considered here compare with

the class-CI topological superconductors with Dirac surface states. For Eq. (2.51) the difference is simply a factor of two, to account for a central charge $\mathcal{C} = 1$ of Dirac fermions [70]. We do not expect such a simple correspondence for the relation (2.49).

From the experimental point of view, the usefulness of Eq. (2.49) is that it provides a purely electrical way to access the transport properties of Majorana surface states. The shot noise measurements should be performed at energies eV well below the superconducting gap Δ. In $Cu_xBi_2Se_3$ this is about 0.6 meV [34]. Shot noise dominates over thermal noise if $eV \gtrsim 3k_BT$ [63], so if one would perform the experiment at $V = 0.1\,\mathrm{meV}$, a readily accessible temperature range $T \lesssim 0.3\,\mathrm{K}$ would do.

2.8 Appendix: Matrix Green's function of the surface Hamiltonian

We solve the differential equation

$$\left[-i\sigma_x\frac{\partial}{\partial z} + q\sigma_z - \tfrac{1}{2}i\Gamma(z)\sigma_0 - E\right]\mathcal{G}(z,z';q,E) = \mathbb{1}\delta(z-z') \tag{2.52}$$

to obtain the 2×2 matrix Green's function that determines the transmission matrix of the Majorana fermions between the normal-metal contacts. (To simplify the notation we have set $v \equiv 1$.) For a similar calculation in graphene, see Ref. [74].

We first consider in Sec. 2.8.1 the case of uncoupled top and bottom surfaces, when the z-coordinate ranges over the entire real axis and the tunnel coupling in the contact region is given by

$$\Gamma(z) = \Gamma\theta(|z| - L/2), \quad -\infty < z < \infty. \tag{2.53}$$

In Sec. 2.8.2 we incorporate the finite extension d of the contact region, by setting

$$\Gamma(z) = \Gamma\left[\theta(|z| - L/2) - \theta(|z| - L/2 - d)\right], \quad |z| < L + d. \tag{2.54}$$

Antiperiodic boundary conditions at $z = \pm(L + d)$ then couple the top and bottom surfaces.

2.8.1 Single surface

We define

$$\varepsilon(z) = E + \tfrac{1}{2}i\Gamma(z), \;\; \varepsilon_0 = E + \tfrac{1}{2}i\Gamma, \tag{2.55}$$

with $\Gamma(z)$ given by Eq. (2.53). The Green's function that decays at infinity is

$$\begin{aligned}\mathcal{G}(z,z';q,E) = \mathcal{P}_{z\leftrightarrow 0}\exp\left[\int_0^z dz_1\,(i\sigma_z\varepsilon(z_1)+q\sigma_y)\right][M-\tfrac{i}{2}\sigma_z+i\sigma_z\theta(z-z')] \\ \cdot\,\mathcal{P}_{0\leftrightarrow z'}\exp\left[\int_0^{z'} dz_2\,(-i\sigma_z\varepsilon(z_2)+q\sigma_y)\right],\end{aligned} \tag{2.56}$$

where $\mathcal{P}_{z_1\leftrightarrow z_2}$ indicates a monotically increasing or decreasing ordering of the z-dependent non-commuting operators, from z_1 leftmost to z_2 rightmost. The matrix M is determined by the requirement that $\lim_{z\to\pm\infty}\mathcal{G}(z,z';q,E) = 0$:

$$\left(-\varepsilon_0 \pm i\sqrt{q^2-\varepsilon_0^2}, q\right)\cdot\exp[\pm\tfrac{1}{2}L(iE\sigma_z+q\sigma_y)](M\pm\tfrac{1}{2}i\sigma_z) = 0. \tag{2.57}$$

The row-spinor on the left-hand-side is orthogonal (without taking complex conjugates) to the column-spinor

$$|\pm\rangle = \begin{pmatrix}\varepsilon_0 \mp i\sqrt{q^2-\varepsilon_0^2}\\ q\end{pmatrix}, \tag{2.58}$$

which is an eigenstate of

$$(i\varepsilon_0\sigma_z + q\sigma_y)|\pm\rangle = \pm\sqrt{q^2-\varepsilon_0^2}|\pm\rangle. \tag{2.59}$$

The square root should be taken such that $\mathrm{Re}\,\sqrt{q^2-\varepsilon^2} > 0$.

The result is

$$\begin{aligned} M &= \begin{pmatrix}M_1 & M_2\\ M_2 & M_1\end{pmatrix},\\ M_1 &= \frac{E(\xi_0^2-\frac{1}{2}i\Gamma E)\cosh(L\xi_0)+E\xi\xi_0\sinh(L\xi_0)+\frac{1}{2}i\Gamma q^2}{2\xi\xi_0^2\cosh(L\xi_0)+2(\xi_0^2-\frac{1}{2}i\Gamma E)\xi_0\sinh(L\xi_0)},\\ M_2 &= \frac{q(\xi_0^2-\frac{1}{2}i\Gamma E)\cosh(L\xi_0)+q\xi\xi_0\sinh(L\xi_0)+\frac{1}{2}i\Gamma qE}{2\xi\xi_0^2\cosh(L\xi_0)+2(\xi_0^2-\frac{1}{2}i\Gamma E)\xi_0\sinh(L\xi_0)}, \end{aligned} \tag{2.60}$$

with the definitions

$$\xi_0 = \sqrt{q^2 - E^2}, \;\; \xi = \sqrt{q^2 - (E + \tfrac{1}{2}i\Gamma)^2}. \tag{2.61}$$

As a check, we take the limit $E \to 0$, $q \to 0$, when $M \to \frac{1}{2}i\sigma_0$, as it should. Note the symmetry relations

$$\sigma_y M^{\mathrm{T}}(-q, E)\sigma_y = M(q, E), \;\; M^*(-q, -E) = -M(q, E), \tag{2.62}$$

which ensure that the Green's function (2.56) satisfies the required time-reversal and electron-hole symmetries:

$$\sigma_y \mathcal{G}^{\mathrm{T}}(z', z; -q, E)\sigma_y = \mathcal{G}(z, z'; q, E), \tag{2.63}$$

$$\mathcal{G}^*(z, z'; -q, -E) = -\mathcal{G}(z, z'; q, E). \tag{2.64}$$

To obtain the transmission matrix we set $z > L/2$ and $z' < -L/2$:

$$\begin{aligned}\mathcal{G}(z, z'; q, E) = \; & \exp\Big[(z - L/2)\Big(iE\sigma_z - \tfrac{1}{2}\Gamma\sigma_z + q\sigma_y\Big)\Big] \\ & \cdot \exp\left[(L/2)(iE\sigma_z + q\sigma_y)\right] \\ & \cdot \Big(M + \tfrac{1}{2}i\sigma_z\Big) \exp[(L/2)(iE\sigma_z - q\sigma_y)] \\ & \cdot \exp\Big[-(z' + L/2)\Big(iE\sigma_z - \tfrac{1}{2}\Gamma\sigma_z - q\sigma_y\Big)\Big]. \end{aligned} \tag{2.65}$$

For $E = 0$ this simplifies to Eq. (2.28) in the main text.

2.8.2 Coupled top and bottom surfaces

The Green's function for coupled top and bottom surfaces is still of the form (2.56), with $\Gamma(z)$ now given by Eq. (2.54). Instead of a decay at infinity we now have the antiperiodic boundary conditions

$$\mathcal{G}\left(L + d, z'; q, E\right) = -\mathcal{G}\left(-L - d, z'; q, E\right). \tag{2.66}$$

The condition (2.57) on the matrix M is replaced by

$$\begin{aligned} & \exp\Big[\tfrac{1}{2}L\left(iE\sigma_z + q\sigma_y\right)\Big] \exp\left[d\left(i\varepsilon_0\sigma_z + q\sigma_y\right)\right] \\ & \cdot \exp\Big[\tfrac{1}{2}L\left(iE\sigma_z + q\sigma_y\right)\Big] \Big(M + \tfrac{1}{2}i\sigma_z\Big) = \\ & \quad = -\exp\Big[-\tfrac{1}{2}L\left(iE\sigma_z + q\sigma_y\right)\Big] \exp\left[-d\left(i\varepsilon_0\sigma_z + q\sigma_y\right)\right] \\ & \qquad \cdot \exp\Big[-\tfrac{1}{2}L\left(iE\sigma_z + q\sigma_y\right)\Big] \Big(M - \tfrac{1}{2}i\sigma_z\Big), \end{aligned} \tag{2.67}$$

with solution

$$M = \begin{pmatrix} M_1 & M_2 \\ M_2 & M_1 \end{pmatrix}, \tag{2.68}$$

$$M_1 = \frac{E(\xi_0^2 - \frac{1}{2}i\Gamma E)\cosh(L\xi_0)\tanh(\xi d) + E\xi\xi_0\sinh(L\xi_0) + \frac{1}{2}i\Gamma q^2\tanh(\xi d)}{2\xi\xi_0^2\cosh(L\xi_0) + 2(\xi_0^2 - \frac{1}{2}i\Gamma E)\xi_0\sinh(L\xi_0)\tanh(\xi d)},$$

$$M_2 = \frac{q(\xi_0^2 - \frac{1}{2}i\Gamma E)\cosh(L\xi_0)\tanh(\xi d) + q\xi\xi_0\sinh(L\xi_0) + \frac{1}{2}i\Gamma qE\tanh(\xi d)}{2\xi\xi_0^2\cosh(L\xi_0) + 2(\xi_0^2 - \frac{1}{2}i\Gamma E)\xi_0\sinh(L\xi_0)\tanh(\xi d)}.$$

For the transmission matrix we set $-L/2 - d < z' < -L/2$ and $L/2 < z < L/2 + d$. The energy-dependent Green's function is then given by Eq. (2.65) with M from Eq. (2.68). At zero energy this produces the result (2.32) from the main text.

Chapter 3

Topologically protected charge transfer along the edge of a chiral p-wave superconductor

3.1 Introduction

The second moment of the transferred charge in a Majorana mode is directly determined by the quantized thermal conductance. Higher moments are not so constrained, and one might ask whether they are quantized as well. Here we calculate the full probability distribution $P(q)$ of the transferred charge, including also the effects of finite temperature. In the zero-temperature limit we find that the characteristic (moment generating) function $F(\chi) = \langle e^{i\chi q}\rangle$, related to $P(q)$ by a Fourier transform, has the form

$$F(\chi) = \left[1 + \tfrac{1}{4}(e^{ie\chi} - 1) + \tfrac{1}{4}(e^{-ie\chi} - 1)\right]^{\mathcal{N}}. \tag{3.1}$$

This describes a trinomial counting statistics where $\mathcal{N} = eV\tau/h$ attempts transfer either $-e$, 0, or $+e$ charge, with probabilities 1/4, 1/2, and 1/4,

The contents of this chapter have been published and reprinted with permission from N. V. Gnezdilov, B. van Heck, M. Diez, J. A. Hutasoit, and C. W. J. Beenakker, Phys. Rev. B **92**, 121406(R) (2015).

respectively.

This result for the statistics of charge transported by a chiral Majorana edge mode can be contrasted with the characteristic function for the charge transmitted by an electronic mode in a nanowire [75],

$$F_{\text{electron}}(\chi) = \left[1 + \mathcal{T}(e^{ie\chi} - 1)\right]^{\mathcal{N}}, \tag{3.2}$$

where $\mathcal{T} \in [0, 1]$ is the transmission probability. The two key distinctions with Eq. (3.1) are that the counting statistics is binomial, rather than trinomial, and that the transfer probability is not quantized. A chiral quantum Hall edge mode would have a quantized $\mathcal{T} = 1$, but then there would be no charge fluctuations at all.

To see that these distinctions are not merely a consequence of the presence of a superconductor, we compare with the corresponding result for the charge transferred through a normal-metal-superconducting (NS) point contact [76],

$$F_{\text{NS}}(\chi) = \left[1 + \mathcal{R}_{\text{A}}(e^{2ie\chi} - 1)\right]^{\mathcal{N}}. \tag{3.3}$$

The transmission probability is replaced by the probability $\mathcal{R}_{\text{A}}$ for Andreev reflection [77] and the unit of transferred charge is doubled, but the statistics remains binomial and not quantized.

Resonant tunneling through a Majorana zero-mode, bound to a vortex or to the end of a nanowire, provides another point of comparison [78–80]. For two contacts biased at voltage $\pm V/2$ and coupled to the zero-mode with tunnel probabilities $\mathcal{T}_1$, $\mathcal{T}_2$, the charge entering contact 1 has characteristic function [80]

$$F_{\text{zero-mode}} = \left[1 + \mathcal{T}_1(\mathcal{T}_1 + \mathcal{T}_2)^{-1}(e^{ie\chi} - 1)\right]^{\mathcal{N}}. \tag{3.4}$$

The statistics is binomial and dependent on the tunnel probabilities, except for a symmetric junction (when $\mathcal{T}_1 = \mathcal{T}_2$ it drops out).[1]

[1] For a symmetric coupling to the Majorana zero-mode ($\mathcal{T}_1 = \mathcal{T}_2$), the trinomial and binomial characteristic functions (3.1) and (3.4) are related by $\ln F_{\text{zero-mode}}(\chi) = \frac{1}{2} ie\mathcal{N}\chi + \frac{1}{2} \ln F(\chi)$, so cumulants of order two and higher differ only by a factor of two. This explains the correspondence between the Bernoulli numbers in Eq. (3.18) and the Euler polynomial of Ref. [80]. For general $\mathcal{T}_n$ there is no such correspondence between trinomial and binomial distributions.

3.2 Full counting statistics of Majorana edge states

Our analysis follows the scattering theory of counting statistics pioneered by Levitov and Lesovik [75], in the convenient formulation of Klich [81]. The characteristic function is given by

$$F(\chi) = \operatorname{Tr}\rho_0 \exp\left[ie\chi \sum_{E>0} c^\dagger(E)\mathcal{P}c(E)\right] \times \exp\left[-ie\chi \sum_{E>0} c^\dagger(E)\mathcal{M}(E)c(E)\right], \tag{3.5}$$

$$\mathcal{M}(E) = S^\dagger(E)\mathcal{P}S(E), \quad S = \begin{pmatrix} r' & t' \\ t & r \end{pmatrix}, \quad \mathcal{P} = \begin{pmatrix} 0 & 0 \\ 0 & \sigma_z \end{pmatrix}. \tag{3.6}$$

The sum over energies is understood as $\sum_E \to (\tau/h)\int dE$ in the limit $\tau \to \infty$. The trace gives the expectation value with density matrix ρ_0 of the fermion operators $c, c^\dagger$, representing the quasiparticles injected into the edge from the two contacts, contact 1 at voltage V and contact 2 grounded. The scattering matrix S relates incoming and outgoing quasiparticles, with reflection and transmission subblocks. The matrix $\mathcal{P}$ selects the quasiparticles at contact 2, where the current is measured. The Pauli matrix σ_z appearing in $\mathcal{P}$ acts on the electron-hole degree of freedom, to account for the fact that electron and hole quasiparticles contribute with opposite sign to the electrical current.

Because different energies are uncoupled, we may perform the trace at each energy separately, so that we may write Eq. (3.5) in the form

$$\ln F(\chi) = \sum_{E>0} \ln \operatorname{Tr}\Big(e^{-\beta c^\dagger(E)\mathcal{E}(E)c(E)} \times e^{ie\chi c^\dagger(E)\mathcal{P}c(E)} e^{-ie\chi c^\dagger(E)\mathcal{M}(E)c(E)} \Big) - \ln Z, \tag{3.7}$$

$$\mathcal{E}(E) = E - eV \begin{pmatrix} \sigma_z & 0 \\ 0 & 0 \end{pmatrix}. \tag{3.8}$$

Here $\beta = 1/k_{\mathrm{B}}T$ and $Z = \operatorname{Tr} e^{-\beta c^\dagger \mathcal{E} c}$ is the partition function at temperature T (the same for both contacts) and chemical potential μ (equal to $\pm eV$ for electrons and holes at contact 1, and equal to 0 at contact 2).

With the help of the formula [81, 82]

$$\operatorname{Tr}\textstyle\prod_n e^{c^\dagger A_n c} = \operatorname{Det}\left(1 + \prod_n e^{A_n}\right), \tag{3.9}$$

the expression (3.7) reduces to

$$\ln F(\chi) = \frac{\tau}{h}\int_0^\infty dE\, \ln \mathrm{Det}(1-\mathcal{F}+\mathcal{F}e^{ie\chi\mathcal{P}}e^{-ie\chi\mathcal{M}}), \tag{3.10}$$

$$\mathcal{F}(E) = [1+e^{\beta\mathcal{E}(E)}]^{-1}. \tag{3.11}$$

The matrix exponentials simplify because $\mathcal{P}^{2n}=\mathcal{P}^2$, $\mathcal{P}^{2n+1}=\mathcal{P}$, $\mathcal{M}^{2n}=\mathcal{M}^2$, $\mathcal{M}^{2n+1}=\mathcal{M}$ (in view of unitarity, $SS^\dagger=1$), hence

$$\begin{aligned} e^{ie\chi\mathcal{P}} &= 1+\mathcal{P}^2(\cos e\chi-1)+i\mathcal{P}\sin e\chi,\\ e^{-ie\chi\mathcal{M}} &= 1+\mathcal{M}^2(\cos e\chi-1)-i\mathcal{M}\sin e\chi. \end{aligned} \tag{3.12}$$

In the zero-temperature limit $\mathcal{F}(E)\mathcal{P}\to 0$ for $E>0$, so the factor $e^{ie\chi\mathcal{P}}$ in Eq. (3.10) may be replaced by unity. To first order in V we then have

$$\begin{aligned} \ln F_0(\chi) = (eV\tau/h)\ln\mathrm{Det}\big[1+\\ +\tfrac{1}{2}(1+\sigma_z)t^\dagger(\cos e\chi-1-i\sigma_z\sin e\chi)t\big], \end{aligned} \tag{3.13}$$

with transmission matrix t evaluated at the Fermi energy $E=0$.

These formulas hold for any channel connecting two metal contacts via a superconductor. We now use that the connection is via an unpaired Majorana edge mode, which implies that the $2N\times 2N$ transmission matrix has rank one, irrespective of the number $2N$ of electron-hole modes in the metal contact: $t=\mathcal{T}^{1/2}uv^{\mathrm{T}}$ with unit vectors u,v and transmission probability $\mathcal{T}$. Particle-hole symmetry at the Fermi level requires that $t=\sigma_x t^*\sigma_x$, hence the matrix $t^\dagger\sigma_z t$ vanishes identically:

$$t^\dagger\sigma_z t = -i\sigma_x t^{\mathrm{T}}\sigma_y t = -i\mathcal{T}(u^{\mathrm{T}}\sigma_y u)\sigma_x vv^{\mathrm{T}}=0. \tag{3.14}$$

Similarly, $t\sigma_z t^\dagger=0$ while $tt^\dagger$ has a single nonzero eigenvalue equal to $\mathcal{T}$. We thus arrive at

$$\ln F_0(\chi) = \mathcal{N}\ln\big[1+\tfrac{1}{2}\mathcal{T}(\cos e\chi-1)\big],\ \ \mathcal{N}=eV\tau/h, \tag{3.15}$$

which for $\mathcal{T}=1$ is the result (3.1) announced in the introduction.

The corresponding trinomial probability distribution $P(q)$ of the transferred charge $q=0,\pm1,\pm2,\ldots\pm\mathcal{N}$ (in units of the electron charge e) is given by

$$\begin{aligned} P(q) = \frac{(2-\mathcal{T})^{\mathcal{N}-|q|}\mathcal{T}^{|q|}\mathcal{N}!}{2^{\mathcal{N}+|q|}(\mathcal{N}-|q|)!|q|!}\\ \times {}_2F_1\left[\tfrac{|q|-\mathcal{N}}{2},\tfrac{|q|+1-\mathcal{N}}{2},|q|+1,\tfrac{\mathcal{T}^2}{(2-\mathcal{T})^2}\right], \end{aligned} \tag{3.16}$$

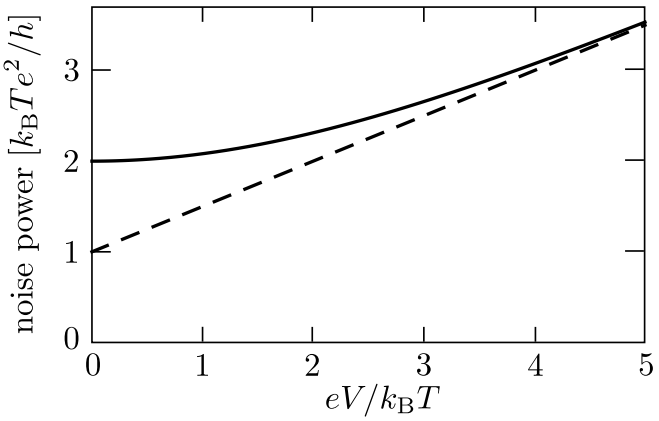

Figure 3.1. Noise power P of the Majorana edge mode at temperature T, as a function of bias voltage V. The solid curve is calculated from Eq. (3.22), the dashed line is the low-temperature asymptote (3.23). These are results for a single-channel contact ($N = 1$) to a fully transmitted edge mode ($\mathcal{T} = 1$). Here the voltage is assumed to be small on the scale of the superconducting gap Δ_0. See Fig. 3.2 for the voltage dependence in the regime $k_B T \ll eV \lesssim \Delta_0$.

with ${}_2F_1$ the hypergeometric function. For $\mathcal{T} = 1$ this simplifies to

$$P(q) = 2^{-2\mathcal{N}} \binom{2\mathcal{N}}{\mathcal{N} - q}, \tag{3.17}$$

which looks like a *displaced* binomial distribution. Cumulants are coefficients in the Taylor series $\ln F(\chi) = \sum_p \langle\langle q^p \rangle\rangle (i\chi)^p / p!$, giving for $\mathcal{T} = 1$ the result

$$\langle\langle q^p \rangle\rangle = \begin{cases} 2\mathcal{N}(2^{p+1} - 1) \frac{p!}{(p+1)!} B_{p+1} & \text{for } p \text{ even}, \\ 0 & \text{for } p \text{ odd}, \end{cases} \tag{3.18}$$

with B_{p+1} the Bernoulli number. The first few values are

$$\mathcal{N}^{-1} \langle\langle q^p \rangle\rangle = \tfrac{1}{2}, -\tfrac{1}{4}, \tfrac{1}{2}, -\tfrac{17}{8}, \tfrac{31}{2} \quad \text{for} \quad p = 2, 4, 6, 8, 10. \tag{3.19}$$

All of this is at zero-temperature.

3.2.1 Finite temperature

The general finite-temperature formulas are complicated, for a compact expression we take the case $N = 1$, $\mathcal{T} = 1$ of a single-channel contact

to a fully transmitted edge mode. The determinant in Eq. (3.10) then evaluates to

$$\ln F(\chi) = \frac{\tau}{h}\int_0^\infty dE\, \ln\big[1 + \tfrac{1}{2}f(1-f)(\cos 2e\chi - 1) + (f + \tfrac{1}{2}f_V - f f_V)(\cos e\chi - 1)\big], \tag{3.20}$$

$$f(E) = (1+e^{\beta E})^{-1}, \quad f_V = f(E-eV) + f(E+eV). \tag{3.21}$$

This is the multinomial statistics of transferred charge $0, \pm e, \pm 2e$, with the interpretation that charge $\pm e$ is transferred via the Majorana edge mode and charge $\pm 2e$ is transferred via Andreev reflection into the bulk superconductor. The corresponding noise power is

$$P = -\frac{1}{\tau}\lim_{\chi\to 0}\frac{d^2}{d\chi^2}\ln F(\chi) =$$

$$= \frac{e^2}{h}\int_0^\infty dE\,\big[\tfrac{1}{2}f_V(1-2f) + 3f - 2f^2\big] \tag{3.22}$$

$$= \frac{e^2}{h}\times\begin{cases}(k_{\rm B}T + \frac{1}{2}eV) & \text{for } k_{\rm B}T \lesssim eV,\\ 2k_{\rm B}T & \text{for } eV \ll k_{\rm B}T.\end{cases} \tag{3.23}$$

As a check, we note that the thermal noise power is related to the contact conductance [2] $G = e^2/h$ by

$$P_{\rm thermal} \equiv \lim_{V\to 0} P = 2k_{\rm B}TG, \tag{3.24}$$

in accordance with the Johnson-Nyquist relation.

From Fig. 3.1 we see that the slope dP/dV is within 10% of the quantized value $e^2/2h$ for voltages $eV \gtrsim 3k_{\rm B}T$. This lower limit on the voltage is to be combined with an upper limit set by the superconducting energy gap. From Fig. 3.2 we estimate that the quantization is preserved even in the presence of strong disorder when $eV \lesssim \Delta_0/2$. For a realistic gap [83, 84] of 0.2 meV the quantized shot-noise regime would then be accessible at temperatures below 0.4 K, which is a quite feasible requirement.

[2] The contact conductance G in the geometry of Fig. 1.4 is given in terms of the $2N\times 2N$ reflection matrix r at the contact by $G = \frac{1}{2}(e^2/h)\,\mathrm{Tr}\,(1 - r^\dagger\tau_z r\tau_z)$. For $N=1$, $\mathcal{T}=1$ we have $r = ab^{\rm T}$, $r^\dagger = \sigma_x b a^{\rm T}\sigma_x$, with unit vectors a, b, hence $G = e^2/h$.

[3] The Hamiltonian of the chiral p-wave superconductor on a two-dimensional square lattice is $H = \varepsilon(\boldsymbol{k})\sigma_z + \Delta_0(\sigma_x \sin k_x a + \sigma_y \sin k_y a)$, $\varepsilon(\boldsymbol{k}) = -2t_0(\cos k_x a + \cos k_y a) - \mu$.

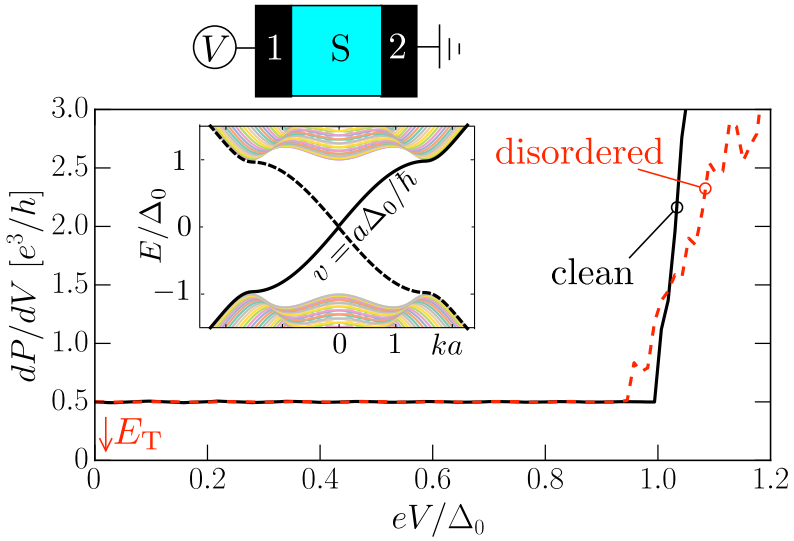

Figure 3.2. Voltage dependence of the zero-temperature shot noise power, calculated numerically[3] for the tight-binding Hamiltonian of a chiral p-wave superconductor (black solid and dashed curves in the band structure are the counterpropagating Majorana modes at opposite edges). The superconducting region ($W = L = 100$ in units of the lattice constant a) is connected to metallic leads (superconductor and lead 2 grounded, lead 1 at voltage V). The electron-to-electron and electron-to-hole transmission matrices $t_{ee}(E)$ and $t_{he}(E)$ from lead 1 to 2 are calculated as a function of the energy $E = eV$. The differential shot noise power in lead 2 then follows from [12, 62] $dP/dV = (e^3/h)\mathrm{Tr}\,(T_+ - T_-^2)$, with $T_\pm = t_{ee}^\dagger t_{ee} \pm t_{he}^\dagger t_{he}$. The black solid curve is the result for a clean system, the red dashed curve is obtained in the presence of a random on-site potential $U_n \in [-\Delta_0/2, \Delta_0/2]$. The red arrow indicates the Thouless energy $E_\mathrm{T} = \hbar v/L$. This simulation demonstrates that the quantized shot noise $dP/dV = e^3/2h$ is insensitive to disorder for voltages $|V| \lesssim \Delta_0/e$ — even if eV is large compared to E_T.

3.3 Discussion

We discuss three further issues regarding the robustness of the quantized shot noise of the Majorana edge mode.

[3] For the simulations in Fig. 3.2 we took parameters $t_0 = \Delta_0$, $\mu = -2\Delta_0 + U$, for which the velocity of the edge mode equals $v = a\Delta_0/\hbar$. (In the normal metal leads we set Δ_0 to zero, keeping the same t_0 and μ.) In the clean system $U \equiv 0$, in the disordered system U is varied randomly from site to site. The scattering matrix was calculated using the KWANT code from [72].

1) Impurity scattering along the edge has no effect because of the chirality of the edge mode, prohibiting backscattering. The contact resistance may in principle reduce $\mathcal{T}$ below unity, but this effect can be minimized by using an extended contact: If each of the two contacts contains $2N$ electron-hole modes with tunnel probability Γ to the edge mode, then $\mathcal{T} \simeq [\min(1, N\Gamma)]^2$. Hence contact resistances have no effect on the quantized shot noise if $N\Gamma \gtrsim 1$. We need to avoid a large thermal noise due to Andreev reflection from such an extended contact, which is of order $k_{\rm B}TN\Gamma^2$. Both conditions, maximal coupling ($\mathcal{T} = 1$) with minimal thermal noise ($P_{\rm thermal} \simeq k_{\rm B}Te^2/h$), are satisfied if we take $1/N \ll \Gamma \ll 1/\sqrt{N}$, so that $N\Gamma \gg 1$, $N\Gamma^2 \ll 1$.

2) Loss of phase coherence has no effect on the quantized shot noise. The coherent electron-hole superposition of a Majorana fermion is fragile indeed, coupling to the electromagnetic environment will project it onto an electron or a hole, effectively measuring the charge of the quasiparticle. The trinomial statistics, however, remains unaffected, because each of the $\mathcal{N}$ current pulses still transfers the same amount of charge $\pm e$ with equal probability 1/4.

3) The shot noise quantization is a macroscopic effect, preserved on scales large compared to the Thouless energy $E_{\rm T} = \hbar v/L$. This is the energy scale on which electrons and holes dephase after traveling with velocity v over a distance L and which governs transport experiments in an interferometer [85, 86]. As demonstrated in Fig. 3.2, raising the voltage to $eV \approx E_{\rm T}$ has a negligible effect on the shot noise. The reason for this unusual insensitivity is that the electron and hole component of the Majorana mode acquire *the same* phase factor at finite energy [87], so no dephasing can occur. The fact that the energy scale for the quantization is set by Δ_0 rather than by $E_{\rm T}$ is crucial for the observability of the effect.

In conclusion, we have identified unique electrical signatures of a charge-neutral Majorana mode propagating along the edge of a topological superconductor: A trinomial statistics of transferred charge, with quantized cumulants persisting in a macroscopic system, since they are insensitive to impurity scattering or loss of phase coherence. A promising physical system to search experimentally for the shot noise quantization could be an array of parallel nanowires [59, 88–91] or parallel chains of magnetic atoms [92, 93], all on a superconducting substrate.

As a direction for further theoretical research we point to the effect of interactions among the Majorana fermions. Two recent studies [94, 95]

have found an interaction-driven quantum phase transition from central charge $c = 1/2$ to $c = 3/2$. Because the coefficient $1/2$ in the shot noise power (1.2) originates from the central charge of the Majorana mode, it would be interesting to see what is the effect of this phase transition on the charge transfer statistics. A related extension of our results would be to topological superconductors with a higher Chern number, supporting multiple Majorana modes at each edge, for which physical realizations have been recently predicted [96, 97].

3.4 Appendix: Effect of a tunnel barrier at the NS contact

A tunnel barrier at the normal-metal–superconductor (NS) interface is needed to suppress the thermal noise from Andreev reflection. At zero temperature this is of no concern, but it turns out that a tunnel barrier is still advantageous because it reduces the voltage sensitivity of the shot noise power. We show this in Fig. 3.3, where we compare the zero-temperature dP/dV for the two cases.

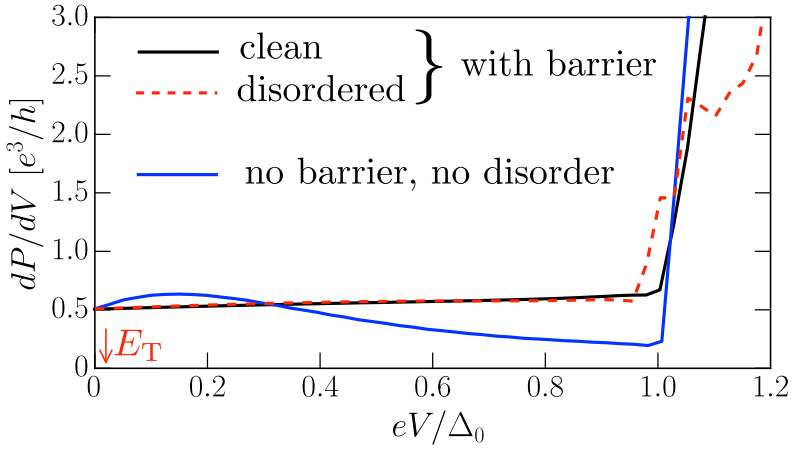

Figure 3.3. Voltage dependence of the zero-temperature shot noise power in the model of Fig. 3.2. The black curves are with a tunnel barrier at the NS interfaces (transmission probability $\Gamma = 0.32$ in each of $N = 100$ modes), the blue curve is without any barrier. For $V \lesssim E_T$ there is no difference, for larger V a tunnel barrier helps to preserve the quantization all the way up to the superconducting gap.

Chapter 4

Valley switch in a graphene superlattice due to pseudo-Andreev reflection

4.1 Introduction

The precession of a spin in a magnetic field has analogues for the pseudospin degrees of freedom that characterize quasiparticles in condensed matter. The K,K′ valley index of Dirac electrons in graphene is a such a pseudospin — it is actively studied because it might play a role as a carrier of information in "valleytronics", the valley-based counterpart of spintronics [98]. The analogue of the magnetic field for valley precession can be provided by a superlattice potential: [99–102] When graphene is deposited on a substrate with a commensurate honeycomb lattice, the valleys are coupled by the periodic modulation of the potential on the carbon atoms [103–105]. The coupling can be represented by an artificial magnetic field [106] that rotates the valley pseudospin as the electron propagates through the superlattice [99], analogously to the spin-rotation by an exchange field in spintronics [107].

The contents of this chapter have been published and reprinted with permission from C. W. J. Beenakker, N. V. Gnezdilov, E. Dresselhaus, V. P. Ostroukh, Y. Herasymenko, İ. Adagideli, and J. Tworzydło, Phys. Rev. B **97**, 241403(R) (2018).

Here we present a valley precession effect without a counterpart in spintronics: A quantized 180° precession angle upon reflection, such that the electron switches valleys. This valley switch is analogous to Andreev reflection at the interface between a normal metal and a topological superconductor [11]. Andreev reflection is the reflection as a hole of an electron incident on the superconductor, which happens with unit probability if the normal-superconductor interface contains a Majorana zero-mode. The analogous effect happens in the superlattice because of an anti-unitary symmetry that is formally equivalent to the charge-conjugation symmetry in a superconductor.

4.2 Graphene superlattice with anti-unitary symmetry

We consider the Dirac Hamiltonian [103–105]

$$H = \begin{pmatrix} V_0+\mu & v_{\rm F}p_- & 0 & \alpha \\ v_{\rm F}p_+ & V_0-\mu & -\beta^* & 0 \\ 0 & -\beta & V_0-\mu & v_{\rm F}p_- \\ \alpha^* & 0 & v_{\rm F}p_+ & V_0+\mu \end{pmatrix}. \tag{4.1}$$

It acts on the spinor $\Psi = (\psi_{\rm KA}, \psi_{\rm KB}, -\psi_{\rm K'B}, \psi_{\rm K'A})$ that contains the sublattice (A,B) and valley (K,K′) degrees of freedom of a conduction electron moving in the x–y plane of a carbon monolayer (graphene), with velocity $v_{\rm F}$ and momentum $\boldsymbol{p} = (p_x, p_y)$, $p_\pm \equiv p_x \pm i p_y$. In terms of Pauli matrices σ_i and τ_i acting, respectively, on the sublattice and valley indices, we may write

$$\begin{aligned} H = {} & v_{\rm F}(p_x\sigma_x + p_y\sigma_y) + \mu\tau_z\otimes\sigma_z \\ & + \tfrac{1}{2}(\tau_x\otimes\sigma_x){\rm Re}\,(\alpha-\beta) - \tfrac{1}{2}(\tau_y\otimes\sigma_y){\rm Re}\,(\alpha+\beta) \\ & - \tfrac{1}{2}(\tau_x\otimes\sigma_y){\rm Im}\,(\alpha-\beta) - \tfrac{1}{2}(\tau_y\otimes\sigma_x){\rm Im}\,(\alpha+\beta). \end{aligned} \tag{4.2}$$

For simplicity, we have shifted the zero of energy such that $V_0 = 0$.

An epitaxial substrate induces a periodic potential modulation, which triples the size of the unit cell: it is enlarged by a factor $\sqrt{3}\times\sqrt{3}$ and contains six rather than two carbon atoms. The parameters V_0, μ (real) and α, β (complex) are determined by the substrate potentials on these six

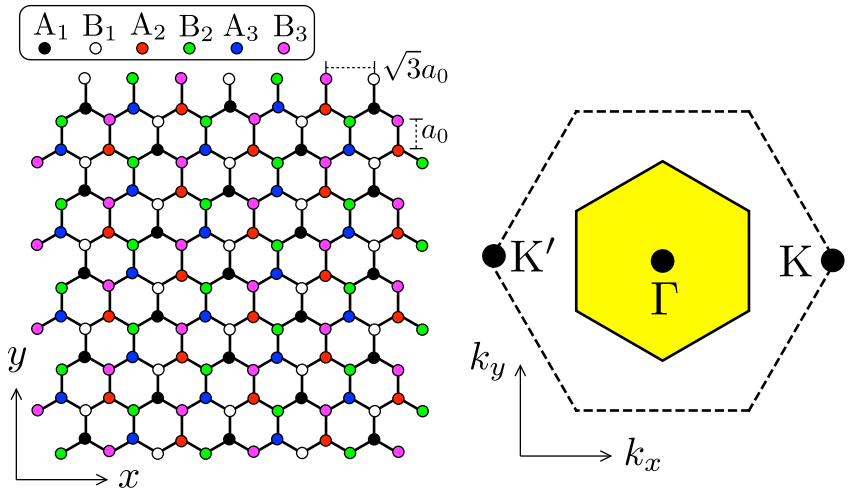

Figure 4.1. *Left panel*: Hexagonal lattice of graphene, decorated by a periodic potential modulation. Different colors distinguish the carbon atoms on the A and B sublattice, each of which has an ionic potential V_{A_n}, V_{B_n}, $n = 1, 2, 3$, induced by the substrate. The lattice constant a_0 of the original hexagonal lattice is increased by a factor $\sqrt{3}$ in the superlattice. *Right panel*: The Dirac points at the K and K′ points of the original Brillouin zone of graphene (dashed hexagon) are folded onto the Γ point at the center of the superlattice Brillouin zone (yellow hexagon).

atoms.[1] The Brillouin zone remains hexagonal, but the two Dirac cones at opposite corners K, K′ of the original Brillouin zone of graphene are folded onto the center Γ of the superlattice Brillouin zone. Depending on the relative magnitude of α, β, μ a gap may open or a linear or quadratic band crossing may appear [103–105].

If there is translational invariance in the y-direction,[2] the momentum component $p_y \equiv q$ is a good quantum number and we may consider the

[1] As derived in Ref. [105], the relationship between the parameters V_0, μ, α, β in the Dirac Hamiltonian (4.1) and the ionic potentials $V_{\mathrm{A}_n}, V_{\mathrm{B}_n}$, $n = 1, 2, 3$, in Fig. 4.1 is: $6V_0 = \sum_n (V_{\mathrm{A}_n} + V_{\mathrm{B}_n})$, $6\mu = \sum_n (V_{\mathrm{A}_n} - V_{\mathrm{B}_n})$, $6\alpha = 2V_{\mathrm{A}_1} - V_{\mathrm{A}_2} - V_{\mathrm{A}_3} + i\sqrt{3}(V_{\mathrm{A}_2} - V_{\mathrm{A}_3})$, $6\beta = 2V_{\mathrm{B}_1} - V_{\mathrm{B}_2} - V_{\mathrm{B}_3} + i\sqrt{3}(V_{\mathrm{B}_2} - V_{\mathrm{B}_3})$. When comparing with Ref. [105], note that we are using a basis in which the single-valley Dirac Hamiltonian $v_{\mathrm{F}}(\boldsymbol{p} \cdot \boldsymbol{\sigma})$ is the same in both valleys.

[2] For definiteness, we are considering the orientation of the graphene lattice shown in Fig. 4.1, with the x-direction parallel to the zigzag edge. A rotation of the lattice by an angle ϕ is equivalent to multiplication of α and β by $e^{i\phi}$.

Hamiltonian $H(q)$ at a fixed q. Time-reversal symmetry is expressed by

$$(\tau_y \otimes \sigma_y) H^*(q) (\tau_y \otimes \sigma_y) = H(-q), \tag{4.3}$$

where the complex conjugation should also be applied to the momentum operator $p_x = -i\hbar\partial/\partial x \equiv -i\hbar\partial_x$. Note the sign change of q. An additional anti-unitary symmetry without inversion of q exists if $\beta^* = \alpha$,

$$\begin{aligned} H(q) &= v_{\rm F}(-i\hbar\sigma_x\partial_x + q\sigma_y) + \mu\tau_z \otimes \sigma_z \\ &\quad - (\tau_y \otimes \sigma_y){\rm Re}\,\alpha - (\tau_x \otimes \sigma_y){\rm Im}\,\alpha, \ \text{ if } \ \beta^* = \alpha, \end{aligned} \tag{4.4}$$

$$\Rightarrow \tau_x H^*(q)\tau_x = -H(q). \tag{4.5}$$

4.3 Topological phase transitions

The symmetry (4.5) is formally identical to charge-conjugation symmetry in a superconductor, where τ_x switches electron and hole degrees of freedom. Because the symmetry operation $\mathcal{C} = \tau_x\mathcal{K}$ (with $\mathcal{K}$ = complex conjugation) squares to $+1$, it is symmetry class D in the Altland-Zirnbauer classification of topological states of matter [3] [108]. This correspondence opens up the possibility of a phase transition into a phase that is analogous to a topological superconductor [10, 16] — with the K and K′ valleys playing the role of electron and hole.

The q-dependent topological quantum number $\mathcal{Q}(q)$ of the Hamiltonian (4.4) follows from Kitaev's Pfaffian formula [6],

$$\mathcal{Q}(q) = {\rm sign}\,{\rm Pf}[\tau_x H(q)]_{p_x=0}. \tag{4.6}$$

(The multiplication by τ_x ensures that the Pfaffian Pf is calculated of an antisymmetric matrix.) We find

$$\mathcal{Q}(q) = {\rm sign}\,(v_{\rm F}^2 q^2 + \mu^2 - |\alpha|^2). \tag{4.7}$$

The graphene superlattice is always topologically trivial ($\mathcal{Q} = +1$) for large $|q|$. However, provided that $|\mu| < |\alpha|$, it is topologically nontrivial ($\mathcal{Q} = -1$) in an interval near $q = 0$. There is a pair of topological phase transitions at

$$q = \pm q_{\rm c}, \ \ v_{\rm F} q_{\rm c} = \sqrt{|\alpha|^2 - \mu^2}. \tag{4.8}$$

[3] For $\mu = 0$ the Hamiltonian (4.4) also has chiral symmetry (it anticommutes with σ_z), so then the symmetry class would be BDI rather than D. The difference is not essential for our analysis.

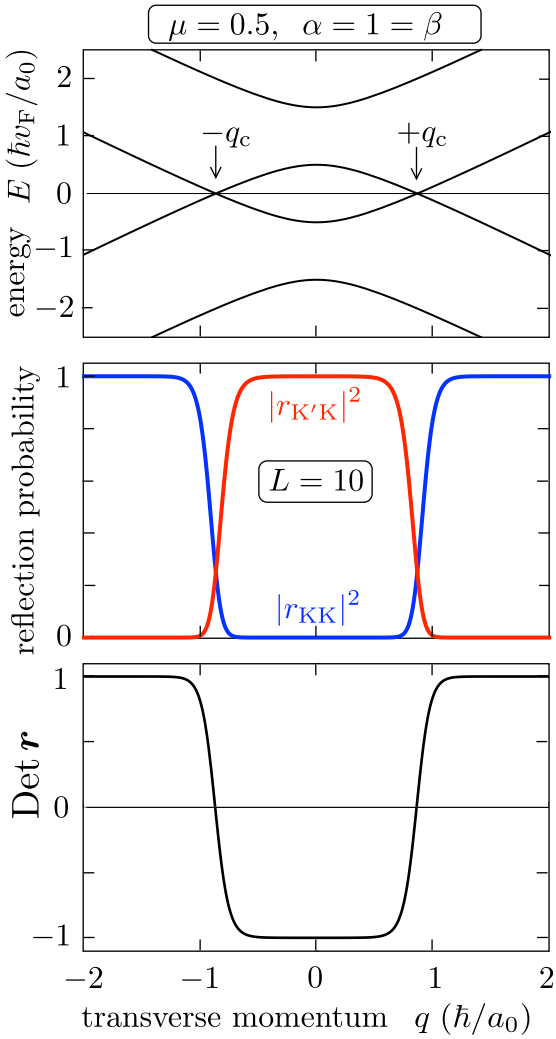

Figure 4.2. *Top panel*: Energy spectrum of superlattice graphene with Hamiltonian (4.4) at $\mu = 0.5$, $\alpha = 1 = \beta$ (in units of $\hbar v_\mathrm{F}/a_0$). *Middle panel*: Corresponding reflection probabilities from a superlattice-graphene strip of length $L = 10\,a_0$ in the x-direction, connected at $x = 0$ and $x = L$ to heavily doped pristine-graphene electrodes. In the topologically nontrivial regime near normal incidence ($|q| < q_\mathrm{c} = \sqrt{|\alpha|^2 - \mu^2}$) the reflection is completely into the opposite valley. *Bottom panel*: Topological order parameter $\mathcal{O}_L(q) = \mathrm{Det}\,\boldsymbol{r}$, computed from Eq. (4.10). The switch from intra-valley to inter-valley reflection lines up with the switch from $\mathcal{O}_L(q) = +1$ to -1.

To probe the topological phase transition, we contact the graphene superlattice at $x = 0$ and $x = L$ by pristine-graphene electrodes, heavily doped so that the Fermi energy in the pristine graphene is high above the Dirac point. By analogy with the conductance of a Kitaev wire [11], the 2×2 reflection matrix $\boldsymbol{r}$ in the large-L limit should be fully diagonal in the topologically trivial phase and fully off-diagonal in the topologically nontrivial phase. In the superconducting problem this means that there is complete Andreev reflection from the topological superconductor. Here the analogue is a complete *valley switch:* An incident electron in valley K is reflected in the other valley K′ with unit probability when $|q| < q_\mathrm{c}$.

4.4 Valley switch

Let us see how this expectation is borne out by an explicit calculation (detailed in the appendix). The energy spectrum of the Hamiltonian (4.4) is shown in Fig. 4.2. The intervalley coupling splits the Dirac cone at the Γ point into a pair of cones at $\boldsymbol{k} = (0, \pm q_\mathrm{c})$ which are gapped out if $|\mu| > |\alpha|$. The same figure shows the $E = 0$ reflection probabilities $|r_{\mathrm{K}'\mathrm{K}}|^2$ and $|r_{\mathrm{KK}}|^2$ with and without a valley switch. We clearly see the transition from complete inter-valley to complete intra-valley reflection at $q = \pm q_\mathrm{c}$.

The analytical formulas that govern this transition are simplest for the special case $\mu = 0$, when $q_\mathrm{c} = |\alpha|/v_\mathrm{F}$. We find the reflection matrix

$$\begin{aligned} &\boldsymbol{r} = \begin{pmatrix} r_{\mathrm{KK}} & r_{\mathrm{KK}'} \\ r_{\mathrm{K}'\mathrm{K}} & r_{\mathrm{K}'\mathrm{K}'} \end{pmatrix}, \quad r_{\mathrm{KK}} = r_{\mathrm{K}'\mathrm{K}'} = -Z^{-1} \sinh 2qL, \\ &r_{\mathrm{KK}'} = r^*_{\mathrm{K}'\mathrm{K}} = -iZ^{-1}(\alpha/|\alpha|) \sinh 2q_\mathrm{c}L, \\ &Z = \cosh 2q_\mathrm{c}L + \cosh 2qL. \end{aligned} \tag{4.9}$$

(We have set $\hbar \equiv 1$.) In the topologically trivial regime $|q| > q_\mathrm{c}$ the off-diagonal elements of $\boldsymbol{r}$ vanish $\propto \exp[-2(|q| - q_\mathrm{c})L]$, while in the topologically nontrivial regime $|q| < q_\mathrm{c}$ it is the diagonal elements that vanish $\propto \exp[-2(q_\mathrm{c} - |q|)L]$.

To confirm that the valley switch at $|q| = q_\mathrm{c}$ is due to a topological phase transition in a *finite* system, we calculate the L-dependent topological order parameter [38]

$$\begin{aligned} \mathcal{O}_L(q) &= \operatorname{Det} \boldsymbol{r} = -\tanh(\xi_- L) \tanh(\xi_+ L), \\ \xi_\pm &= |\alpha| \pm \sqrt{v_\mathrm{F}^2 q^2 + \mu^2}. \end{aligned} \tag{4.10}$$

Unlike the Pfaffian invariant (4.6), the determinant (4.10) crosses over smoothly from $+1$ to -1 in an interval around $|q| = q_c$. This interval becomes narrower and narrower with increasing L, approaching the discontinuous topological phase transition in the infinite-L limit. At $|q| = q_c$ the determinant of $\boldsymbol{r}$ vanishes, signifying the opening of a reflectionless mode, a mode that is transmitted with unit probability through the superlattice.

4.5 Robustness of the valley switch

The anti-unitary symmetry (4.5) is broken if we move away from the symmetry point $\beta^* = \alpha$. Let us find out how sensitive the valley switch effect is to the symmetry breaking. The simplest formulas appear for $\mu = 0$. To quantify the magnitude of the valley switch we calculate the ratio $\rho = |r_{\mathrm{KK}}/r_{\mathrm{K'K}}|^2$ at $q = 0$. We find

$$\rho = \frac{(|\alpha|^2 - |\beta|^2)^2}{4|\alpha^* \Xi + \beta \Xi^*|^2}, \quad \Xi = \sqrt{\alpha\beta}\coth(\sqrt{\alpha\beta}L), \tag{4.11}$$
$$\to \tfrac{1}{4}(|\alpha| - |\beta|)^2 \, |\alpha\beta|^{-1} \text{ for } L \to \infty \text{ if } \arg(\alpha\beta) \neq \pi,$$

see Fig. 4.3 for a plot. Only the absolute value of the complex amplitudes α, β enters in the large-L limit, provided that $\alpha\beta$ is not on the negative real axis (when reflection is quenched by the opening of a propagating mode). [4]

The valley switch happens with 100% probability if $|\alpha| = |\beta|$, but the ratio $|\alpha/\beta|$ may differ from unity by as much as a factor of two and still 90% of the reflected intensity at normal incidence happens with a valley switch. Fig. 4.4 shows that this robustness to variation of parameters persists for $\mu \neq 0$ – as long as $\mu < |\alpha| \approx |\beta|$.

Concerning the robustness of the valley switch to disorder, we firstly note that forward scattering events which only couple the transverse momenta within the topologically nontrivial interval $|q| < q_c$ do not spoil the topological protection. Secondly, large-angle scattering with a mean free path longer than the penetration depth $\xi = 1/q_c$ into the superlattice will also not affect the valley switch.

[4] In terms of the atomic potentials, the condition $\arg\alpha\beta = \pi$ is equivalent to $V_{\mathrm{A}_1}(V_{\mathrm{B}_3} - V_{\mathrm{B}_2}) + V_{\mathrm{A}_2}(V_{\mathrm{B}_2} - V_{\mathrm{B}_1}) + V_{\mathrm{A}_3}(V_{\mathrm{B}_1} - V_{\mathrm{B}_3}) = 0$, $V_{\mathrm{A}_1}(V_{\mathrm{B}_2} + V_{\mathrm{B}_3} - 2V_{\mathrm{B}_1}) + V_{\mathrm{A}_2}(V_{\mathrm{B}_1} + V_{\mathrm{B}_2} - 2V_{\mathrm{B}_3}) + V_{\mathrm{A}_3}(V_{\mathrm{B}_1} + V_{\mathrm{B}_3} - 2V_{\mathrm{B}_2}) > 0$.

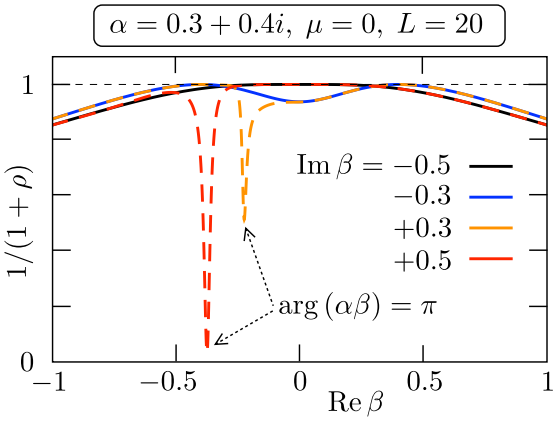

Figure 4.3. Plot of the fraction $1/(1+\rho) = |r_{\mathrm{K'K}}|^2/(|r_{\mathrm{KK}}|^2 + |r_{\mathrm{K'K}}|^2)$ of the reflected intensity at normal incidence ($q = 0$) that is reflected in the opposite valley, calculated from Eq. (4.11). The reflection with valley switch happens at close to unit probability provided that the product $\alpha\beta$ stays away from the negative real axis.

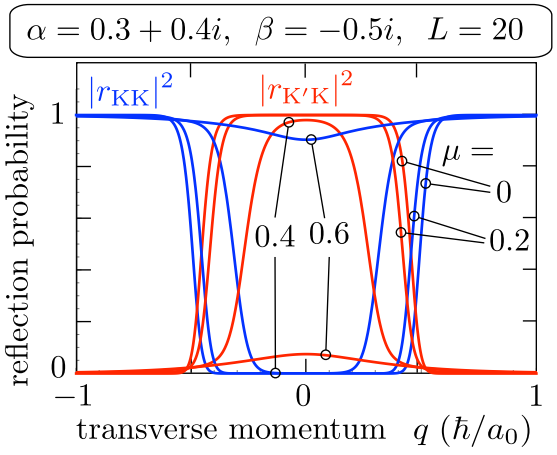

Figure 4.4. Reflection probabilities from the superlattice-graphene strip with and without a valley switch, for four values of μ. The parameters α, β are quite far from the ideal symmetry point $\beta^* = \alpha$, but still the reflection near normal incidence happens predominantly in the opposite valley ($|r_{\mathrm{K'K}}|^2 \approx 1$) provided $\mu < |\alpha| \approx |\beta|$.

4.6 Conclusion

We have presented a topological mechanism that switches the K, K' valley index of Dirac fermions in graphene. Unlike scattering processes that require control on the atomic scale, such as intervalley reflection from an armchair edge, our valley switch relies on the long-range effect of a superlattice potential.

The valley switch is protected by a topological invariant, the Pfaffian (4.6), originally introduced by Kitaev to describe a topologically nontrivial superconductor [6]. Because of this topological protection the switch happens with 100% probability even in the presence of a large Fermi energy mismatch at the interface with the superlattice. It is analogous to the 100% Andreev reflection from a Majorana zero-mode, which is also unaffected by a Fermi energy mismatch at the interface with the superconductor [11].

We have identified the symmetry point of the superlattice Hamiltonian at which an anti-unitary symmetry appears that is analogous to charge-conjugation symmetry in a superconductor, and we have checked that the valley switch remains close to 100% in a broad parameter range around that symmetry point. We expect that the analogy between intervalley reflection and Andreev reflection revealed in this work can provide further useful additions to the valleytronics toolbox [98].

4.7 Appendix: Scattering matrix of the graphene superlattice

The calculation of the scattering matrix of the graphene superlattice region $0 < x < L$, sandwiched between heavily doped pristine-graphene contacts, proceeds as follows. (See Refs. [69, 109] for similar calculations in graphene.)

We start from the Dirac Hamiltonian $H(p_x, p_y)$, given by Eq. (4.2). We consider solutions of the Dirac equation $H\Psi = E\Psi$ at energy E that are plane waves in the y-direction, $\Psi(x, y) = \Psi_q(x)e^{iqy}$. The four-component spinor $\Psi_q(x)$ in the region $0 < x < L$ is a solution of

$$\frac{\partial}{\partial x}\Psi_q(x) = \Xi(q)\Psi_q(x), \quad \Xi(q) = iv_{\mathrm{F}}^{-1}\sigma_x[E - H(0, q)], \tag{4.12}$$

resulting in the transfer matrix

$$\Psi_q(L) = \mathcal{T}(q)\Psi_q(0), \;\; \mathcal{T}(q) = e^{\Xi(q)}. \tag{4.13}$$

The next step is to transform to a basis of right-moving and left-moving modes in the contact regions $x < 0$, $x > L$. The Dirac Hamiltonian in those regions is

$$H_{\text{contact}} = v_{\text{F}}(p_x\sigma_x + p_y\sigma_y) - V_{\text{doping}}. \tag{4.14}$$

[We use the same valley-isotropic basis $\Psi = (\psi_{\text{KA}}, \psi_{\text{KB}}, -\psi_{\text{K}'\text{B}}, \psi_{\text{K}'\text{A}})$ as in Eq. (4.2).] In the limit $V_{\text{doping}} \to \infty$ of infinitely doped contacts the right-moving modes $\Psi_+(x,y)$ and left-moving modes $\Psi_-(x,y)$ are given for $x < 0$ by

$$\begin{aligned}
\Psi_+ &= c^+_{\text{K}} e^{ikx+iqy} \begin{pmatrix} 1 \\ 1 \\ 0 \\ 0 \end{pmatrix} + c^+_{\text{K}'} e^{ikx+iqy} \begin{pmatrix} 0 \\ 0 \\ 1 \\ 1 \end{pmatrix}, \\
\Psi_- &= c^-_{\text{K}} e^{-ikx+iqy} \begin{pmatrix} 1 \\ -1 \\ 0 \\ 0 \end{pmatrix} + c^-_{\text{K}'} e^{-ikx+iqy} \begin{pmatrix} 0 \\ 0 \\ 1 \\ -1 \end{pmatrix},
\end{aligned} \tag{4.15}$$

with $v_{\text{F}}k = V_{\text{doping}} \to \infty$. The same expression with $x \mapsto x - L$ applies for $x > L$.

The transfer matrix in the basis $(c^+_{\text{K}}, c^-_{\text{K}}, c^+_{\text{K}'}, c^-_{\text{K}'})$ is

$$\tilde{\mathcal{T}}(q) = \mathcal{H}\mathcal{T}(q)\mathcal{H}, \;\; \mathcal{H} = \frac{1}{\sqrt{2}} \begin{pmatrix} 1 & 1 & 0 & 0 \\ 1 & -1 & 0 & 0 \\ 0 & 0 & 1 & 1 \\ 0 & 0 & 1 & -1 \end{pmatrix}. \tag{4.16}$$

After this "Hadamard transform" [109] we can directly read off the elements of the reflection matrix $\boldsymbol{r}$ from the $x = 0$ interface,

$$\boldsymbol{r} = \begin{pmatrix} r_{\text{KK}} & r_{\text{KK}'} \\ r_{\text{K}'\text{K}} & r_{\text{K}'\text{K}'} \end{pmatrix} = -(\tilde{\mathcal{T}}_{--})^{-1} \cdot \tilde{\mathcal{T}}_{-+}, \tag{4.17a}$$

$$\tilde{\mathcal{T}}_{--} = \begin{pmatrix} \tilde{\mathcal{T}}_{22} & \tilde{\mathcal{T}}_{24} \\ \tilde{\mathcal{T}}_{42} & \tilde{\mathcal{T}}_{44} \end{pmatrix}, \;\; \tilde{\mathcal{T}}_{-+} = \begin{pmatrix} \tilde{\mathcal{T}}_{21} & \tilde{\mathcal{T}}_{23} \\ \tilde{\mathcal{T}}_{41} & \tilde{\mathcal{T}}_{43} \end{pmatrix}. \tag{4.17b}$$

The final results are lengthy and not recorded here, but they are easily derived using a computer algebra system.

Chapter 5

Low-high voltage duality in tunneling spectroscopy of the Sachdev-Ye-Kitaev model

5.1 Introduction

The Sachdev-Ye-Kitaev model, a fermionic version [27] of a disordered quantum Heisenberg magnet [28, 110], describes how N fermionic zero-energy modes are broadened into a band of width J by random infinite-range interactions. The phase diagram of the SYK Hamiltonian can be solved exactly in the large-N limit [29, 30, 47], when a conformal symmetry emerges at low energies that forms a holographic description of the horizon of an extremal black hole in a (1+1)-dimensional anti-de Sitter spac [27, 47, 110, 111].

To be able to probe this holographic behaviour in the laboratory, it is of interest to create a "black hole on a chip" [31, 32, 53], that is, to realize the SYK model in the solid state. Ref. [32] proposed to use a quan-

The contents of this chapter have been published and reprinted with permission from N. V. Gnezdilov, J. A. Hutasoit, and C. W. J. Beenakker, Phys. Rev. B **98**, 081413(R) (2018).

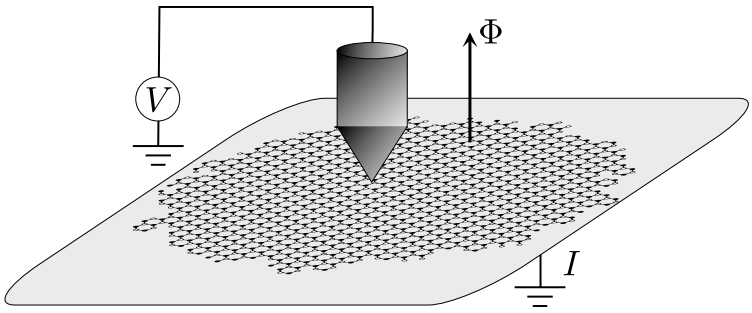

Figure 5.1. Tunneling spectroscopy of a graphene flake, in order to probe the complex-valued SYK model [53]. We calculate the current I driven by a voltage V through a single-channel point contact (coupling strength Γ) into a graphene flake on a grounded conducting substrate. At the charge neutrality point a chiral symmetry ensures that the zeroth Landau level (degeneracy $N = e\Phi/h$ for an enclosed flux Φ) is only broadened by electron-electron interactions (strength J). For a sufficiently random boundary the quantum dot can be described by the SYK Hamiltonian (5.1).

tum dot formed by an opening in a superconducting sheet on the surface of a topological insulator. In a perpendicular magnetic field the quantum dot can trap vortices, each of which contains a Majorana zero-mode [8]. Chiral symmetry ensures that the band only broadens as a result of four-Majorana-fermion terms in the Hamiltonian, a prerequisite for the real-valued SYK model. A similar construction uses an array of Majorana nanowires coupled to a quantum dot [31]. Since it might be easier to start from conventional electrons rather than Majorana fermions, Ref. [53] suggested to work with the complex-valued SYK model of interacting Dirac fermions in the zeroth Landau level of a graphene quantum dot. Chiral symmetry at the charge-neutrality point again suppresses broadening of the band by two-fermion terms.

The natural way to study a quantum dot is via transport properties. Electrical conduction through chains of SYK quantum dots has been studied in Refs. [50, 112–118]. For a single quantum dot coupled to a tunnel contact, as in Fig. 5.1, Refs. [31, 32, 53] studied the limit of negligibly small coupling strength Γ, in which the differential conductance $G = dI/dV$ equals the density of states of the quantum dot. Conformal symmetry in the large-N limit gives a low-voltage divergence $\propto 1/\sqrt{V}$, until eV drops below the single-particle level spacing $\delta \simeq J/N$ [119–121].

Here we investigate how a finite Γ affects the tunneling spectroscopy.

We focus on the complex-valued SYK model for Dirac fermions, as in the graphene quantum dot of Ref. [53]. Our key result is that in the large-N conformal symmetry regime $J/N \ll eV \ll J$ the zero-temperature differential conductance of the quantum dot depends on Γ, J, and V only via the dimensionless combination $\xi = eVJ/\Gamma^2$. Low and high voltages are related by the duality $G(\xi) = G(\pi/\xi)$, providing an experimental signature of the conformal symmetry.

5.2 Tunneling Hamiltonian

We describe the geometry of Fig. 5.1 by the Hamiltonian

$$\begin{aligned} H &= H_{\rm SYK} + \sum_p \varepsilon_p \psi_p^\dagger \psi_p + \sum_{i,p} (\lambda_i c_i^\dagger \psi_p + \lambda_i^* \psi_p^\dagger c_i), \\ H_{\rm SYK} &= (2N)^{-3/2} \textstyle\sum_{ijkl} J_{ij;kl}\, c_i^\dagger c_j^\dagger c_k c_l, \\ J_{ij;kl} &= J_{kl;ij}^* = -J_{ji;kl} = -J_{ij;lk}. \end{aligned} \tag{5.1}$$

The annihilation operators c_i, $i = 1, 2, \ldots$ represent the $N = h\Phi/e$ interacting Dirac fermions in the spin-polarized zeroth Landau level of the graphene quantum dot (enclosing a flux Φ). Two-fermion terms $c_i^\dagger c_j$ are suppressed by chiral symmetry when the Fermi level $\mu = 0$ is at the charge-neutrality point (Dirac point) [53]. The operators ψ_p represent electrons at momentum p in the single-channel lead (dispersion $\varepsilon_p = p^2/2m$, linearized near the Fermi level), coupled to mode i in the quantum dot with complex amplitude λ_i. The tunneling current depends only on the sum of $|\lambda_i|^2$, via the coupling strength

$$\Gamma = \pi \rho_{\rm lead} \textstyle\sum_i |\lambda_i|^2, \quad \rho_{\rm lead} = (2\pi\hbar v_{\rm F})^{-1}. \tag{5.2}$$

If $\mathcal{T} \in (0, 1)$ is the transmission probability into the quantum dot, one has $\Gamma \simeq \mathcal{T} N\delta \simeq \mathcal{T} J$.

The Hamiltonian $H_{\rm SYK}$ is the complex-valued SYK model [47] if we take random couplings $J_{ij;kl}$ that are independently distributed Gaussians with zero mean $\langle J_{ij;kl}\rangle = 0$ and variance $\langle |J_{ij;kl}|^2\rangle = J^2$. The zeroth Landau level then broadens into a band of width J, corresponding to a single-particle level spacing $\delta \simeq J/N$ (more precisely, $\delta \simeq J/N \ln N$) [119]. In the energy range $\delta \ll \varepsilon \ll J$ the retarded Green's functions can be evaluated in saddle-point approximation [47],

$$G^{\rm R}(\varepsilon) = -{\rm i}\pi^{1/4} \sqrt{\frac{\beta}{2\pi J}}\, \frac{\Gamma\left(1/4 - {\rm i}\beta\varepsilon/2\pi\right)}{\Gamma\left(3/4 - {\rm i}\beta\varepsilon/2\pi\right)}, \tag{5.3}$$

where $\beta = 1/k_{\mathrm{B}}T$ and $\Gamma(x)$ is the Gamma function. At zero temperature this simplifies to

$$G^{\mathrm{R}}(\varepsilon) = -\mathrm{i}\pi^{1/4} \exp\left[\tfrac{1}{4}\mathrm{i}\pi \operatorname{sgn}(\varepsilon)\right] |J\varepsilon|^{-1/2} . \tag{5.4}$$

Quantum fluctuations around the saddle point cut off the low-ε divergence for $|\varepsilon| < \delta$ [119–121].

5.3 Tunneling current

The graphene flake lies on a grounded substrate,[1] so the current is entirely determined by the transmission of electrons through the point contact. The current operator $\boldsymbol{I}$ is given by the commutator

$$\boldsymbol{I} = \frac{\mathrm{i}e}{\hbar}\left[H, \textstyle\sum_p \psi_p^\dagger \psi_p\right] = \mathrm{i}\frac{e}{\hbar}\sum_{n,p}\left(\lambda_n c_n^\dagger \psi_p - \lambda_n^* \psi_p^\dagger c_n\right). \tag{5.5}$$

We calculate the time-averaged expectation value of $\boldsymbol{I}$ using the Keldysh path integral technique [123–125], which has previously been applied to the SYK model in Refs. [112, 113, 117, 126]. The expectation value I of the tunneling current is given by the first derivative of cumulant generating function: [124]

$$I = -\mathrm{i}\lim_{\chi\to 0}\frac{\partial}{\partial\chi}\ln Z(\chi)\,, \tag{5.6}$$

$$Z(\chi) = \langle \mathcal{T}_C \exp(-\mathrm{i}\textstyle\int_C \mathrm{d}t \left[H + \frac{1}{2}\chi(t)\boldsymbol{I}\right])\rangle. \tag{5.7}$$

Here $\mathcal{T}_C$ indicates time-ordering along the Keldysh contour [123] of the counting field $\chi(t)$, equal to $+\chi$ on the forward branch of the contour (from $t = 0$ to $t = \infty$) and equal to $-\chi$ on the backward branch (from $t = \infty$ to $t = 0$). The calculation is worked out in the Appendix.

The result for the differential conductance is

$$G = \frac{dI}{dV} = \frac{e^2}{h}\int_{-\infty}^{+\infty} \mathrm{d}\varepsilon\, f'(\varepsilon - eV)\frac{4\Gamma \operatorname{Im} G^{\mathrm{R}}(\varepsilon)}{|1 + \mathrm{i}\Gamma G^{\mathrm{R}}(\varepsilon)|^2}\,, \tag{5.8}$$

[1] We assume that the grounded substrate does not spoil the non-Fermi-liquid state of the quantum dot. This might happen if the coupling becomes too strong, according to S. Banerjee and E. Altman, [122].

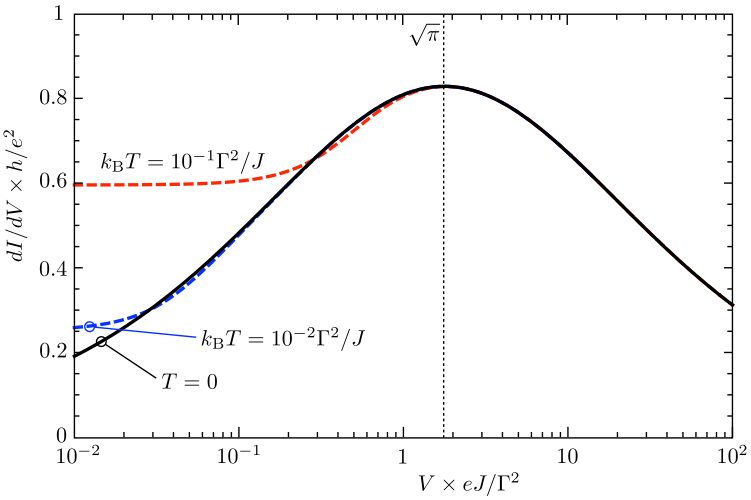

Figure 5.2. Differential conductance $G = dI/dV$ calculated from Eq. (5.8), as a function of dimensionless voltage $\xi = eVJ/\Gamma^2$ for three different temperatures. On the semi-logarithmic scale the duality between low and high voltages shows up as a reflection symmetry along the dotted line (where $\xi = \sqrt{\pi}$).

where $f(\varepsilon) = (1+e^{\beta\varepsilon})^{-1}$ is the Fermi function. Substitution of the conformal Green's function (5.3) gives upon integration the finite temperature curves plotted in Fig. 5.2.

At zero temperature $f'(\varepsilon - eV) \to -\delta(\varepsilon - eV)$ and substitution of Eq. (5.4) produces a single-parameter function of $\xi = eVJ/\Gamma^2$,

$$G(\xi) = \frac{e^2}{h} \frac{2\sqrt{2}}{\sqrt{2} + \pi^{1/4}\xi^{-1/2} + \pi^{-1/4}\xi^{1/2}}. \tag{5.9}$$

5.4 Low–high voltage duality

The $T = 0$ differential conductance (5.9) in the conformal regime $J/N \ll eV \ll J$ satisfies the duality relation

$$G(\xi) = G(\pi/\xi), \quad \text{if} \quad N^{-1}(J/\Gamma)^2 \ll \xi, 1/\xi \ll (J/\Gamma)^2. \tag{5.10}$$

The V-to-$1/V$ duality is visible in the semi-logarithmic Fig. 5.2 by a reflection symmetry of the differential conductance along the $\xi = \sqrt{\pi}$ axis. The symmetry is precise at $T = 0$, and is broken in the tails with increasing temperature.

The voltage range in which V and $1/V$ are related by Eq. (5.10) covers the full conformal regime for $N \simeq (J/\Gamma)^4$. In this voltage range the $1/\sqrt{V}$ tail at high voltages crosses over to a $\sqrt{V}$ decay at low voltages. The high-voltage tail reproduces the $1/\sqrt{V}$ differential conductance that follows [31, 32, 53] from the density of states in the limit $\Gamma \to 0$ (since $\xi \to \infty$ for $\Gamma \to 0$). The density of states gives [119–121] a crossover to a $\sqrt{V}$ decay when eV drops below the single-particle level spacing $\delta \simeq J/N$. Our finite-Γ result (5.9) implies that this crossover already sets in at larger voltages $eV \simeq \Gamma^2/J$, well above δ for $N \gg (J/\Gamma)^2$.

The symmetrically peaked profile of Fig. 5.2 is a signature of conformal symmetry in as much as this produces a power-law singularity in the retarded propagator at low energies. It is not specific for the square-root singularity (5.4), other exponents would give a qualitatively similar low-high voltage duality. For example, the generalized SYK_{2p} model with $2p \geq 4$ interacting Majorana fermion terms has a $\varepsilon^{(1-p)/p}$ singularity [29, 112], corresponding to the duality $G(\xi_p) = G(C_p/\xi_p)$ with C_p a numerical coefficient and $\xi_p = (eV)^{2(p-1)/p} J^{2/p} \Gamma^{-2}$. In contrast, a disordered Fermi liquid such as the non-interacting SYK_2 model, with Hamiltonian $H = \sum_{ij} J_{ij} c_i^\dagger c_j$, has a constant propagator at low energies and hence a constant dI/dV in the range $J/N \ll eV \ll J$.

5.5 Conclusion

We have shown that tunneling spectroscopy can reveal a low–high voltage duality in the conformal regime of the Sachdev-Ye-Kitaev model of N interacting Dirac fermions. A physical system in which one might search for this duality is the graphene quantum dot in the lowest Landau level, proposed by Chen, Ilan, De Juan, Pikulin, and Franz [53].

As argued by those authors, one should be able to reach N of order 10^2 for laboratory magnetic field strengths in a sub-micrometer-size quantum dot. This leaves two decades in the conformal regime $J/N \ll eV \ll J$. If we tune the tunnel coupling strength near the ballistic limit $\Gamma \lesssim J$, it should be possible even for these moderately large values of N to achieve $N \simeq (J/\Gamma)^4$ and access the duality over two decades of voltage variation. For such large Γ the condition on temperature, $k_\mathrm{B}T \ll \Gamma^2/J$ would then also be within experimental reach ($J \simeq 34\,\mathrm{meV}$ from Ref. [53] and $\Gamma \simeq 10\,\mathrm{meV}$ has $k_\mathrm{B}T = 10^{-2}\,\Gamma^2/J$ at $T = 300\,\mathrm{mK}$).

5.6 Appendix: Outline of the calculation

We describe the calculation leading to Eq. (5.8) for the current-voltage characteristics, generalizing it to nonzero chemical potential μ and including also the shot noise power. We set $\hbar$ and e to unity, except for the final formulas.

5.6.1 Generating function of counting statistics

Arbitrary cumulants of the current operator (5.5) can be obtained from the generating function (5.7). A gauge transformation allows us to write equivalently

$$Z(\chi) = \langle \mathcal{T}_C \exp(-\mathrm{i}\textstyle\int_C H(t)\,\mathrm{d}t)\rangle, \tag{5.11}$$

$$H(t) = H_{\rm SYK} + \textstyle\sum_p \varepsilon_p \psi_p^\dagger \psi_p - \mu \sum_n c_n^\dagger c_n + \sum_{n,p} \left(\mathrm{e}^{\mathrm{i}\chi(t)/2} \lambda_n c_n^\dagger \psi_p + \mathrm{e}^{-\mathrm{i}\chi(t)/2} \lambda_n^* \psi_p^\dagger c_n \right). \tag{5.12}$$

For generality we have added a chemical potential term $\propto \mu$. (In the main text we take $\mu = 0$, corresponding to a quantum dot at charge neutrality.)

We need the advanced and retarded Green's functions $G^{\rm A}(\varepsilon) = \big(G^{\rm R}(\varepsilon)\big)^*$ and the Keldysh Green's function

$$G^{\rm K}(\varepsilon) = \mathcal{F}(\varepsilon) \left(G^{\rm R}(\varepsilon) - G^{\rm A}(\varepsilon) \right), \quad \mathcal{F}(\varepsilon) = \tanh(\beta\varepsilon/2). \tag{5.13}$$

These are collected in the matrix Green's function $\mathcal{G}$, which on the Keldysh contour has the representation [125, 127]

$$\mathcal{G} = \begin{pmatrix} G^{\rm R} & G^{\rm K} \\ 0 & G^{\rm A} \end{pmatrix} = L\sigma_3 \begin{pmatrix} G^{++} & G^{+-} \\ G^{-+} & G^{--} \end{pmatrix} L^\dagger, \tag{5.14}$$

$$L = \frac{1}{\sqrt{2}} \begin{pmatrix} 1 & -1 \\ 1 & 1 \end{pmatrix}, \quad \sigma_3 = \begin{pmatrix} 1 & 0 \\ 0 & -1 \end{pmatrix}, \tag{5.15}$$

in terms of the Green's functions on the forward and backward branches

of the contour:

$$G^{++}(t,t') = -\mathrm{i}N^{-1}\sum_n \left\langle \mathcal{T}\, c_n(t)c_n^\dagger(t')\right\rangle, \tag{5.16a}$$

$$G^{+-}(t,t') = \mathrm{i}N^{-1}\sum_n \left\langle c_n^\dagger(t')c_n(t)\right\rangle, \tag{5.16b}$$

$$G^{-+}(t,t') = -\mathrm{i}N^{-1}\sum_n \left\langle c_n(t)c_n^\dagger(t')\right\rangle, \tag{5.16c}$$

$$G^{--}(t,t') = -\mathrm{i}N^{-1}\sum_n \left\langle \mathcal{T}^{-1}\, c_n(t)c_n^\dagger(t')\right\rangle. \tag{5.16d}$$

The operators $\mathcal{T}$ and $\mathcal{T}^{-1}$ order the times in increasing and decreasing order, respectively.

5.6.2 Saddle point solution

In the regime $J/N \ll \varepsilon \ll J$ the Green's function of the SYK model is given by the saddle point solution [47]

$$G^{\mathrm{R}}(\varepsilon) = -\mathrm{i}C\mathrm{e}^{-\mathrm{i}\theta}\sqrt{\frac{\beta}{2\pi J}}\,\frac{\Gamma\left(\frac{1}{4}-\mathrm{i}\frac{\beta\varepsilon}{2\pi}+\mathrm{i}\mathcal{E}\right)}{\Gamma\left(\frac{3}{4}-\mathrm{i}\frac{\beta\varepsilon}{2\pi}+\mathrm{i}\mathcal{E}\right)}, \tag{5.17}$$

with the definitions

$$\mathrm{e}^{2\pi\mathcal{E}} = \frac{\sin\left(\frac{\pi}{4}+\theta\right)}{\sin\left(\frac{\pi}{4}-\theta\right)},\quad C = (\pi/\cos 2\theta)^{1/4}. \tag{5.18}$$

The angle $\theta \in (-\pi/4, \pi/4)$ is a spectral asymmetry angle [128], determined by the charge per site $\mathcal{Q} \in (-1/2, 1/2)$ on the quantum dot according to [56]

$$\mathcal{Q} = N^{-1}\textstyle\sum_i \langle c_i^\dagger c_i\rangle - \frac{1}{2} = -\theta/\pi - \frac{1}{4}\sin 2\theta. \tag{5.19}$$

For $\mu = 0$, when $\mathcal{Q} = 0$, one has $\theta = 0$, $C = \pi^{1/4}$. In good approximation (accurate within 15%),

$$\theta \approx -\tfrac{1}{2}\pi\mathcal{Q} \Rightarrow C \approx (\pi/\cos\pi\mathcal{Q})^{1/4}. \tag{5.20}$$

In the mean-field approach the quartic SYK interaction (5.1) is replaced by a quadratic one with the kernel $\mathcal{G}^{-1}$ from Eq. (5.14). A Gaussian

integration over the Grassmann fields gives the generating function

$$\ln Z = \int_{-\infty}^{\infty} \frac{\mathrm{d}\varepsilon}{2\pi} \ln \left(\frac{\det \left[1 - \Gamma \Xi(\varepsilon) \Lambda^{\dagger} \mathcal{G}(\varepsilon) \Lambda \right]}{\det \left[1 - \Gamma \Xi(\varepsilon) \mathcal{G}(\varepsilon) \right]} \right), \tag{5.21}$$

$$\Lambda = \begin{pmatrix} \cos(\chi/2) & \mathrm{i}\sin(\chi/2) \\ \mathrm{i}\sin(\chi/2) & \cos(\chi/2) \end{pmatrix}, \quad \Xi(\varepsilon) = -\mathrm{i} \begin{pmatrix} 1 & 2\mathcal{F}(\varepsilon - V) \\ 0 & -1 \end{pmatrix}. \tag{5.22}$$

The matrix $\Xi(\varepsilon)$ is the Keldysh Green's function of the lead, integrated over the momenta. This evaluates further to

$$\ln Z = \int_{-\infty}^{\infty} \frac{d\varepsilon}{2\pi} \ln \Bigg[1 + \frac{\mathrm{i}\Gamma \left(G^{\mathrm{R}} - G^{\mathrm{A}} \right)}{\left(1 + \mathrm{i}\Gamma G^{\mathrm{R}} \right) \left(1 - \mathrm{i}\Gamma G^{\mathrm{A}} \right)} \cdot \Big(\left[1 - \mathcal{F}(\varepsilon) \mathcal{F}(\varepsilon - V) \right] (\cos\chi - 1) + \mathrm{i} \left[\mathcal{F}(\varepsilon) - \mathcal{F}(\varepsilon - V) \right] \sin\chi \Big) \Bigg]. \tag{5.23}$$

At zero temperature the distribution function simplifies to $\mathcal{F}(\varepsilon) \mapsto \operatorname{sgn}(\varepsilon)$, hence

$$\ln Z = \int_{0}^{V} \frac{d\varepsilon}{2\pi} \ln \left[1 + \frac{2\mathrm{i}\Gamma \left(G^{\mathrm{R}} - G^{\mathrm{A}} \right) \left(\mathrm{e}^{\mathrm{i}\chi} - 1 \right)}{\left(1 + \mathrm{i}\Gamma G^{\mathrm{R}} \right) \left(1 - \mathrm{i}\Gamma G^{\mathrm{A}} \right)} \right]. \tag{5.24}$$

5.6.3 Average current and shot noise power

A p-fold differentation of $Z(\chi)$ with respect to χ gives the p-th cumulant of the current. In this way the full counting statistics of the charge transmitted through the quantum dot can be calculated [124]. The first cumulant, the time-averaged current I from Eq. (5.6), is given by

$$I = \frac{e}{h} \int_{-\infty}^{+\infty} d\varepsilon \, \frac{\mathrm{i}\Gamma \left[\mathcal{F}(\varepsilon) - \mathcal{F}(\varepsilon - V) \right] \left(G^{\mathrm{R}} - G^{\mathrm{A}} \right)}{\left(1 + \mathrm{i}\Gamma G^{\mathrm{R}} \right) \left(1 - \mathrm{i}\Gamma G^{\mathrm{A}} \right)}, \tag{5.25}$$

which is Eq. (5.8) from the main text.

At zero temperature the differential conductance $G = dI/dV$ is

$$G(\xi) = \frac{2e^2}{h} \left[1 + \frac{1}{2\sin(\pi/4 + \theta)} \left(\frac{\sqrt{\xi}}{C} + \frac{C}{\sqrt{\xi}} \right) \right]^{-1}, \tag{5.26}$$

with $\xi = eVJ/\Gamma^2$. The duality relation

$$G(\xi) = G(C^4/\xi) \tag{5.27}$$

reduces to the one from the main text, $G(\xi) = G(\pi/\xi)$, when we set $\mu = 0 \Rightarrow \theta = 0 \Rightarrow C = \pi^{1/4}$.

The second cumulant, the shot noise power P, follows similarly from

$$P = -\lim_{\chi\to 0} \frac{\partial^2}{\partial\chi^2} \ln Z(\chi). \tag{5.28}$$

The Fano factor F, being the ratio of the shot noise power and the current at zero temperature, is simply given by

$$F = \frac{dP/dV}{dI/dV} = e\left(1 - \frac{h}{e^2}G\right). \tag{5.29}$$

It has the same one-parameter scaling and duality as G. The fact that higher order cumulants of the current have the same scaling as the differential conductance is a consequence of the single-point-contact geometry, with a single counting field $\chi(t)$. This does not carry over to a two-point-contact geometry.

Chapter 6

Isolated zeros in the spectral function as signature of a quantum continuum

6.1 Introduction

The energy levels of a generic quantum system can be organized either in discrete or continuum spectra. The discrete spectrum is associated with the existence of stable bound states, corresponding to localized long-lived quasiparticles with well defined energy, while the continuum spectrum reflects either multiparticle states with finite phase volume – e.g., particle-hole continuum, a thermodynamically large number of interacting degrees of freedom – a thermal bath, or the absence of quasiparticles as such – a quantum critical continuum. The qualitative difference between discrete states and continua is manifest in the spectral function: It either exhibits sharp peaks in the former case or a (peakless) smooth profile in the latter one. In more complicated quantum systems which have both discrete and continuum subparts, the spectral function can take a distinct shape. The well-known example is the Fano resonance [129–131], which arises when one probes the continuum in the presence of the isolated states, whose

The contents of this chapter have been published and reprinted with permission from N. Gnezdilov, A. Krikun, K. Schalm, and J. Zaanen, Phys. Rev. B **99**, 165149 (2019).

interference leads to a characteristic line shape with a neighboring peak and zero.

The continued strong interest in quantum criticality and various non-Fermi liquid models inherently concerns the study of a quantum system with a continuum rather than a discrete spectrum. A defining feature of the non-Fermi liquid is the absence of the stable quasiparticles. No discrete peaks are seen in the spectral function; rather it has the appearance of a power law [132]. The same type of spectra are characteristic of quantum critical systems [133], which are described by conformal field theory and a lack of the quasiparticles. Conformal field theories also generically exhibit power laws, controlled by the anomalous dimensions of the operators. These non-Fermi liquid and quantum critical ideas appear to be very relevant to the unconventional states of strongly correlated quantum matter, most notoriously the strange metal phase observed in high temperature superconductors and heavy fermion systems [134]. This experimental relevance in turn triggered the active theoretical effort in the last decades, aimed at building controlled models of non-Fermi liquids and/or quantum critical systems. Among the latest developments is the Sachdev-Ye-Kitaev model [27, 28], which has a power law spectral function due to the strong entanglement between the constituent fermions. A few proposals have arisen recently on the experimental realization of the SYK model [31, 32, 53], which makes the question about the observable properties of the quantum critical continuum especially important. This case of the $0 + 1$ dimensional "quantum dot" systems is special since the multiparticle phase space shrinks to zero and any observed continuum spectrum can not be of quasiparticle nature. Therefore the detection of continuum in a quantum dot signals the interesting physics, whether it is related to the particular SYK model or not.

In this paper we point out a very basic and therefore very general feature of quantum systems containing the continuum as a subpart. We show that the spectral function exhibits a distinct line shape characterized by an isolated zero arising when one probes a discrete subpart of the system that consists both of discrete states and a continuum. It is the "mirror" of the Fano resonance. A similar effect has been pointed out by one of us in the form of interference effects between different decay channels of the core holes created in high energy photoemission processes [130]. This distinct spectral function zero is in principle observable in experiment and it can therefore be used as a signature of the presence of

a continuum subpart in quantum systems, in particular in the laboratory realizations of quantum criticality. The important aspect is that this probe is *indirect* – it does not interact with the continuum system. This can be a significant advantage since the quantum critical systems are notoriously fragile and the direct measurement could easily destroy them.

We shall first discuss the generic mechanism of the phenomenon and then demonstrate how it works in several examples with continuum subsystems: (1) two single fermion quantum dots coupled to an SYK quantum dot, (2) a one-dimensional wire coupled to a chain of the SYK nodes, and (3) a holographic model of a local quantum critical system with a periodic lattice.

6.2 Isolated zeros in the spectral function

Consider two fermions χ_A, χ_B with discrete quasiparticle energies Ω_A, Ω_B, respectively, coupled to a fermion ψ with a continuum spectrum characterized by a Green's function $\mathcal{G}(\omega)$. The Euclidean action for the full system reads:

$$\begin{aligned} S &= S_\chi + S_\psi + S_{int}, \qquad (6.1)\\ S_\chi &= \int dt \sum_{\sigma=A,B} \bar{\chi}_\sigma \left(\partial_t + \Omega_\sigma\right) \chi_\sigma,\\ S_\psi &= -\int dt dt' \, \bar{\psi}(t) \mathcal{G}\left(t-t'\right)^{-1} \psi(t'),\\ S_{int} &= \int dt \sum_{\sigma=A,B} \left(\lambda_\sigma \, \bar{\psi} \, \chi_\sigma + \lambda^*_\sigma \bar{\chi}_\sigma \psi\right). \end{aligned}$$

As shown in Appendix 6.7.1 our effect is present for any tunneling couplings λ_σ, however for brevity here we consider the case $\lambda_A = \lambda_B \equiv \lambda$. Integrating out the fermion ψ in the continuum gives the Green's function for the fermions χ_A, χ_B:

$$G_{\sigma\sigma'}(\omega)^{-1} = \begin{pmatrix} \omega - \Omega_A - |\lambda|^2 \mathcal{G}(\omega) & -|\lambda|^2 \mathcal{G}(\omega) \\ -|\lambda|^2 \mathcal{G}(\omega) & \omega - \Omega_B - |\lambda|^2 \mathcal{G}(\omega) \end{pmatrix}. \qquad (6.2)$$

We are interested in the spectral function of a single fermion χ_A: $A_A(\omega) = -\frac{1}{\pi} \mathrm{Im} G^R_{AA}(\omega)$, where the retarded Green's function is obtained from the inverse of the matrix (6.2) after analytic continuation $\omega \to \omega + \mathrm{i}\delta \, \mathrm{sign}(\omega)$

with $\delta = 0^+$. The result is

$$A_A(\omega) = -\frac{|\lambda|^2}{\pi}\frac{\mathrm{Im}\mathcal{G}^R(\omega)}{|D(\omega)|^2}\,(\omega-\Omega_B)^2\,, \tag{6.3}$$
$$D(\omega)=(\omega-\Omega_A)(\omega-\Omega_B)-|\lambda|^2(2\omega-\Omega_A-\Omega_B)\mathcal{G}^R(\omega).$$

In (6.3) $\mathcal{G}^R$ is the retarded Green's function of the fermion ψ. Here we've taken the limit $\delta \to 0^+$ assuming the imaginary part of $\mathcal{G}^R$ stays finite. In Eqs. (6.14) and (6.30) in Appendices 6.7.1 and 6.7.2 we give the results for finite δ, i.e., a universal finite lifetime for the fermions $\chi_{A,B}$.

Our main observation is that the spectral function of fermion χ_A has a double zero exactly at the energy level of fermion χ_B: $\omega = \Omega_B$. The physics of the zero in (6.3) can be better understood by considering the matrix structure of the imaginary part of the Green's function

$$\mathrm{Im}G^R_{\sigma\sigma'} \sim \begin{pmatrix} (\omega-\Omega_B)^2 & (\omega-\Omega_B)(\omega-\Omega_A) \\ (\omega-\Omega_B)(\omega-\Omega_A) & (\omega-\Omega_A)^2 \end{pmatrix}. \tag{6.4}$$

This matrix is degenerate and has a single zero eigenvalue with eigenvector

$$|\chi_0\rangle = (\omega-\Omega_A)|\chi_A\rangle - (\omega-\Omega_B)|\chi_B\rangle\ . \tag{6.5}$$

In other words this linear combination of probes is completely oblivious to the continuum. One immediately sees that for $\omega = \Omega_B$ the probe fermion χ_A aligns with the "oblivious" combination and thus does not get absorbed/reflected. This explains the double zero at the resonance frequency. In the degenerate case $\Omega \equiv \Omega_A = \Omega_B$ the double zero at $\omega = \Omega$ is canceled by the same multiplying factor in the denominator $D(\omega)$ and it's easy to understand the absence of the effect: For any energy the combination (6.5) is now fixed to $|\chi_0\rangle \sim |\chi_A\rangle - |\chi_B\rangle$ and it never coincides with one of the probes.

Though similar, this occurrence of the double zero for the discrete probe is the obverse of the Fano resonance, as the latter follows when one integrates out the discrete fermions $\chi_{A,B}$. The Green's function for the continuum fermion ψ then becomes (setting the χ_B coupling to zero) $G^{-1}_{\psi\psi} = \mathcal{G}^{-1} - |\lambda|^2/(\omega-\Omega_A)$, with the spectral function

$$A_\psi(\omega) = -\frac{1}{\pi}\mathrm{Im}G^R_{\psi\psi}(\omega) = -\frac{1}{\pi}\frac{(\omega-\Omega_A)^2\mathrm{Im}\mathcal{G}^R(\omega)}{|\omega-\Omega_A-\lambda^2\mathcal{G}^R(\omega)|^2}. \tag{6.6}$$

The double zero at the energy $\omega = \Omega_A$ is again obvious but the pole structure is different. This Fano response has a pole at $\omega = \omega_p$ near Ω_A

shifted by the interaction with continuum. For small λ we can approximate its location as $\omega_p = \Omega_A + \lambda^2 \mathcal{G}(\Omega_A)$. In this case the spectrum function near the pole $\omega \sim \omega_p$ takes the familiar Fano form [131]

$$A_\psi \propto \frac{(\epsilon + q\Gamma)^2}{\epsilon^2 + \Gamma^2}, \tag{6.7}$$

with the parameters $\epsilon = (\omega - \Omega_A - \lambda^2 \mathrm{Re}\mathcal{G}(\Omega_A))$, $\Gamma = \lambda^2 \mathrm{Im}\mathcal{G}(\Omega_A)$, and $q = \mathrm{Re}\mathcal{G}(\Omega_A)/\mathrm{Im}\mathcal{G}(\Omega_A)$.

One obvious extension of the action is to include a direct coupling between fermions $S'_\chi = \int dt\, (\kappa \bar{\chi}_A \chi_B + \kappa^* \bar{\chi}_B \chi_A)$. We analyze this in Appendix 6.7.1. The complex zeros of the spectral function $A_A(\omega)$ are given in this case by $(\Omega_B - \mathrm{Re}\kappa \pm \mathrm{iIm}\kappa)$. The real part of the coupling shifts the position of the zero, while the imaginary one moves it off the real axis. In the latter case the exact real zero in the spectral function gets superseded by the localized depression with finite minimum value, but the overall line shape stays intact. This is reminiscent of the Fano resonance, where the exact zero is never observed in practice, but the full line shape points out the characteristic physics [130, 131].

6.3 SYK model

To give an **explicit example** of how this zero arises we first focus on the $0 + 1$ dimensional model featuring quantum critical continuum – the Sachdev-Ye-Kitaev (SYK) model [27, 28] with quartic interaction among complex fermions [47]. We couple the continuum SYK model at charge neutrality point ($\mu_{SYK} = 0$) to two discrete states with combined Hamil-

Figure 6.1. Cheburashkian geometry [135]. Two quantum dots with discrete energy levels Ω_A and Ω_B are symmetrically coupled to an SYK quantum dot.

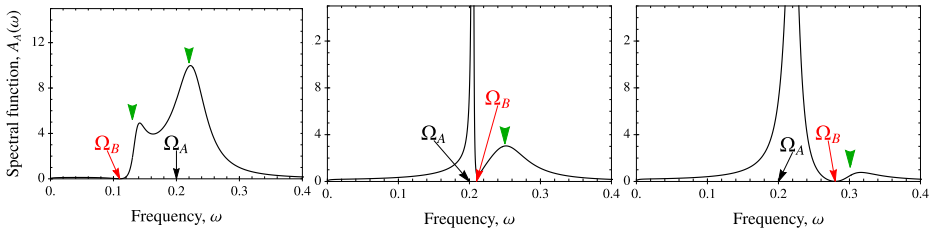

Figure 6.2. Isolated zero for the SYK model. For a given coupling to a continuum $\lambda = 0.135, F = 10$, the dependence of the spectral function of state A on the energy level of the state B is shown. The isolated zero is always present at Ω_B. The peak at Ω_A gets sharpened due to the proximity of zero, but is destroyed if $\Omega_A = \Omega_B$ [not shown, see Eq. (6.3)]. Green arrows show the positions of the poles of the Green's function defined as zeros of the determinant $D(\omega)$ in the spectral function in Eq. (6.3). Note that they do not coincide exactly with the maxima of the spectral function due to the proximity of zeros.

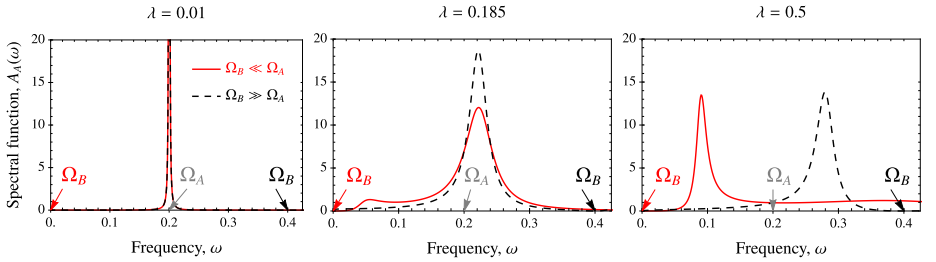

Figure 6.3. Asymptotic shape of the peak. Depending on the value of the coupling λ the shape of the peak at Ω_A may differ considerably in the asymptotic cases when $\Omega_B \ll \Omega_A$ (red lines) and $\Omega_B \gg \Omega_A$ (black lines). When $\lambda \ll 1$ (left panel) the two cases are identical, for intermediate values of λ (middle panel) the width of the peak changes, for strong coupling (right panel) the position of the peak is affected as well.

tonian

$$H = \sum_{\sigma=A,B} \Omega_\sigma \chi_\sigma^\dagger \chi_\sigma + H_{SYK} + H_{int}, \tag{6.8}$$

$$H_{SYK} = \frac{1}{(2N)^{3/2}} \sum_{i,j,k,l=1}^{N} J_{ij;kl}\, \psi_i^\dagger \psi_j^\dagger \psi_k \psi_l,$$

$$H_{int} = \frac{1}{\sqrt{N}} \sum_{i=1}^{N} \sum_{\sigma=A,B} \left(\lambda_i \psi_i^\dagger \chi_\sigma + \lambda_i^* \chi_\sigma^\dagger \psi_i \right).$$

The fermions χ_A, χ_B can be thought of as a pair of single state tunable quantum dots symmetrically coupled to the SYK system, the latter might be experimentally realized in a graphene flake based device [53]. We call it Cheburashkian geometry [135], Fig. 6.1. The random couplings $J_{ik;kl}$ and λ_i are independently distributed as Gaussian with zero mean $\overline{J_{ij;kl}} = 0 = \overline{\lambda_i}$ and finite variance $\overline{|J_{ij;kl}|^2} = J^2$ ($J_{ij;kl} = -J_{ji;kl} = -J_{ij;lk} = (J_{kl;ij})^*$), $\overline{|\lambda_i|^2} = \lambda^2$. After disorder averaging, one finds that in the large N, long time limit $1 \ll J\tau \ll N$ the spectral function $A_A(\omega)$ for the fermion χ_A coincides with Eq. (6.3), where the coupling strength is given by the variance $\overline{|\lambda_i|^2} = \lambda^2$ and the continuum $\mathcal{G}^R$ originates from the SYK Green's function

$$\mathcal{G}^R(\omega) = -\mathrm{i}\pi^{1/4}\frac{\mathrm{e}^{\mathrm{i}\pi\mathrm{sgn}(\omega)/4}}{\sqrt{J|\omega|}} \tag{6.9}$$

at zero temperature, see the details in Appendix 6.7.2.

The line shape of the spectral function of χ_A depends on the frequencies Ω_A and Ω_B in a characteristic manner. We give examples in Figs. 6.2 and 6.3. By tuning those one gets a distinct identifier of existence of the SYK continuum spectrum.

In case of multiple M states, a spectral function of a single state $A_A(\omega) \propto \mathrm{Im}\mathcal{G}^R(\omega)\prod_{m=1}^{M-1}(\omega - \Omega_{B_m})^2$ contains $M-1$ isolated zeros. This is described in Appendix 6.7.3, where we assume $M \ll N$ to avoid a transition in the SYK model to a Fermi liquid phase [122].

6.4 Cluster of SYK nodes

One can generalize the previous case by clustering evenly separated quantum SYK dots, coupled to a 1D wire [116, 136]. Here we can consider the itinerant fermion χ_p either in Galilean continuum or in an independent

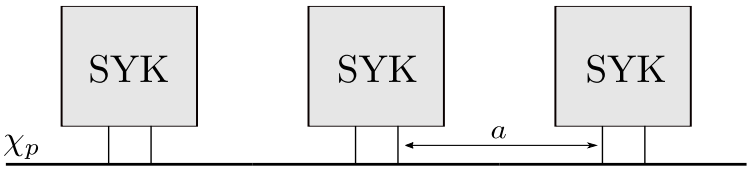

Figure 6.4. SYK chain. An evenly spaced chain of SYK impurities is introduced to the one-dimensional system with propagating fermion χ.

crystal with arbitrary periodicity. It has a given dispersion relation ξ_p and interacts locally with an SYK quantum dot at point x_n, see Fig. 6.4. The corresponding Hamiltonian is similar to Eq. (6.8) with

$$H = \sum_p \xi_p \chi_p^\dagger \chi_p + \sum_{x_n} H_{SYK}(x_n) + H_{int}(x_n), \tag{6.10}$$

$$H_{SYK}(x_n) = \frac{1}{(2N)^{3/2}} \sum_{i,j,k,l=1}^{N} J^n_{ij;kl}\, \psi^\dagger_{i,n} \psi^\dagger_{j,n} \psi_{k,n} \psi_{l,n},$$

$$H_{int}(x_n) = \frac{1}{\sqrt{N}} \sum_{i=1}^{N} \Big(\lambda_{i,n} \psi^\dagger_{i,n} \chi(x_n) + \lambda^*_{i,n} \chi^\dagger(x_n) \psi_{i,n} \Big).$$

It is clear that momentum plays now the role of the quantum number A, B in our earlier model (6.1). Therefore we are dealing with the case of many coupled states $M > 2$. Importantly however, the momentum modes are not all cross coupled through the interaction mediated by many SYK continua. As usual for the periodic structures, see Appendix 6.7.4, the SYK chain introduces an Umklapp-like effect: After integrating out all the SYK fermions the effective interaction only couples the momenta separated by the integer number of the reciprocal lattice units $\Delta p = 2\pi/a$. Note that only a discrete set of momentum modes is coupled, therefore the SYK fermions stay in the quantum critical phase. The inverse Green's function is labeled by the Bloch momentum p

$$G(p,\omega)^{-1} = \\ = \begin{pmatrix} \ddots & \cdots & \cdots \\ \vdots & \omega - \xi_p - \lambda^2 \mathcal{G}(\omega) & -\lambda^2 \mathcal{G}(\omega) \\ \vdots & -\lambda^2 \mathcal{G}(\omega) & \omega - \xi_{p-\Delta p} - \lambda^2 \mathcal{G}(\omega) \end{pmatrix}. \tag{6.11}$$

Following the same logic as before we find that the energy distribution of the spectral density at given momentum p has a discrete set of zeros at frequencies $\omega = \ldots, \xi_{p-\Delta p}, \xi_{p+\Delta p}, \xi_{p+2\Delta p}, \ldots$. Varying p this introduces continuous lines of zeros separated by Δp in the momentum resolved spectral function $A(p,\omega)$, as seen in Fig. 6.6, top panel. One can consider disordering the periodic structure by randomly shifting the nodes. The sharp lines in the Brillouin zone will smear out, since the Bloch momentum will not be well defined anymore. Therefore we expect the lines of zeros to smear out as well, but for the weak disorder the characteristic line shape will remain visible.

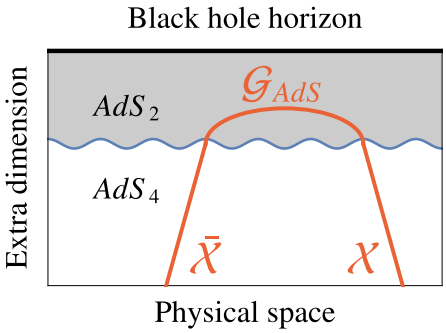

Figure 6.5. Holographic fermions. The spectral function of the fermion corresponds to the propagator in the holographic model. It is affected by the near horizon geometry, which induces locally critical continuum contribution $\mathcal{G}_{AdS}$.

6.5 Holographic fermions

This isolated zero phenomenon in the case of a finite number of spatial dimensions can be illustrated in a holographic model of a strange metal [137]. In this framework one describes strongly entangled quantum systems in terms of a classical gravitational problem with one extra dimension, see Fig. 6.5. At finite chemical potential these systems can flow to a novel "strange metal" low energy sector that exhibits local quantum criticality, i.e. it contains a continuum sector. The fermionic spectral function can be computed from the propagator of a dual holographic fermion $\mathcal{X}$ in the curved space with a charged black hole horizon. We refer the reader to the seminal works [138–140]. Importantly, the dynamics of a holographic fermion can be understood as a momentum dependent probe of the quantum critical continuum sector. In holographic models this sector is local, i.e. the system falls apart into local domains, each of which is a continuum theory in its own right [141]. The SYK model is an explicit proposal for the microscopic theory of one such domain. This explains why at low energy this holographic theory is similar to (6.10) with the SYK Hamiltonian replaced by the more abstract local quantum critical Hamiltonian [140]. The Green's function of the critical fermions ψ can be shown to have the scaling form $\mathcal{G}(\omega) \sim \omega^{2\nu_p}$, where ν_p depends on the momentum of the itinerant probe χ_p.

Unlike the case with an SYK chain, the holographic continuum comes from translationally invariant horizon, therefore it does not introduce the Brillouin zone by itself. The weak interaction between the localized contin-

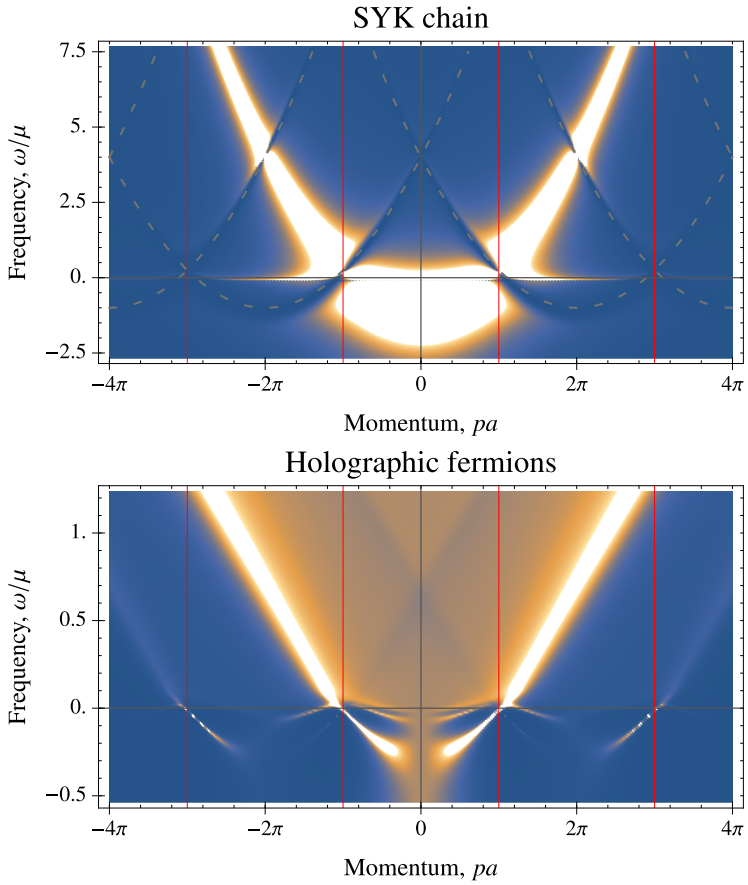

Figure 6.6. Lines of isolated zeros. Spectral density of a fermion is shown in color. The Brillouin zone boundaries are shown with red grid lines. The bright bands correspond to the dispersion relation of itinerant fermion ξ_p, while the finite background is due to the critical continuum. The lines of zeros are seen as darker bands and correspond to the dispersion of the Umklapp copies of the fermionic dispersion $\xi_{p\pm 2\pi/a}$. *Top panel*: **In SYK chain.** We use free space dispersion $\xi_p = p^2/2m - \mu$ with $\mu = 0.2, m = 0.5$, SYK Green's function (6.9) has $J = 10$, and the coupling is $\lambda = 0.3$. The gray dashed lines show the dispersions $\xi_{p\pm\Delta_p}$. *Bottom panel*: **In the holographic model for fermions on top of the continuum.** The model has periodic background with period a.

uum sectors effectively restores translational invariance. The appearance of isolated zeros in the holographic spectrum becomes apparent once one breaks translations by introducing a crystal lattice with period a. The

technical details of this construction are discussed in the specialized papers [142–145]. Importantly, in this case it is the periodic potential, which introduces the Bloch momentum and makes the dispersion ξ_p multivalued due to the appearance of the $\xi_{p-2\pi/a}$ and $\xi_{p+2\pi/a}$ copies. These branches are coupled by the near horizon continuum $\mathcal{G}(\omega)$, and this leads to the similar pattern in the spectral function as in the SYK chain case, see Fig. 6.6, bottom panel. At finite temperature the zeros are smeared and the spectral density never strictly vanishes. However the distinctive line shape is clearly recognizable.

6.6 Conclusion

We have observed a characteristic phenomenon which arises in quantum systems having both discrete spectrum and continuum subparts. The interference between the discrete parts mediated by the continuum gives rise to the isolated zeros in the spectral function of the one discrete state, which are located at the energy levels of the other states. It is the complement of the known Fano resonance. We derive this effect in full generality and show that it is present for a very general class of the continuum subsystems, provided their Green's functions have finite imaginary part and lack a pole structure.

By studying several examples with and without spatial dimensions, we see that the phenomenon is generally present. It is characterized by the distinctive "pole-zero" line shape, which is different from that of the Fano resonance, since the positions of the pole and zero are in principle independent of each other. We show that this line shape is not destroyed by the additional couplings or disorder: The exact zero gets smeared, but the localized depression remains. This leads us to propose that our finding can serve as a convenient experimental marker for a quantum system to include a continuum subpart, such as an SYK continuum in the graphene flake on a quantum dot or a local quantum critical phase in case of a strange metal.

6.7 Appendix: Outline of the calculation

6.7.1 Inclusion of general coupling between discrete levels

As in the main text, we consider two fermions coupled through continuum but with an additional direct coupling:

$$
\begin{aligned}
S &= S_\chi + S_\psi + S_{int}, \qquad (6.12)\\
S_\chi &= \int_0^\beta d\tau \begin{pmatrix} \bar\chi_A & \bar\chi_B \end{pmatrix} \begin{pmatrix} \partial_\tau + \Omega_A & \kappa \\ \kappa^* & \partial_\tau + \Omega_B \end{pmatrix} \begin{pmatrix} \chi_A \\ \chi_B \end{pmatrix},\\
S_\psi &= -\int_0^\beta d\tau \int_0^\beta d\tau'\, \bar\psi(\tau) \mathcal{G}\left(\tau-\tau'\right)^{-1} \psi(\tau'),\\
S_{int} &= \int_0^\beta d\tau \sum_{\sigma=A,B} \left(\lambda_\sigma\, \bar\psi\, \chi_\sigma + \lambda_\sigma^* \bar\chi_\sigma \psi\right),
\end{aligned}
$$

where κ is the direct coupling strength. After integration over the fermion ψ, we derive the inverse Green's function for the fermions χ_A, χ_B:

$$
G_{\sigma\sigma'}(\mathrm{i}\omega_n)^{-1} = \begin{pmatrix} \mathrm{i}\omega_n - \Omega_A - |\lambda_A|^2 \mathcal{G}(\mathrm{i}\omega_n) & -\kappa - \lambda_A^* \lambda_B\, \mathcal{G}(\mathrm{i}\omega_n) \\ -\kappa^* - \lambda_A \lambda_B^*\, \mathcal{G}(\mathrm{i}\omega_n) & \mathrm{i}\omega_n - \Omega_B - |\lambda_B|^2 \mathcal{G}(\mathrm{i}\omega_n) \end{pmatrix}, \quad (6.13)
$$

where $\omega_n = \pi T\,(2n+1)$ are Matsubara frequencies. Inversion of the matrix (6.13) and analytic continuation $\mathrm{i}\omega_n \to \omega + \mathrm{i}\delta$ with $\delta = 0^+$ gives the retarded Green's function:

$$
G^R_{\sigma\sigma'}(\omega) = \frac{1}{D(\omega)} \begin{pmatrix} \omega - \Omega_B + \mathrm{i}\delta - |\lambda_B|^2 \mathcal{G}^R(\omega) & \kappa + \lambda_A^* \lambda_B \mathcal{G}^R(\omega) \\ \kappa^* + \lambda_A \lambda_B^* \mathcal{G}^R(\omega) & \omega - \Omega_A + \mathrm{i}\delta - |\lambda_A|^2 \mathcal{G}^R(\omega) \end{pmatrix}, \quad (6.14)
$$

$$
\begin{aligned}
D(\omega) = {} & (\omega - \Omega_A + \mathrm{i}\delta)\,(\omega - \Omega_B + \mathrm{i}\delta) - |\kappa|^2 - \left(|\lambda_A|^2\,(\omega - \Omega_B + \mathrm{i}\delta)\right.\\
& \left. + |\lambda_B|^2\,(\omega - \Omega_A + \mathrm{i}\delta) + \kappa \lambda_A \lambda_B^* + \kappa^* \lambda_A^* \lambda_B\right) \mathcal{G}^R(\omega). \qquad (6.15)
\end{aligned}
$$

The spectral function for fermion χ_A is defined as the imaginary part of the AA block of (6.14):

$$
A_A(\omega) = -\frac{1}{\pi} \mathrm{Im} G^R_{AA}(\omega) = -\frac{|\lambda_A|^2}{\pi} \frac{\left|\omega - \Omega_B + \kappa\, \frac{\lambda_A \lambda_B^*}{|\lambda_A|^2}\right|^2}{|D(\omega)|^2}\, \mathrm{Im}\mathcal{G}^R(\omega). \quad (6.16)
$$

The imaginary part of the continuum Green's function $\mathcal{G}^R$ is supposed to be finite: $\mathrm{Im}\mathcal{G}^R \gg \delta = 0^+$, so that δ can be neglected in (6.16). Zeros of the spectral function (6.16) are given by solutions of the equation

$(\omega-\Omega_B)^2+2\mathrm{Re}\zeta\,(\omega-\Omega_B)+|\zeta|^2=0$, where $\zeta=\kappa\lambda_A\lambda_B^*/|\lambda_A|^2$. In case of the complex valued $\zeta=|\zeta|\mathrm{e}^{\mathrm{i}\varphi}$, the solutions are $\omega=\Omega_B-|\zeta|\cos\varphi\pm|\zeta|\sqrt{\cos^2\varphi-1}$. This results in the appearance of shifted isolated zeros at the real energy axis only for $\varphi=\pi m$: $\omega=\Omega_B+(-1)^{m+1}\,|\zeta|$, where m are integers. So, zeros of the spectral function (6.16) are stable for real values of ζ.

In case of negligibility of the direct coupling κ between the isolated states on the background of the frequencies of those, we restore the expression for the spectral function from the main text:

$$A_A(\omega)=-\frac{|\lambda_A|^2}{\pi}\frac{(\omega-\Omega_B)^2}{|D(\omega)|^2}\mathrm{Im}\mathcal{G}^R(\omega), \tag{6.17}$$

$$D(\omega)=(\omega-\Omega_A)(\omega-\Omega_B)-\Big(|\lambda_A|^2(\omega-\Omega_B)+|\lambda_B|^2\,(\omega-\Omega_A)\Big)\,\mathcal{G}^R(\omega).$$

The result (6.17) is valid for general couplings λ_σ.

6.7.2 Mean-field treatment of the SYK model with two component impurity

The Euclidean action for the Hamiltonian (8) in the main text after disorder averaging is

$$\begin{aligned}S=&\int_0^\beta d\tau\Big[\sum_{\sigma=A,B}\bar\chi_\sigma\,(\partial_\tau+\Omega_\sigma)\,\chi_\sigma+\sum_{i=1}^N\bar\psi_i\,\partial_\tau\psi_i\Big]\\&-\int_0^\beta d\tau\int_0^\beta d\tau'\Big[\frac{\lambda^2}{N}\sum_{i=1}^N\sum_{\sigma,\sigma'=A,B}\bar\chi_\sigma\psi_i(\tau)\,\bar\psi_i\chi_{\sigma'}(\tau')\\&+\frac{J^2}{4N^3}\sum_{i,j,k,l=1}^N\bar\psi_i\bar\psi_j\psi_k\psi_l(\tau)\bar\psi_l\,\bar\psi_k\psi_j\psi_i(\tau')\Big].\end{aligned} \tag{6.18}$$

Introduction of two pairs of nonlocal fields:

$$\begin{aligned}1_\psi=&\int\mathcal{D}G_\psi\,\delta\left(G_\psi(\tau',\tau)-\frac{1}{N}\sum_{i=1}^N\bar\psi_i(\tau)\psi_i(\tau')\right)=\\=&\int\mathcal{D}\Sigma_\psi\int\mathcal{D}G_\psi\exp\left[N\int_0^\beta d\tau\int_0^\beta d\tau'\,\Sigma_\psi(\tau,\tau')\right.\\&\left.\cdot\left(G_\psi(\tau',\tau)-\frac{1}{N}\sum_{i=1}^N\bar\psi_i(\tau)\psi_i(\tau')\right)\right]\end{aligned} \tag{6.19}$$

and

$$1_\chi = \int \mathcal{D}G_\psi\, \delta\left(G_\chi(\tau',\tau) - \sum_{\sigma,\sigma'=A,B} \bar{\chi}_\sigma(\tau)\chi_{\sigma'}(\tau')\right) = \\ = \int \mathcal{D}\Sigma_\chi \int \mathcal{D}G_\chi \exp\left[\int_0^\beta d\tau \int_0^\beta d\tau'\, \Sigma_\chi(\tau,\tau') \right. \\ \left. \cdot \left(G_\chi(\tau',\tau) - \sum_{\sigma,\sigma'=A,B} \bar{\chi}_\sigma(\tau)\chi_{\sigma'}(\tau')\right)\right] \tag{6.20}$$

allows us to rewrite the action (6.18) as

$$S = \int_0^\beta d\tau \int_0^\beta d\tau' \Bigg[\sum_{\sigma,\sigma'=A,B} \bar{\chi}_\sigma(\tau)\left(\delta_{\sigma\sigma'}\delta(\tau-\tau')(\partial_\tau+\Omega_\sigma)+\Sigma_\chi(\tau,\tau')\right)\chi_{\sigma'}(\tau') \\ + \sum_{i=1}^N \bar{\psi}_i(\tau)\left(\delta(\tau-\tau')\partial_\tau+\Sigma_\psi(\tau,\tau')\right)\psi_i(\tau') - \left(\Sigma_\chi(\tau,\tau')-\lambda^2 G_\psi(\tau,\tau')\right)G_\chi(\tau',\tau) \\ - N\left(\Sigma_\psi(\tau,\tau')G_\psi(\tau',\tau) + \frac{J^2}{4}G_\psi(\tau,\tau')^2 G_\psi(\tau',\tau)^2\right)\Bigg]. \tag{6.21}$$

Assuming that all nonlocal fields G_ψ, Σ_ψ, G_χ, and Σ_χ are the functions of $\tau-\tau'$, we get variational saddle-point equations:

$$G_\psi(\tau-\tau') = -\frac{1}{N}\sum_{i=1}^N \left\langle \mathrm{T}_\tau \psi_i(\tau)\bar{\psi}_i(\tau')\right\rangle, \tag{6.22}$$

$$\Sigma_\psi(\tau-\tau') = -J^2 G_\psi(\tau-\tau')^2 G_\psi(\tau'-\tau) + \frac{\lambda^2}{N}G_\chi(\tau-\tau'), \tag{6.23}$$

$$G_\chi(\tau-\tau') = -\sum_{\sigma,\sigma'=A,B} \left\langle \mathrm{T}_\tau \chi_\sigma(\tau)\bar{\chi}_{\sigma'}(\tau')\right\rangle, \tag{6.24}$$

$$\Sigma_\chi(\tau-\tau') = \lambda^2 G_\psi(\tau-\tau'), \tag{6.25}$$

where $G_\chi = \sum_{\sigma\sigma'} G_{\sigma\sigma'}$. In the large N and long time limit $1 \ll J\tau \ll N$, equations (6.22) and (6.23) are simplified to $G_\psi(\mathrm{i}\omega_n)^{-1} = -\Sigma_\psi(\mathrm{i}\omega_n)$ and $\Sigma_\psi(\tau-\tau') = -J^2 G_\psi(\tau-\tau')^2 G_\psi(\tau'-\tau)$ with a known zero temperature solution [47]:

$$G_\psi(\mathrm{i}\omega_n) = -\mathrm{i}\pi^{1/4}\frac{\mathrm{sgn}(\omega_n)}{\sqrt{J|\omega_n|}}. \tag{6.26}$$

Thus, we derived an effective action for the impurity fermions:

$$S = \sum_{n=-\infty}^{+\infty} \begin{pmatrix} \bar{\chi}_{n,A} & \bar{\chi}_{n,B} \end{pmatrix} G(\mathrm{i}\omega_n)^{-1} \begin{pmatrix} \chi_{n,A} \\ \chi_{n,B} \end{pmatrix}, \tag{6.27}$$

so that their Green's function is

$$G_{\sigma\sigma'}(\mathrm{i}\omega_n) = \frac{1}{D(\mathrm{i}\omega_n)} \begin{pmatrix} \mathrm{i}\omega_n - \Omega_B - \lambda^2 G_\psi(\mathrm{i}\omega_n) & \lambda^2 G_\psi(\mathrm{i}\omega_n) \\ \lambda^2 G_\psi(\mathrm{i}\omega_n) & \mathrm{i}\omega_n - \Omega_A - \lambda^2 G_\psi(\mathrm{i}\omega_n) \end{pmatrix}, \tag{6.28}$$

$$D(\mathrm{i}\omega_n) = (\mathrm{i}\omega_n - \Omega_A)\,(\mathrm{i}\omega_n - \Omega_B) - \lambda^2 (2\mathrm{i}\omega_n - \Omega_A - \Omega_B)\, G_\psi(\mathrm{i}\omega_n). \tag{6.29}$$

We perform analytic continuation $\mathrm{i}\omega \to \omega + \mathrm{i}\delta$ with $\delta = 0^+$ to derive the retarded Green's function:

$$G^R_{\sigma\sigma'}(\omega) = \frac{1}{D(\omega)} \begin{pmatrix} \omega - \Omega_B + \mathrm{i}\delta - \lambda^2 G^R_\psi(\omega) & \lambda^2 G^R_\psi(\omega) \\ \lambda^2 G^R_\psi(\omega) & \omega - \Omega_A + \mathrm{i}\delta - \lambda^2 G^R_\psi(\omega) \end{pmatrix}, \tag{6.30}$$

where

$$G^R_\psi(\omega) = -\mathrm{i}\pi^{1/4} \frac{\mathrm{e}^{\mathrm{i}\pi \mathrm{sgn}(\omega)/4}}{\sqrt{J|\omega|}}, \tag{6.31}$$

that fulfills $\mathrm{Im} G^R_\psi \gg \delta = 0^+$. The spectral function of the fermion χ_A is given by the imaginary part of the corresponding matrix element of (6.30)

$$A_A(\omega) = -\frac{1}{\pi} \mathrm{Im} G^R_{AA}(\omega) = -\frac{\lambda^2}{\pi} \frac{(\omega - \Omega_B)^2}{|D(\omega)|^2} \mathrm{Im} G^R_\psi(\omega), \tag{6.32}$$

where $\delta = 0^+$ is neglected. The result (6.16) coincides with the expression (3) in the main text for $\mathcal{G}^R \equiv G^R_\psi$.

6.7.3 Multiple states coupled to the SYK continuum

Here we address the case of M discrete states $\sigma = A, B_1, \ldots, B_{M-1}$ coupled to the SYK continuum. To stay in the non-Fermi liquid regime we suppose $M \ll N$ [122]. Once SYK degrees of freedom are integrated out,

the effective action for χ_σ fermions is similar to (6.27) in Appendix 6.7.2:

$$
\begin{aligned}
S &= \sum_{n=-\infty}^{+\infty} \sum_{\sigma,\sigma'=A,B_1,\ldots,B_{M-1}} \bar{\chi}_{n,\sigma} \left(\delta_{\sigma\sigma'} \left(-\mathrm{i}\omega_n + \Omega_\sigma \right) + \lambda^2 G_\psi(\mathrm{i}\omega_n) \right) \chi_{n,\sigma'} = \\
&= \sum_{n=-\infty}^{+\infty} \Bigg[\sum_{\sigma,\sigma'=A,B_1,\ldots,B_{M-2}} \bar{\chi}_{n,\sigma} \left(\delta_{\sigma\sigma'} \left(-\mathrm{i}\omega_n + \Omega_\sigma \right) + \lambda^2 G_\psi(\mathrm{i}\omega_n) \right) \chi_{n,\sigma'} \\
&\quad + \bar{\chi}_{n,B_{M-1}} \left(-\mathrm{i}\omega_n + \Omega_{B_{M-1}} + \lambda^2 G_\psi(\mathrm{i}\omega_n) \right) \chi_{n,B_{M-1}} \\
&\quad + \sum_{\sigma=A,B_1,\ldots,B_{M-2}} \lambda^2 G_\psi(\mathrm{i}\omega_n) \left(\bar{\chi}_{n,B_{M-1}} \chi_{n,\sigma} + \bar{\chi}_{n,\sigma} \chi_{n,B_{M-1}} \right) \Bigg] = \\
&= \sum_{n=-\infty}^{+\infty} \sum_{\sigma,\sigma'=A,B_1,\ldots,B_{M-2}} \bar{\chi}_{n,\sigma} \Bigg(\delta_{\sigma\sigma'} \left(-\mathrm{i}\omega_n + \Omega_\sigma \right) \\
&\quad + \lambda^2 \underbrace{\frac{\left(-\mathrm{i}\omega_n + \Omega_{B_{M-1}} \right) G_\psi(\mathrm{i}\omega_n)}{-\mathrm{i}\omega_n + \Omega_{B_{M-1}} + \lambda^2 G_\psi(\mathrm{i}\omega_n)}}_{\equiv G_{M-1}(\mathrm{i}\omega_n)} \Bigg) \chi_{n,\sigma'} = \\
&= \sum_{n=-\infty}^{+\infty} \sum_{\sigma,\sigma'=A,B_1,\ldots,B_{M-3}} \bar{\chi}_{n,\sigma} \Bigg(\delta_{\sigma\sigma'} \left(-\mathrm{i}\omega_n + \Omega_\sigma \right) \\
&\quad + \lambda^2 \underbrace{\frac{\left(-\mathrm{i}\omega_n + \Omega_{B_{M-2}} \right) G_{M-1}(\mathrm{i}\omega_n)}{-\mathrm{i}\omega_n + \Omega_{B_{M-2}} + \lambda^2 G_{M-1}(\mathrm{i}\omega_n)}}_{\equiv G_{M-2}(\mathrm{i}\omega_n)} \Bigg) \chi_{n,\sigma'} = \ldots = \\
&= \sum_{n=-\infty}^{+\infty} \bar{\chi}_{n,A} \Bigg(-\mathrm{i}\omega_n + \Omega_A + \lambda^2 \underbrace{\frac{\left(-\mathrm{i}\omega_n + \Omega_{B_1} \right) G_2(\mathrm{i}\omega_n)}{-\mathrm{i}\omega_n + \Omega_{B_1} + \lambda^2 G_2(\mathrm{i}\omega_n)}}_{\equiv G_1(\mathrm{i}\omega_n)} \Bigg) \chi_{n,A} \,, \qquad (6.33)
\end{aligned}
$$

where the derivation of the last line in (6.33) is based on the one-by-one Gaussian integration over all states except χ_A and G_ψ is given by the

expression (6.26). Now we restore G_1 back:

$$\begin{aligned} G_1(\mathrm{i}\omega_n) &= \frac{(-\mathrm{i}\omega_n+\Omega_{B_1})G_2(\mathrm{i}\omega_n)}{-\mathrm{i}\omega_n+\Omega_{B_1}+\lambda^2 G_2(\mathrm{i}\omega_n)} = \\ &= \frac{(-\mathrm{i}\omega_n+\Omega_{B_1})(-\mathrm{i}\omega_n+\Omega_{B_2})G_3(\mathrm{i}\omega_n)}{(-\mathrm{i}\omega_n+\Omega_{B_1})(-\mathrm{i}\omega_n+\Omega_{B_2})+\lambda^2 G_3(\mathrm{i}\omega_n)(-\mathrm{i}\omega_n+\Omega_{B_1}-\mathrm{i}\omega_n+\Omega_{B_2})} = \\ &= \frac{\prod_{m=1}^{3}(-\mathrm{i}\omega_n+\Omega_{B_m})\,G_4(\mathrm{i}\omega_n)}{\prod_{m=1}^{3}(-\mathrm{i}\omega_n+\Omega_{B_m})+\lambda^2 G_4(\mathrm{i}\omega_n)\sum_{m=1}^{3}\prod_{p\neq m}^{3}(-\mathrm{i}\omega_n+\Omega_{B_p})} = \dots \\ &= \frac{\prod_{m=1}^{M-1}(-\mathrm{i}\omega_n+\Omega_{B_m})G_\psi(\mathrm{i}\omega_n)}{\prod_{m=1}^{M-1}(-\mathrm{i}\omega_n+\Omega_{B_m})+\lambda^2 G_\psi(\mathrm{i}\omega_n)\sum_{m=1}^{M-1}\prod_{p\neq m}^{M-1}(-\mathrm{i}\omega_n+\Omega_{B_p})}. \end{aligned} \tag{6.34}$$

Finally,

$$\begin{aligned} G_{AA}(\mathrm{i}\omega_n) &= \frac{1}{D(\mathrm{i}\omega_n)}\Bigg(\prod_{m=1}^{M-1}(\mathrm{i}\omega_n-\Omega_{B_m}) \\ &\quad -\lambda^2 G_\psi(\mathrm{i}\omega_n)\sum_{m=1}^{M-1}\prod_{p\neq m}^{M-1}(\mathrm{i}\omega_n-\Omega_{B_p})\Bigg), \end{aligned} \tag{6.35}$$

$$\begin{aligned} D(\mathrm{i}\omega_n) &= (\mathrm{i}\omega_n-\Omega_A)\prod_{m=1}^{M-1}(\mathrm{i}\omega_n-\Omega_{B_m}) - \lambda^2 G_\psi(\mathrm{i}\omega_n) \\ &\quad \cdot\Bigg((\mathrm{i}\omega_n-\Omega_A)\sum_{m=1}^{M-1}\prod_{p\neq m}^{M-1}(\mathrm{i}\omega_n-\Omega_{B_p})+\prod_{m=1}^{M-1}(\mathrm{i}\omega_n-\Omega_{B_m})\Bigg). \end{aligned} \tag{6.36}$$

The spectral function we are interested is

$$\begin{aligned} A_A(\omega) &= -\frac{1}{\pi}\mathrm{Im}G_{AA}\left(\mathrm{i}\omega_n\to\omega+\mathrm{i}\delta\right) = \\ &= -\frac{\lambda^2}{\pi}\frac{\mathrm{Im}G_\psi^R(\omega)}{|D(\omega)|^2}\prod_{m=1}^{M-1}(\omega-\Omega_{B_m})^2. \end{aligned} \tag{6.37}$$

Result (6.37) coincides with the two fermion case (6.32) at $M=2$.

6.7.4 Effective momentum coupling by the SYK chain

Consider the action corresponding to the Hamiltonian of the SYK chain one with one-dimensional propagating fermions χ, which interact locally

with the SYK nodes. After integrating out the SYK fermions one can write down the effective interaction term in the action as

$$V_{\text{eff}} = \int dx dx' \lambda^2 \bar{\chi}(x) \mathcal{G}(x, x'|\omega) \chi(x'). \tag{6.38}$$

Locality of the interaction immediately means that

$$\mathcal{G}(x, x'|\omega) = \delta(x - x') \rho(x) \mathcal{G}(\omega), \tag{6.39}$$

where we introduce the "position density of nodes" $\rho(x)$ which is a collection of periodically distributed delta functions in the case of a chain $\rho(x) = \sum_n \delta(x + na)$. Moving to momentum space gives

$$V_{\text{eff}} = \int dp\, d\Delta p\, \lambda^2 \bar{\chi}_p \chi_{p+\Delta p}\, \rho(\Delta p) \mathcal{G}(\omega), \tag{6.40}$$

where $\rho(\Delta p)$ is simply a Fourier transform of $\rho(x)$. For the periodically distributed chain it has the form $\rho(\Delta p) = \sum_n \delta(\Delta p + 2\pi n/a)$, which brings the interaction term to the form used in expression (6.11) of the main text.

$$V_{\text{eff}} = \int dp \sum_n \lambda^2 \bar{\chi}_p \chi_{p-2\pi n/a} \mathcal{G}(\omega). \tag{6.41}$$

Chapter 7

Gapless odd-frequency superconductivity induced by the Sachdev-Ye-Kitaev model

7.1 Introduction

In this Chapter we consder the SYK model with Majorana fermions. We modify the model via coupling it to a single-state non-interacting quantum dot. As we add only a single fermion, this model stays far away from the non-Fermi liquid/Fermi liquid transition [122] and it is still exactly solvable in the large N limit. We demonstrate that the effective theory for the fermion in the quantum dot gains the anomalous pairing terms, that make the quantum dot superconducting. Despite the induced superconductivity, the density of states in the quantum dot has no excitation gap. It has been a while since the phenomenon of gapless superconductivity was found in the superconductors with magnetic impurities, where for a specific range of concentration of those, a part of electrons does not

The contents of this chapter have been published and reprinted with permission from N. V. Gnezdilov, Phys. Rev. B **99**, 024506 (2019).

participate in the condensation process [146, 147]. The anomalous components of the Gor'kov Green's function [148, 149] of the quantum dot are calculated exactly in the large N limit and are odd functions of frequency [150, 151]. Odd-frequency pairing is known to be induced by proximity to an unconventional superconductor [151–154]. Below we obtain induced odd-frequency gapless superconductivity in zero dimensions as a consequence of the proximity to a system described by the SYK model [31, 32]. We suggest to use this effect as a way to detect the SYK-like effective behavior in a solid-state system.

7.2 The model

Let's consider the Sachdev-Ye-Kitaev model [27, 29] randomly coupled to a single state quantum dot [155] with the frequency Ω_d. The Hamiltonian of the system reads:

$$H=\Omega_d d^\dagger d+\sum_{i=1}^{N}\lambda_i\gamma_i\left(d^\dagger-d\right)+\frac{1}{4!}\sum_{i,j,k,l=1}^{N}J_{ijkl}\gamma_i\gamma_j\gamma_k\gamma_l\,, \tag{7.1}$$

where the couplings J_{ijkl} and λ_i are independently distributed as a Gaussian with zero mean $\overline{J_{ijkl}}=0=\overline{\lambda_i}$ and finite variance $\overline{J_{ijkl}^2}=3!J^2/N^3$, $\overline{\lambda_i^2}=\lambda^2/N$. The tunneling term in the Hamiltonian (7.1) is similar to one, that appears for tunneling into Majorana nanowires [15, 80, 152, 156, 157].

Once the disorder averaging is done, we decouple the interactions by introducing four pairs of the non-local fields in the Euclidean action as a resolution of unity [27, 29]:

$$1=\int\mathcal{D}\Sigma_\gamma\mathcal{D}G_\gamma \mathrm{e}^{\int d\tau d\tau'\frac{\Sigma_\gamma(\tau,\tau')}{2}\left(NG_\gamma(\tau',\tau)-\sum_i\gamma_i(\tau)\gamma_i(\tau')\right)}, \tag{7.2}$$

$$1=\int\mathcal{D}\Sigma_d\mathcal{D}G_d \mathrm{e}^{\int d\tau d\tau'\Sigma_d(\tau,\tau')\left(G_d(\tau',\tau)-\bar{d}(\tau)d(\tau')\right)}, \tag{7.3}$$

$$1=\int\mathcal{D}\Xi_d\mathcal{D}F_d \mathrm{e}^{\int d\tau d\tau'\Xi_d(\tau,\tau')\left(F_d(\tau',\tau)-d(\tau)d(\tau')\right)}, \tag{7.4}$$

$$1=\int\mathcal{D}\bar{\Xi}_d\mathcal{D}\bar{F}_d \mathrm{e}^{\int d\tau d\tau'\bar{\Xi}_d(\tau,\tau')\left(\bar{F}_d(\tau',\tau)-\bar{d}(\tau)\bar{d}(\tau')\right)}. \tag{7.5}$$

A variation of the effective action, which is given in Appendix 7.5, with respect to $G_\gamma, G_d, F_d, \bar{F}_d$ and $\Sigma_\gamma, \Sigma_d, \Xi_d, \bar{\Xi}_d$ produces self-consistent Schwinger-Dyson equations [149], that relate those fields to the Green's functions and

self-energies of Majorana fermions and the fermion in the quantum dot:

$$\Sigma_d(\tau) = \lambda^2 G_\gamma(\tau), \tag{7.6}$$

$$\Xi_d(\tau) = -\frac{\lambda^2}{2} G_\gamma(\tau), \quad \bar{\Xi}_d(\tau) = -\frac{\lambda^2}{2} G_\gamma(\tau), \tag{7.7}$$

$$\Sigma_\gamma(\tau) = J^2 G_\gamma(\tau)^3 + \frac{2\lambda^2}{N}\Big(G_d(\tau) - \frac{F(\tau)}{2} - \frac{\bar{F}(\tau)}{2}\Big), \tag{7.8}$$

$$G_\gamma(\mathrm{i}\omega_n) = \Big(\mathrm{i}\omega_n - \Sigma_\gamma(\mathrm{i}\omega_n)\Big)^{-1}. \tag{7.9}$$

The Green's function of Majorana fermions (independent from the site i) is $G_\gamma(\tau) = -N^{-1}\sum_i \langle \mathcal{T}_\tau\, \gamma_i(\tau)\gamma_i(0)\rangle$ and $G_d(\tau) = -\Big\langle \mathcal{T}_\tau\, d(\tau)\bar{d}(0)\Big\rangle$, $F_d(\tau) = -\langle \mathcal{T}_\tau\, d(\tau)d(0)\rangle$, $\bar{F}_d(\tau) = -\Big\langle \mathcal{T}_\tau\, \bar{d}(\tau)\bar{d}(0)\Big\rangle$ are normal and anomalous Green's functions of the quantum dot variables.

We are focused on the large N, long time limit $1 \ll J\tau \ll N$, where the conformal symmetry of the SYK model emerges [27, 29]. In this regime, the backreaction of the quantum dot on Majoranas self-energy (7.8) is suppressed as $1/N$. The bare frequency in the equation (7.9) can also be omitted at low frequencies. Thus, equations (7.8, 7.9) become $\Sigma_\gamma(\tau) = J^2 G_\gamma(\tau)^3$ and $G_\gamma(\mathrm{i}\omega_n) = -\Sigma_\gamma(\mathrm{i}\omega_n)^{-1}$, which are the same as in the case of the isolated SYK model. These equations have a known zero temperature solution [27, 29] $G_\gamma(\mathrm{i}\omega_n) = -\mathrm{i}\pi^{1/4}\mathrm{sgn}(\omega_n)\,(J|\omega_n|)^{-1/2}$, which contributes to the self-energies (7.6, 7.7) of the quantum dot. The Green's function of Majorana zero-modes has no pole structure, which manifests the absence of quasiparticles. Moreover, it behaves as a power-law of frequency, which is the case of quantum criticality [**Sac11**] and emergence of the conformal symmetry in the SYK case [27, 29].

7.3 SYK proximity effect

The effective action for the fermion in the quantum dot acquires anomalous terms

$$S_{\text{eff}} = -\frac{1}{2}\sum_{n=-\infty}^{+\infty} \begin{pmatrix} \bar{d}_n & d_{-n} \end{pmatrix} \mathcal{G}(\mathrm{i}\omega_n)^{-1} \begin{pmatrix} d_n \\ \bar{d}_{-n} \end{pmatrix}, \tag{7.10}$$

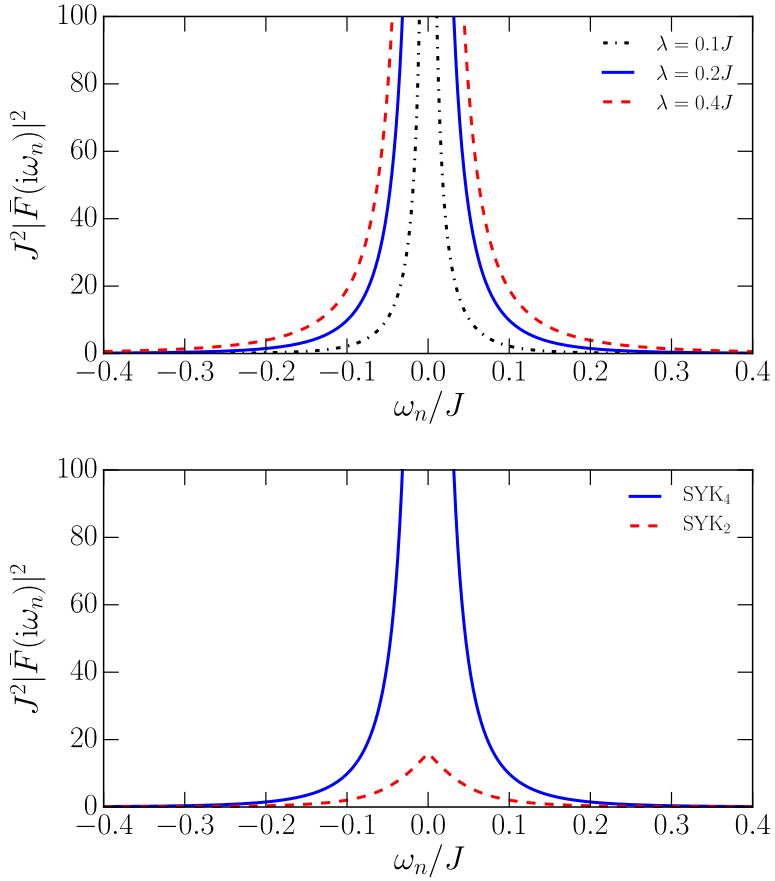

Figure 7.1. *Top panel*: Absolute value of the **anomalous averages** in the quantum dot coupled to the SYK model as a function of Matsubara frequency. The frequency of the quantum dot is $\Omega_d = 0.1J$. *Bottom panel*: **Anomalous averages** in the quantum dot coupled to the **SYK/SYK$_2$** model. The frequency of the dot is $\Omega_d = 0.1J$ and the coupling strength is $\lambda = 0.2J$.

where the Gor'kov Green's function [148, 149]

$$\mathcal{G}(i\omega_n)^{-1} = \begin{pmatrix} i\omega_n - \Omega_d - \lambda^2 G_\gamma(i\omega_n) & \lambda^2 G_\gamma(i\omega_n) \\ \lambda^2 G_\gamma(i\omega_n) & i\omega_n + \Omega_d - \lambda^2 G_\gamma(i\omega_n) \end{pmatrix} \tag{7.11}$$

is found self-consistently in a one loop expansion [149]. Due to negligibility of the last term in Majoranas self-energy (7.8) mentioned above, the one

loop approximation turns out to be exact in the large N limit. A detailed derivation of the formula (7.11) is presented in Appendix 7.5.

Appearance of the anomalous pairing terms $\bar{d}(\tau)G_\gamma(\tau-\tau')\bar{d}(\tau')$ in the effective action (7.10) does not require any additional quantum numbers, because those are "glued" by the nonlocality in the imaginary time that originates from the SYK saddle-point solution. The anomalous Green's function which follows from (7.11) is odd in frequency [150, 151]:

$$\begin{aligned}\bar{F}(\mathrm{i}\omega_n) &= -\frac{\lambda^2 G_\gamma(\mathrm{i}\omega_n)}{\mathrm{i}\omega_n\left(\mathrm{i}\omega_n - 2\lambda^2 G_\gamma(\mathrm{i}\omega_n)\right) - \Omega_d^2} = \\ &= -\bar{F}(-\mathrm{i}\omega_n).\end{aligned} \tag{7.12}$$

This result (7.12) is well aligned with previously found proximity effect by Majorana zero modes [80, 152] and odd-frequency correlations found in interacting Majorana fermions [158]. Superconducting pairing grows smoothly while the coupling increases as it is shown in Fig. 7.1, top panel.

It is worthwhile to compare our setting (7.1) to the case when the SYK quantum dot is replaced by a disordered Fermi liquid. The latter can be described by the SYK_2 model: $H_{\mathrm{SYK}_2} = \mathrm{i}\sum_{ij} J_{ij}\gamma_i\gamma_j$. In the long time limit, the Green's function of the SYK_2 model is $G_{\mathrm{SYK}_2}(\mathrm{i}\omega_n) = -\mathrm{i}\,\mathrm{sgn}(\omega_n)/J$ [32], which is substituted to the result for the anomalous component of the Gor'kov function (7.12). As we show in Fig. 7.1 (bottom panel), the amount of the SYK induced superconductivity is sufficiently higher then in the case of the SYK_2 model.

In the large N limit, the spectral function of the quantum dot is

$$\begin{aligned}A(\omega) &= -\frac{1}{\pi}\mathrm{Im}\,\mathrm{tr}\mathcal{G}\left(\mathrm{i}\omega_n \to \omega + \mathrm{i}\delta\right) = \\ &= -\frac{2}{\pi}\frac{\lambda^2\left(\omega^2+\Omega_d^2\right)\mathrm{Im}G_\gamma^R(\omega)}{\left|\omega\left(\omega - 2\lambda^2 G_\gamma^R(\omega)\right) - \Omega_d^2\right|^2},\end{aligned} \tag{7.13}$$

where $\delta = 0^+$ and $G_\gamma^R(\omega) = -\mathrm{i}\pi^{1/4}\mathrm{e}^{\mathrm{i}\pi\mathrm{sgn}(\omega)/4}\left(J|\omega|\right)^{-1/2}$. The broadening $\delta = 0^+$ of the fermion in the quantum dot is neglected once the imaginary part of the SYK Green's function is finite: $\lambda^2\mathrm{Im}G_\gamma^R(\omega) \gg \delta = 0^+$.

In absence of coupling between the single-state quantum dot and the SYK model ($\lambda = 0$), there is no particle-hole mixing. Superconducting pairing (Fig. 7.1) appears in the regime of intermediate coupling. The absence of the gap in the presence of the anomalous pairing reveals gapless superconductivity [146, 147] in zero dimensions, which can be probed by

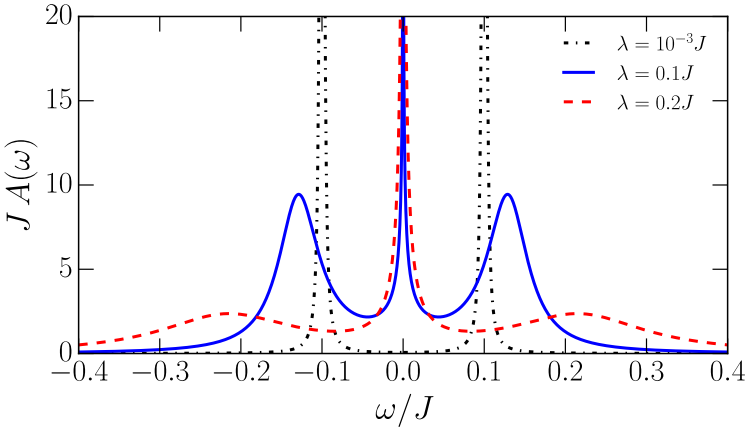

Figure 7.2. Density of states in the quantum dot at zero temperature as a function of frequency. $\Omega_d = 0.1J$ and $\delta = 10^{-3}J$.

Andreev reflection [77] in the tunneling experiment. The wide broadening of the peaks in Fig. 7.2 is due to the binding of the fermionic quantum dot with the SYK quantum critical continuum. Increasing of coupling strength λ results in grows of the anomalous pairing (7.12) and suppression of the initial quasiparticle peaks. In strong coupling the system shows divergent behavior at $\omega = 0$. However, the divergence point might be addressed beyond the conformal limit [119] $\omega \lesssim J/(N \log N)$. This changes the scaling of the SYK Green's function from $1/\sqrt{\omega}$ to $N \log N \sqrt{\omega}$ in the infrared.

In Fig. 7.3 we show, that the behavior of the spectral function of the quantum dot coupled to the SYK model is qualitatively different from the SYK_2 case. The SYK_2 model, mentioned above, describes disordered Fermi liquid and has a constant density of states $\propto 1/J$ in the long time limit.

At finite temperature the saddle-point solution of the SYK model is given by [47]:

$$G^R_\gamma(\omega) = -\mathrm{i}\pi^{1/4}\sqrt{\frac{\beta}{2\pi J}}\,\frac{\Gamma\left(\frac{1}{4} - \mathrm{i}\frac{\beta\omega}{2\pi}\right)}{\Gamma\left(\frac{3}{4} - \mathrm{i}\frac{\beta\omega}{2\pi}\right)}, \tag{7.14}$$

where $\beta = 1/T$ is inverse temperature and $\Gamma(x)$ is the Gamma function. We substitute the finite temperature SYK Green's function (7.14) in the spectral function of d fermion (7.13). Fig. 7.4 demonstrates that the di-

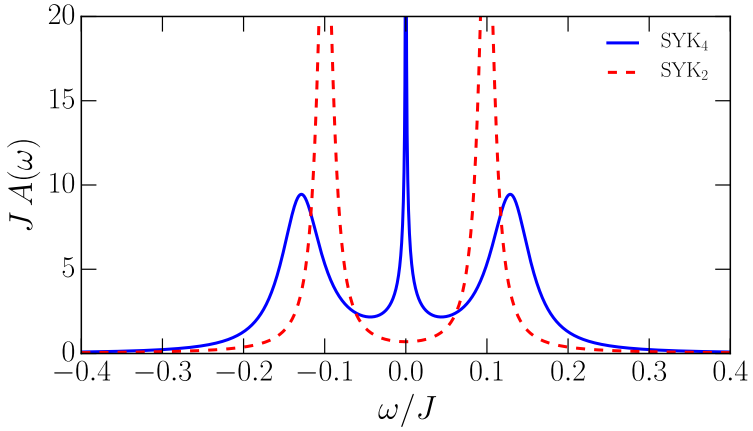

Figure 7.3. Density of states in the quantum dot coupled to the **SYK/SYK$_2$** model at zero temperature. The coupling strength is $\lambda = 0.1J$ and the frequency of the single state is $\Omega_d = 0.1J$.

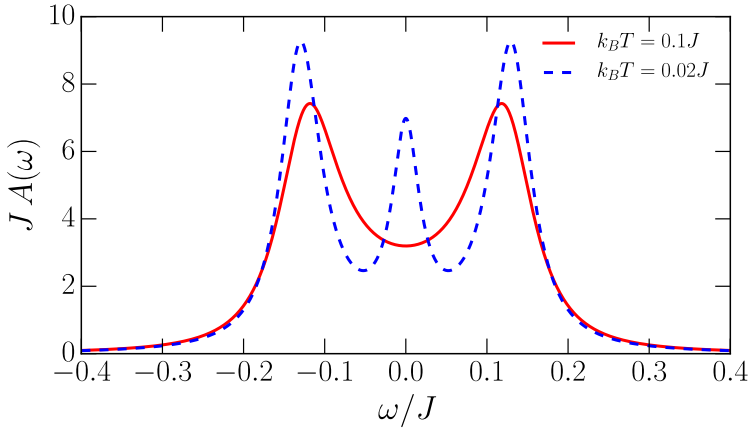

Figure 7.4. Density of states in the quantum dot at finite temperature as a function of frequency. The parameters are $\lambda/J = 0.1 = \Omega_d/J$.

vergence around $\omega \sim 0$ in the quantum dot density of states is regularized at finite temperature.

7.4 Conclusion

In this paper, we have shown that a single-state spinless quantum dot becomes superconducting in proximity to a structure whose low-energy behavior can be captured by the Sachdev-Ye-Kitaev model. Anomalous averages are found exactly in the large N limit and turn out to be odd functions of frequency. Appearance of non-zero superconducting pairing does not require any additional quantum numbers like spin, because it originates from nonlocality of the SYK saddle-point solution. Induced superconductivity strikes in the intermediate coupling between the quantum dot and the SYK model. At stronger coupling, the quasiparticle peaks are smeared out on the background of the SYK quantum critical continuum. We propose to use the peculiar property of the induced gapless superconductivity in zero dimensions to characterize the solid-state systems, that can be described by the SYK model as an effective theory in a certain limit.

7.5 Appendix: Gor'kov Green's function for the QD variables

The Euclidean action that corresponds to the Hamiltonian (7.1) after disorder averaging is

$$\begin{aligned} S = &\int_0^\beta d\tau \left[\bar{d} \left(\partial_\tau + \Omega_d \right) d + \frac{1}{2} \sum_{i=1}^N \gamma_i \partial_\tau \gamma_i \right] \\ &- \int_0^\beta d\tau \int_0^\beta d\tau' \Big[\frac{\lambda^2}{2N} \sum_{i=1}^N \gamma_i \left(\bar{d} - d \right)(\tau) \gamma_i \left(\bar{d} - d \right)(\tau') \\ &+ \frac{J^2}{8N} \sum_{i,j,k,l=1}^N \gamma_i \gamma_j \gamma_k \gamma_l(\tau) \gamma_l \gamma_k \gamma_j \gamma_i(\tau') \Big] . \end{aligned} \tag{7.15}$$

We introduce four pairs of nonlocal fields as a resolution of unity:

$$
\begin{aligned}
1 &= \int \mathcal{D}G_\gamma \, \delta \left(G_\gamma(\tau', \tau) - \frac{1}{N} \sum_{i=1}^{N} \gamma_i(\tau) \gamma_i(\tau') \right) = \\
&= \int \mathcal{D}\Sigma_\gamma \int \mathcal{D}G_\gamma \exp \left[\frac{N}{2} \int_0^\beta d\tau \int_0^\beta d\tau' \, \Sigma_\gamma(\tau, \tau') \right. \\
&\quad \left. \cdot \left(G_\gamma(\tau', \tau) - \frac{1}{N} \sum_{i=1}^{N} \gamma_i(\tau) \gamma_i(\tau') \right) \right],
\end{aligned} \tag{7.16}
$$

$$
\begin{aligned}
1 &= \int \mathcal{D}G_d \, \delta \Big(G_d(\tau', \tau) - \bar{d}(\tau) d(\tau') \Big) = \\
&= \int \mathcal{D}\Sigma_d \int \mathcal{D}G_d \exp \left[\int_0^\beta d\tau \int_0^\beta d\tau' \, \Sigma_d(\tau, \tau') \right. \\
&\quad \left. \cdot \Big(G_d(\tau', \tau) - \bar{d}(\tau) d(\tau') \Big) \right],
\end{aligned} \tag{7.17}
$$

$$
\begin{aligned}
1 &= \int \mathcal{D}F_d \, \delta \Big(F_d(\tau', \tau) - d(\tau) d(\tau') \Big) = \\
&= \int \mathcal{D}\Xi_d \int \mathcal{D}F_d \exp \left[\int_0^\beta d\tau \int_0^\beta d\tau' \, \Xi_d(\tau, \tau') \right. \\
&\quad \left. \cdot \Big(F_d(\tau', \tau) - d(\tau) d(\tau') \Big) \right],
\end{aligned} \tag{7.18}
$$

$$
\begin{aligned}
1 &= \int \mathcal{D}\bar{F}_d \, \delta \Big(\bar{F}_d(\tau', \tau) - \bar{d}(\tau') \bar{d}(\tau) \Big) = \\
&= \int \mathcal{D}\bar{\Xi}_d \int \mathcal{D}\bar{F}_d \exp \left[\int_0^\beta d\tau \int_0^\beta d\tau' \, \bar{\Xi}_d(\tau, \tau') \right. \\
&\quad \left. \cdot \Big(\bar{F}_d(\tau', \tau) - \bar{d}(\tau) \bar{d}(\tau') \Big) \right].
\end{aligned} \tag{7.19}
$$

This allows us to rewrite the action (7.15) as:

$$
\begin{aligned}
S = \int_0^\beta d\tau \int_0^\beta d\tau' \Big[& \bar{d}(\tau)\Big(\delta(\tau-\tau')\left(\partial_\tau + \Omega_d\right) + \Sigma_d(\tau,\tau')\Big) d(\tau') \\
& + \bar{d}(\tau)\bar{\Xi}_d(\tau,\tau')\bar{d}(\tau') + d(\tau)\Xi_d(\tau,\tau')d(\tau') \\
& + \frac{1}{2}\sum_{i=1}^{N} \gamma_i(\tau)\Big(\delta(\tau-\tau')\partial_\tau + \Sigma_\gamma(\tau,\tau')\Big)\gamma_i(\tau') \\
& - \Sigma_d(\tau,\tau')G_d(\tau',\tau) - \Xi_d(\tau,\tau')F_d(\tau',\tau) - \bar{\Xi}_d(\tau,\tau')\bar{F}_d(\tau',\tau) \\
& - \frac{N}{2}\left(\Sigma_\gamma(\tau,\tau')G_\gamma(\tau',\tau) + \frac{J^2}{4}G_\gamma(\tau,\tau')^4\right) \\
& - \frac{\lambda^2}{2}G_\gamma(\tau,\tau')\Big(G_d(\tau,\tau') - G_d(\tau',\tau) + F_d(\tau',\tau) + \bar{F}_d(\tau',\tau)\Big)\Big]. \quad (7.20)
\end{aligned}
$$

Following Refs. [27–29, 47], we assume that all nonlocal fields are odd functions of the time difference $\tau - \tau'$. In the large N, long time limit: $1 \ll J\tau \ll N$, self-consistent saddle-point equations are

$$
\begin{aligned}
\frac{\delta S}{\delta \Sigma_d} &= 0 \Rightarrow G_d(\tau-\tau') = -\left\langle \mathcal{T}_\tau\, d(\tau)\bar{d}(\tau')\right\rangle , && (7.21)\\
\frac{\delta S}{\delta \Xi_d} &= 0 \Rightarrow F_d(\tau-\tau') = -\left\langle \mathcal{T}_\tau\, d(\tau)d(\tau')\right\rangle && (7.22)\\
\frac{\delta S}{\delta \bar{\Xi}_d} &= 0 \Rightarrow \bar{F}_d(\tau-\tau') = -\left\langle \mathcal{T}_\tau\, \bar{d}(\tau)\bar{d}(\tau')\right\rangle , && (7.23)\\
\frac{\delta S}{\delta \Sigma_\gamma} &= 0 \Rightarrow G_\gamma(\tau-\tau') = -\frac{1}{N}\sum_{i=1}^{N}\left\langle \mathcal{T}_\tau\, \gamma_i(\tau)\gamma_i(\tau')\right\rangle \Rightarrow \\
&\qquad \Rightarrow G_\gamma(\mathrm{i}\omega_n)^{-1} = \mathrm{i}\omega_n - \Sigma_\gamma(\mathrm{i}\omega_n) \simeq -\Sigma_\gamma(\mathrm{i}\omega_n) && (7.24)
\end{aligned}
$$

and

$$\frac{\delta S}{\delta G_d} = 0 \Rightarrow \Sigma_d(\tau-\tau') = \lambda^2 G_\gamma(\tau-\tau')\,, \tag{7.25}$$

$$\frac{\delta S}{\delta F_d} = 0 \Rightarrow \Xi_d(\tau-\tau') = -\frac{\lambda^2}{2} G_\gamma(\tau-\tau') \tag{7.26}$$

$$\frac{\delta S}{\delta \bar{F}_d} = 0 \Rightarrow \bar{\Xi}_d(\tau-\tau') = -\frac{\lambda^2}{2} G_\gamma(\tau-\tau')\,, \tag{7.27}$$

$$\begin{aligned}\frac{\delta S}{\delta G_\gamma} = 0 \Rightarrow \Sigma_\gamma(\tau-\tau') &= J^2 G_\gamma(\tau-\tau')^3 \\ &+ \frac{\lambda^2}{N}\Big(2G_d(\tau-\tau') - F_d(\tau-\tau') - \bar{F}_d(\tau-\tau')\Big) \\ &\simeq J^2 G_\gamma(\tau-\tau')^3\,. \end{aligned} \tag{7.28}$$

Green's functions of the fermion in the dot enter the equation for the Majoranas self-energy (7.28) as $1/N$, so we neglect them in the large N limit. Thus, equations (7.24, 7.28) are decoupled from the quantum dot and become the standard SYK Schwinger-Dyson equations [27, 29] $G_\gamma(\mathrm{i}\omega_n)^{-1} = -\Sigma_\gamma(\mathrm{i}\omega_n)$ and $\Sigma_\gamma(\tau) = J^2 G_\gamma(\tau)^3$ with a known low-frequency solution

$$G_\gamma(\mathrm{i}\omega_n) = -\mathrm{i}\pi^{1/4}\frac{\mathrm{sgn}(\omega_n)}{\sqrt{J|\omega_n|}} \tag{7.29}$$

at zero temperature, where $\omega_n = \pi T(2n+1)$ are Matsubara frequencies. Meanwhile, the bare SYK Green's function (7.29) enters the self-energies of the quantum dot (7.25, 7.26, 7.27), that, according to the definitions (7.17, 7.18, 7.19), give both normal ($\bar{d}d$) and anomalous ($\bar{d}\bar{d}$, dd) components of the effective action for the d fermion.

The effective action for the fermion in the quantum dot in the basis of $\vec{d}_n^* = \frac{1}{\sqrt{2}}\begin{pmatrix}\bar{d}_n & d_{-n}\end{pmatrix}$, $\vec{d}_n = \frac{1}{\sqrt{2}}\begin{pmatrix}d_n & \bar{d}_{-n}\end{pmatrix}^T$ is given by

$$S = \sum_{n=-\infty}^{+\infty} \vec{d}_n^* \begin{pmatrix} -\mathrm{i}\omega_n + \Omega_d + \lambda^2 G_\gamma(\mathrm{i}\omega_n) & -\lambda^2 G_\gamma(\mathrm{i}\omega_n) \\ -\lambda^2 G_\gamma(\mathrm{i}\omega_n) & -\mathrm{i}\omega_n - \Omega_d + \lambda^2 G_\gamma(\mathrm{i}\omega_n) \end{pmatrix} \vec{d}_n, \tag{7.30}$$

so that the Gor'kov Green's function [148] composed from (7.21, 7.22) is found exactly in the large N limit:

$$\mathcal{G}(\mathrm{i}\omega_n)^{-1} = \begin{pmatrix} \mathrm{i}\omega_n - \Omega_d - \lambda^2 G_\gamma(\mathrm{i}\omega_n) & \lambda^2 G_\gamma(\mathrm{i}\omega_n) \\ \lambda^2 G_\gamma(\mathrm{i}\omega_n) & \mathrm{i}\omega_n + \Omega_d - \lambda^2 G_\gamma(\mathrm{i}\omega_n) \end{pmatrix}. \tag{7.31}$$

The analytic continuation to the real frequencies $\mathrm{i}\omega_n \to \omega + \mathrm{i}\delta$ with $\delta = 0^+$ gives the retarded Green's function in the particle-hole basis:

$$\mathcal{G}^R(\omega) = \frac{1}{(\omega + \mathrm{i}\delta)\left(\omega + \mathrm{i}\delta - 2\lambda^2 G^R_\gamma(\omega)\right) - \Omega_d^2} \cdot \begin{pmatrix} \omega + \mathrm{i}\delta + \Omega_d - \lambda^2 G^R_\gamma(\omega) & -\lambda^2 G^R_\gamma(\omega) \\ -\lambda^2 G^R_\gamma(\omega) & \omega + \mathrm{i}\delta - \Omega_d - \lambda^2 G^R_\gamma(\omega) \end{pmatrix}, \quad (7.32)$$

where $G^R_\gamma(\omega) = -\mathrm{i}\pi^{1/4} \mathrm{e}^{\mathrm{i}\pi \mathrm{sgn}(\omega)/4} \left(J|\omega|\right)^{-1/2}$.

Chapter 8

First-order dipolar phase transition in the Dicke model with infinitely coordinated frustrating interaction

8.1 Introduction

Realization of the equilibrium photonic condensates is of great interest for the fundamental study of a new states of light strongly coupled to quantum metamaterials [159–164]. In particular, cavity quantum electrodynamics of superconducting qubits is crucial for the quantum computation perspectives [165–168]. In quantum optics, e.g. in the cavity QED described by the famous Dicke model [169], the 'no-go' theorems made those perspectives gloomy [170–172], and only dynamically driven condensates are considered [173–178]. Nevertheless, it was found that in the equilibrium circuit QED systems the 'no-go' theorems may not hold [162, 163]. In

The contents of this chapter have been published and reprinted with permission from S. I. Mukhin and N. V. Gnezdilov, Phys. Rev. A **97**, 053809 (2018).

particular, an array of capacitively coupled Cooper pair boxes to a resonant cavity was proven to disobey the 'no-go' theorem for an equilibrium superradiant quantum phase transition [163]. Nevertheless, another complication was found in this case, i.e. it was demonstrated [164, 179, 180], that allowance for the gauge invariance with respect to the electromagnetic vector potential of the photon field causes Hamiltonian of the system to map on the extended Dicke model Hamiltonian of (pseudo)spins one-half, adding to the standard Dicke model a frustrating infinitely coordinated antiferromagnetic interaction between the spins. Lately, a numerical diagonalization results for small clusters with N spins were reported [164] to behaved differently depending on the parity of the number of spins N.

Motivated by the above history of the extended Dicke model exploration, we present in this paper analytic description of the superradiant equilibrium quantum phase transition in the an array of $N \gg 1$ Cooper pair boxes strongly coupled to a resonant cavity. The plan of the present paper is as follows.

First, we reproduce derivation [164, 179] of the extended Dicke Hamiltonian with infinitely coordinated antiferromagnetic (frustrating) term. Next, we confirm the absence of the zero modes in the spectrum of the bosonic excitations, as was found in [164]. Then, we introduce a new representation for the operators of Cartesian components of the total spin ('superspin') of N spins 1/2: a self-consistently rotating Holstein-Primakoff (RHP) representation. After that, we demonstrate that RHP method applied to extended Dicke Hamiltonian reveals the first order quantum phase transition, that sets the system into a double degenerate dipolar ordered superradiant state with coherent photonic condensate emerging in the cavity. Besides, in Appendix 8.7 we show that the RHP approach also reproduces the second order quantum phase transition for the Dicke Hamiltonian without frustrating interaction term, found earlier by other method [181, 182]. We discuss a drastic difference between the critical values of the coupling strength g_c in the $N \to \infty$ limit for the 1st and 2nd order phase transitions. In the Summary we present some evaluations of the parameters of a possible experimental setup for a validation of our theoretical predictions for Cooper pair box arrays in a microwave cavity.

8.2 Dicke Hamiltonian for a Cooper pair boxes array

In this section we present a derivation of the extended Dicke model Hamiltonian. We consider a single mode electromagnetic resonant cavity of a linear dimension L coupled to the array of N independent dissipationless Josephson junctions. It is assumed that the wavelength λ of the cavity's resonant photon is much greater than the inter-junction distance: $\lambda \gg L/N$. The vector potential of the electromagnetic field related with the photon is expressed in the second quantized form:

$$\vec{A} = \sqrt{\frac{c^2 h}{\omega V}} \left(\hat{a}^\dagger + \hat{a}\right) \vec{\epsilon}, \tag{8.1}$$

where h - is Planck's constant, ω is bare photon frequency, the photon creation and annihilation bosonic operators are $\hat{a}^\dagger$, $\hat{a}$, $\vec{\epsilon}$ is polarization of the electric field, c is velocity of light, and V is the volume of the cavity.

The Hamiltonian of the Cooper pair box array in the cavity then reads:

$$\hat{H} = \hat{H}_{ph} + \hat{H}_{JJ}\,, \tag{8.2}$$

$$\hat{H}_{ph} = \frac{1}{2}\left(\hat{p}^2 + \omega^2 \hat{q}^2\right)\,, \tag{8.3}$$

$$\hat{H}_{JJ} = E_C \sum_{i=1}^{N} \hat{n}_i^2 - E_J \sum_{i=1}^{N} \cos\left(\hat{\phi}_i - \frac{g}{\hbar}\hat{q}\right)\,, \tag{8.4}$$

where the coupling constant is $g = 2el\sqrt{4\pi}/\sqrt{V}$, and l is of the order of a penetration depth of an electric field into the superconducting islands forming the Josephson junction, thus, giving the effective thickness across of it [180]. For simplicity, we consider all the junctions being identical, with electric field polarization $\vec{\epsilon}$ aligned across a Josephson junction. Here the two mutually commuting sets of the conjugate variables are introduced: $[\hat{p}, \hat{q}] = -\mathrm{i}\hbar$ and $\left[\hat{n}_i, \hat{\phi}_i\right] = -\mathrm{i}$. The second quantized (harmonic oscillator) variables of the photonic field are:

$$\hat{p} = \mathrm{i}\sqrt{\frac{\hbar\omega}{2}}\left(\hat{a}^\dagger - \hat{a}\right) \quad \text{and} \quad \hat{q} = \sqrt{\frac{\hbar}{2\omega}}\left(\hat{a}^\dagger + \hat{a}\right)\,, \tag{8.5}$$

where $\left[\hat{a}, \hat{a}^\dagger\right] = 1$. An operator $2e\hat{n}_i = 2e\left(\hat{n}_i^R - \hat{n}_i^L\right)/2$ stands for half of a charge difference at the i-th junction, and equals half the difference

of the number of Cooper pairs populating the left and right islands of a Josephson junction accordingly, multiplied by the elementary charge $2e$ of the Cooper pair. The quantum of the charging energy of a single junction is $E_C = (2e)^2/2C$.

Following [179] we make a canonical transformation:

$$\hat{\phi}_i' = \hat{\phi}_i - \frac{g}{\hbar}\hat{q} \quad \text{and} \quad \hat{n}_i' = \hat{n}_i \tag{8.6}$$

for the JJ's variables and

$$\hat{p}' = \hat{p} + g\sum_{i=1}^{N}\hat{n}_i \quad \text{and} \quad \hat{q}' = \hat{q} \tag{8.7}$$

for photonic variables, so that $\left[\hat{p}', \hat{\phi}_i'\right] = 0$ and the other commutation relations between all the operators remain intact. The Hamiltonian (8.2) becomes

$$\begin{aligned}\hat{H} =& \frac{1}{2}\left(\hat{p}^2 + \omega^2\hat{q}^2\right) - g\hat{p}\sum_{i=1}^{N}\hat{n}_i + \frac{g^2}{2}\left(\sum_{i=1}^{N}\hat{n}_i\right)^2 + \\ &+ \sum_{i=1}^{N}\left(E_C\,\hat{n}_i^2 - E_J\cos\hat{\phi}_i\right),\end{aligned} \tag{8.8}$$

where the primes in the new variables are omitted for brevity. Thus, the infinitely coordinated interaction term $\propto g^2$ has appeared in (8.8) after the canonical transformation of the Hamiltonian (8.2).

We restrict ourselves to the Cooper pair box limit [183], when the charging energy E_C is large in comparison with Josephson coupling E_J and the eigenstates of the Hamiltonian (8.4) in the zero order approximation can be chosen as the eigenstates of the charge difference operators $\hat{n}_i$. The lowest bare energy level corresponding to the quantum states $\left|n_i = -\frac{1}{2}\right\rangle$ and $\left|n_i = \frac{1}{2}\right\rangle$ is thus twofold degenerate with respect to the direction of the Cooper pair box dipole moment $\vec{d}_i = 2el\hat{n}_i\vec{\epsilon}$ (l - is effective thickness of the i-th JJ). This double-degenerate level is separated from the levels with the greater charge differences by the E_C gap. The Josephson tunneling term $\sim E_J$ lifts the degeneracy and opens a gap between the energy levels of the two states that differ by the wave-function parity ± 1 with respect to inversion of the Cooper pair box dipole's direction. Thus, formed two-level system is naturally described by the Pauli matrices $\hat{\sigma}_i^{\alpha}$. On the subset of

these lowest energy states the initial Hamiltonian (8.4) of the Cooper pair box array of N Josephson junctions is represented by a Hamiltonian of interacting N spins half:

$$\hat{H}_{JJ} = \sum_{i=1}^{N} \left(E_C \, \hat{n}_i^2 - E_J \cos \hat{\phi}_i \right) \approx \frac{E_C}{4} \sum_{i=1}^{N} \left(\left| \frac{1}{2} \right\rangle \left\langle \frac{1}{2} \right| + \left| -\frac{1}{2} \right\rangle \left\langle -\frac{1}{2} \right| \right)_i$$
$$- \frac{E_J}{2} \sum_{i=1}^{N} \left(\left| \frac{1}{2} \right\rangle \left\langle -\frac{1}{2} \right| + \left| -\frac{1}{2} \right\rangle \left\langle \frac{1}{2} \right| \right)_i = \frac{N E_C}{4} \hat{1} - \frac{E_J}{2} \sum_{i=1}^{N} \hat{\sigma}_i^x. \quad (8.9)$$

Here charge and phase difference operators $\hat{n}_i$ and $\cos \hat{\phi}_i$ are projected on $\hat{s}_i^z$ and $\hat{s}_i^x$ correspondingly, where $\hat{s}_i^\alpha = \frac{1}{2} \hat{\sigma}_i^\alpha$ are spin-1/2 operators expressed via the Pauli matrices. As a result, initial Hamiltonian (8.8) reduces to the following spin-boson Hamiltonian, *modulo* energy shift $NE_C/4$:

$$\hat{H} = \frac{1}{2} \left(\hat{p}^2 + \omega^2 \hat{q}^2 \right) - g \hat{p} \sum_{i=1}^{N} \hat{s}_i^z - E_J \sum_{i=1}^{N} \hat{s}_i^x + \frac{g^2}{2} \left(\sum_{i=1}^{N} \hat{s}_i^z \right)^2. \quad (8.10)$$

It is important to clarify here the meaning of the spin-boson interaction term in (8.10), that had emerged when canonical transformation (8.6, 8.7) of the initial gauge-invariant Hamiltonian (8.2) was performed :

$$-g \hat{p} \, \hat{s}_i^z = -\mathrm{i} \sqrt{\frac{\hbar \omega}{2V}} \left(\hat{a}^\dagger - \hat{a} \right) \; 2el\sqrt{4\pi} \hat{s}_i^z = -\hat{\vec{\mathcal{E}}} \, \hat{\vec{d}}_i \quad (8.11)$$

and represents the energy of the dipole in the electric field. The electric field operator in (8.11) is given by

$$\hat{\vec{\mathcal{E}}} = \mathrm{i} \sqrt{\frac{h\omega}{V}} \left(\hat{a}^\dagger - \hat{a} \right) \vec{\epsilon} \quad (8.12)$$

and the dipole moment of the single junction is

$$\hat{\vec{d}}_i = 2e \hat{s}_i^z l \vec{\epsilon}. \quad (8.13)$$

The total dipole moment is then

$$\hat{\vec{d}} = \sum_{i=1}^{N} \hat{\vec{d}}_i = 2e \, l \vec{\epsilon} \sum_{i=1}^{N} \hat{s}_i^z. \quad (8.14)$$

For convenience of the further calculations we perform a unitary transformation $U^\dagger \hat{H} U$, where $U = \frac{1}{\sqrt{2}} \begin{pmatrix} 1 & \mathrm{i} \\ 1 & -\mathrm{i} \end{pmatrix}$ that interchanges operators of the Cartesian components of spin half: $\hat{s}_i^z \to -\hat{s}_i^y$, $\hat{s}_i^y \to -\hat{s}_i^x$ and $\hat{s}_i^x \to \hat{s}_i^z$.

Hence, the final Cooper pair box Hamiltonian, that we are going to explore, becomes:

$$\hat{H} = \frac{1}{2}\left(\hat{p}^2 + \omega^2 \hat{q}^2\right) + g\hat{p}\,\hat{S}^y - E_J\,\hat{S}^z + \frac{g^2}{2}\left(\hat{S}^y\right)^2, \tag{8.15}$$

where we have introduced operators $\hat{S}^\alpha = \sum_i \hat{s}_i^\alpha$ of the total spin components. The total spin $\hat{S}^2$ is conserved, because it commutes with (8.15): $\left[\hat{S}^2, H\right] = 0$. Cooper pairs tunneling is represented by $-E_J\hat{S}^z$ term, $g\hat{p}\,\hat{S}^y$ is a dipole coupling strength between Cooper pair box and photonic field, and $(g^2/2)\left(\hat{S}^y\right)^2$ stands for the infinitely coordinated 'antiferromagnetic' frustrating term.

8.3 Diagonalization of the frustrated Dicke model

8.3.1 Tunneling regime

In this section, we consider the frustrated Dicke Hamiltonian (8.15) and first assume that at small coupling strength g the Josepson tunneling term $-E_J\hat{S}_z$ dominates at zero temperature. Then the superspin is in the large S sector and hence, one is allowed to use the Holstein-Primakoff transformation [184] (HP) in the form:

$$\hat{S}^z = S - \hat{b}^\dagger\hat{b}, \tag{8.16}$$

$$\hat{S}^y = \mathrm{i}\sqrt{\frac{S}{2}}\left(\hat{b}^\dagger\sqrt{1 - \frac{\hat{b}^\dagger\hat{b}}{2S}} - \sqrt{1 - \frac{\hat{b}^\dagger\hat{b}}{2S}}\,\hat{b}\right) \simeq \mathrm{i}\sqrt{\frac{S}{2}}\left(\hat{b}^\dagger - \hat{b}\right), \tag{8.17}$$

$$\hat{S}^x = \sqrt{\frac{S}{2}}\left(\hat{b}^\dagger\sqrt{1 - \frac{\hat{b}^\dagger\hat{b}}{2S}} + \sqrt{1 - \frac{\hat{b}^\dagger\hat{b}}{2S}}\,\hat{b}\right) \simeq \sqrt{\frac{S}{2}}\left(\hat{b}^\dagger + \hat{b}\right), \tag{8.18}$$

where $\left[\hat{b}, \hat{b}^\dagger\right] = 1$. The substitution of (8.16, 8.17) into (8.15) gives Hamiltonian of the two linearly coupled harmonic oscillators:

$$\begin{aligned}\hat{H} =& \omega\left(\hat{a}^\dagger\hat{a} + \frac{1}{2}\right) - E_J\left(S - \hat{b}^\dagger\hat{b}\right) \\ &- \frac{g\sqrt{S\omega}}{2}\left(\hat{a}^\dagger - \hat{a}\right)\left(\hat{b}^\dagger - \hat{b}\right) - \frac{g^2 S}{4}\left(\hat{b}^\dagger - \hat{b}\right)^2 .\end{aligned} \tag{8.19}$$

This model also arises in the case of ultrastrong light-matter coupling regime with polariton dots [185]. Here and in what follows we put $\hbar = 1$. With the help of the usual linear Bogoliubov's transformation of the creation/annihilation operators (see appendix 8.6) we obtain diagonalized Hamiltonian:

$$\hat{H} = -E_J\left(S + \frac{1}{2}\right) + \frac{1}{2}\left(\varepsilon_1 + \varepsilon_2\right) + \varepsilon_1\,\hat{c}_1^\dagger\hat{c}_1 + \varepsilon_2\,\hat{c}_2^\dagger\hat{c}_2 \tag{8.20}$$

with the excitations spectrum described by the new oscillator frequencies:

$$\begin{aligned}2\varepsilon_{1,2}^2 =& E_J\left(E_J + g^2 S\right) + \omega^2 \\ &\pm\sqrt{\left(E_J\left(E_J + g^2 S\right) - \omega^2\right)^2 + 4\omega^2 g^2 S E_J}\,,\end{aligned} \tag{8.21}$$

where the frequencies $\varepsilon_{1,2}$ have to be chosen positive to keep the hermiticity of the initial operators $\hat{p}$, $\hat{q}$, $\hat{S}_y$. In contrast with the Dicke model without frustration [181] both energy branches are real in the whole range of the coupling constants g, but with a caveat. Namely, the ground state energy equals:

$$E_0(S) = -E_J\left(S + \frac{1}{2}\right) + \frac{1}{2}\left(\varepsilon_1 + \varepsilon_2\right) . \tag{8.22}$$

This ground state is stable as long as the ground state energy $E_0(S)$ (8.22) has global minimum as a function of the superspin S at the end of the interval $[0,\, N/2]$. One can find value of the coupling strength $g = \tilde{g}$, at which the minimum becomes double degenerate via solving equation $E_0\left(S = N/2, g = \tilde{g}\right) = E_0\left(S = 0, g = \tilde{g}\right) = \omega/2$:

$$\tilde{g} \simeq \sqrt{2E_J N} + \left(E_J + \omega\right)\sqrt{\frac{2}{NE_J}}\,, \tag{8.23}$$

which can be easily derived from large g asymptotic expression of $E_0(S)$:

$$E_0 \simeq -E_J\left(S+\frac{1}{2}\right)+\frac{g}{2}\sqrt{E_J S}. \tag{8.24}$$

For $g > \tilde{g}$ the minimum of $E_0(S)$ migrates from $S = N/2$ to $S = 0$, see Figure 8.1. This 'jump' of the minimum obviously makes ground state $S = N/2$ unstable and leads to an inapplicability of the quasi-classical HP approximation. Thus, our large S ground state description (8.22) is justified for $g < \tilde{g}$.

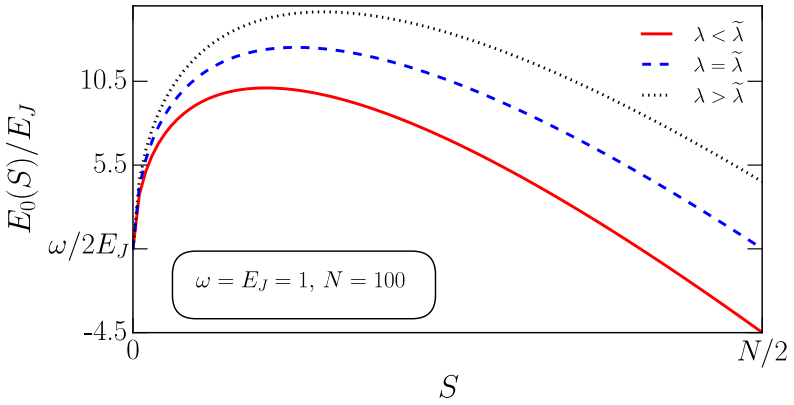

Figure 8.1. Ground state energy as a function of the superspin S at fixed dimensionless coupling constant $\lambda = g\sqrt{N/2E_J}$. The blue dashed line shows the double degenerate minimum of the ground state at the coupling strength $\lambda = \tilde{\lambda}$ (8.23).

8.3.2 Rotating Holstein-Primakoff representation

In order to make continuation of the theory into the stronger coupling strength region outside the interval $g < \tilde{g}$, we substitute in the Hamiltonian (8.15) the y, z components of the total spin operators with a generalised expression of the Holstein-Primakoff representation in a coordinate frame rotated by an angle θ in the z-y plane :

$$\begin{cases} \hat{S}^z = \hat{J}^z\cos\theta - \hat{J}^y\sin\theta \\ \hat{S}^y = \hat{J}^z\sin\theta + \hat{J}^y\cos\theta \end{cases} \tag{8.25}$$

Here the set of operators of the Cartesian projections of the total spin $\hat{J}^{x,y,z}$ are

$$\begin{cases} \hat{J}^z = S - \hat{b}^\dagger \hat{b} \\ \hat{J}^y \simeq \mathrm{i}\sqrt{\dfrac{S}{2}}\left(\hat{b}^\dagger - \hat{b}\right) \\ \hat{J}^x \simeq \sqrt{\frac{S}{2}}\left(\hat{b}^\dagger + \hat{b}\right) \end{cases} . \tag{8.26}$$

To find $\theta \neq 0$ solution that diagonalises (8.15) we introduce a shift, $i\sqrt{\alpha}$, of the photon creation/annihilation operators, similar to [181], in the following way:

$$\begin{cases} \hat{a}^\dagger = \hat{c}^\dagger - \mathrm{i}\sqrt{\alpha} \\ \hat{a} = \hat{c} + \mathrm{i}\sqrt{\alpha} \end{cases} , \tag{8.27}$$

thus, envisaging formation of a superradiant state. One substitutes (8.25 - 8.27) into (8.15) and the Hamiltonian, quadratic in operators $c, c^\dagger\, b,\, b^\dagger$, becomes:

$$\begin{aligned} \hat{H} =& \omega\left(\hat{c}^\dagger \hat{c} + \frac{1}{2}\right) - E_J \cos\theta \left(S - \hat{b}^\dagger \hat{b}\right) \\ & - \frac{g\cos\theta\sqrt{S\omega}}{2}\left(\hat{c}^\dagger - \hat{c}\right)\left(\hat{b}^\dagger - \hat{b}\right) - \frac{g^2\cos^2\theta\, S}{4}\left(\hat{b}^\dagger - \hat{b}\right)^2 , \end{aligned} \tag{8.28}$$

where an elimination of the linear in $\left(\hat{c}^\dagger - \hat{c}\right)$ and $\left(\hat{b}^\dagger - \hat{b}\right)$ terms in the Hamiltonian introduces a system of the two equations:

$$\sqrt{2\omega\alpha} + g\sin\theta\left(S - \left\langle \hat{b}^\dagger \hat{b}\right\rangle\right) = 0\,; \tag{8.29}$$

$$E_J \sin\theta + g\cos\theta\sqrt{2\omega\alpha} + g^2\cos\theta\sin\theta\left(S - \left\langle \hat{b}^\dagger \hat{b}\right\rangle - \frac{1}{2}\right) = 0\,. \tag{8.30}$$

We have also made in (8.28) a mean-field decoupling of the products that are higher than quadratic in $b,\, b^\dagger$-operators: $\hat{b}^\dagger\hat{b}\,\hat{b}^\dagger\hat{b} = 2\left\langle \hat{b}^\dagger\hat{b}\right\rangle \hat{b}^\dagger\hat{b} - \left\langle \hat{b}^\dagger\hat{b}\right\rangle^2$ and $\hat{b}^\dagger\hat{b}\left(\hat{b}^\dagger - \hat{b}\right) + \left(\hat{b}^\dagger - \hat{b}\right)\hat{b}^\dagger\hat{b} = \left(\hat{b}^\dagger - \hat{b}\right)\left(1 + 2\left\langle \hat{b}^\dagger\hat{b}\right\rangle\right)$.

A nontrivial solution $\alpha \neq 0$, $\theta \neq 0$ of the system of equations (8.29)

and (8.30) emerges when $g \geq \sqrt{2E_J}$:

$$\cos\theta = \frac{2E_J}{g^2}\,, \tag{8.31}$$

$$\sqrt{\alpha} = -\frac{gS}{\sqrt{2\omega}}\left(1 - \frac{\left\langle \hat{b}^\dagger \hat{b} \right\rangle}{S}\right)\sin\theta \simeq -\frac{gS}{\sqrt{2\omega}}\sin\theta = \\ = \mp\frac{gS}{\sqrt{2\omega}}\sqrt{1 - \frac{4E_J^2}{g^4}}. \tag{8.32}$$

Under the solutions (8.31), (8.32), the energy of the photonic condensate $= \omega\alpha$ exactly cancels with the sum of the rest of the c-number terms in the Hamiltonian (8.28):

$$\omega\alpha + gS\sin\theta\sqrt{2\omega\alpha} + \frac{g^2\sin^2\theta}{2}\left(S^2 - \left\langle \hat{b}^\dagger \hat{b} \right\rangle^2\right) = \\ = \frac{g^2\sin^2\theta}{2}\Big(S^2 - 2S\left\langle \hat{b}^\dagger \hat{b} \right\rangle + \left\langle \hat{b}^\dagger \hat{b} \right\rangle^2 - 2S^2 \\ + 2S\left\langle \hat{b}^\dagger \hat{b} \right\rangle + S^2 - \left\langle \hat{b}^\dagger \hat{b} \right\rangle^2\Big) = 0\,. \tag{8.33}$$

The c-number terms in the first line of (8.33) have the following meaning: the photonic condensate energy $\sim \omega\alpha$, the (negative) contribution of the dipole-photon coupling energy $\sim g\langle\hat{p}\rangle\langle\hat{S}^y\rangle$, and the zero-point oscillations energy of the frustration term $\sim g^2\langle(\hat{S}^y)^2\rangle/2$. The total of these three terms proves to be zero. This α-independent cancellation, actually, stems from the degeneracy of the energy minima of the diagonal in spin operators part of the extended Dicke Hamiltonian (8.15) with respect to $2S+1$ different $\hat{S}^y$ projections and classical part $\sim \sqrt{\alpha}$ of the photonic operator $\hat{p}$.

8.3.3 Superradiant dipolar regime

The structure of (8.28) is the same as (8.19), though with coefficients renormalised with prefactor $\cos\theta$ due to RHP rotation by an angle θ . Hence, after the Bogoliubov's transformation similar to the one already described in the Appendix 8.6, the diagonalized Hamiltonian expressed via new second quantized operators $\hat{e}_{1,2}^\dagger$, $\hat{e}_{1,2}$ acquires the form:

$$\hat{H} = -\frac{g^2\cos^2\theta}{2}\left(S + \frac{1}{2}\right) + \frac{1}{2}\left(\tilde{\varepsilon}_1 + \tilde{\varepsilon}_2\right) + \tilde{\varepsilon}_1\,\hat{e}_1^\dagger\hat{e}_1 + \tilde{\varepsilon}_2\,\hat{e}_2^\dagger\hat{e}_2 \tag{8.34}$$

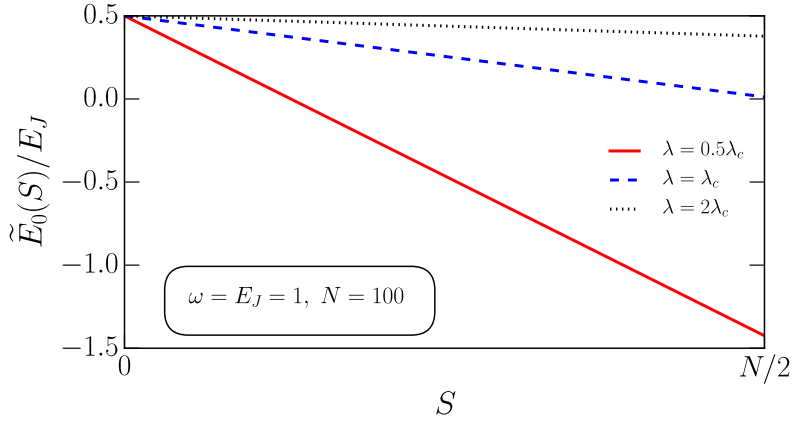

Figure 8.2. Ground state energy $\widetilde{E}_0$ as a function of the superspin S at fixed dimensionless coupling constant $\lambda = g\sqrt{N/2E_J}$.

with the positive eigenvalues $\tilde{\varepsilon}_{1,2}$

$$2\tilde{\varepsilon}_{1,2}^2 = \frac{g^4\cos^4\theta}{2}\left(S+\frac{1}{2}\right)+\omega^2 \pm\sqrt{\left(\frac{g^4\cos^4\theta}{2}\left(S+\frac{1}{2}\right)-\omega^2\right)^2+2S\,\omega^2 g^4\cos^4\theta} \tag{8.35}$$

and the ground state energy

$$\widetilde{E}_0(S) = -\frac{g^2\cos^2\theta}{2}\left(S+\frac{1}{2}\right)+\frac{1}{2}\left(\tilde{\varepsilon}_1+\tilde{\varepsilon}_2\right). \tag{8.36}$$

The stability of the large S state in this regime is provided by the negative slope of $\widetilde{E}_0(S)$ as a function of S (see Figure 8.2) in the strong coupling limit:

$$\widetilde{E}_0(S)\Big|_{g\to+\infty} \simeq \frac{\omega}{2}-\frac{2E_J^2}{g^2}\left(S+\frac{1}{2}\right). \tag{8.37}$$

The interval $g \geq \sqrt{2E_J}$ is characterized with an emergent dipole moment in the Cooper pair box array and the superradint photoinic condensate either as a metastable state for $\sqrt{2E_J} \leq g < g_c$, or as the ground state for $g \geq g_c$ (the critical strength g_c is found below). To see this explicitly, we

express electromagnetic field operators via the new set of Bose-operators found after the Bogoliubov's transformation:

$$\hat{p} = \sqrt{2\omega\alpha} + \mathrm{i}\frac{\omega\cos\delta}{\sqrt{2\tilde{\varepsilon}_1}}\left(\hat{e}_1^\dagger - \hat{e}_1\right) + \mathrm{i}\frac{\omega\sin\delta}{\sqrt{2\tilde{\varepsilon}_2}}\left(\hat{e}_2^\dagger - \hat{e}_2\right), \tag{8.38}$$

$$\hat{q} = \frac{\cos\delta}{\sqrt{2\tilde{\varepsilon}_1}}\left(\hat{e}_1^\dagger + \hat{e}_1\right) + \frac{\sin\delta}{\sqrt{2\tilde{\varepsilon}_2}}\left(\hat{e}_2^\dagger + \hat{e}_2\right). \tag{8.39}$$

In turn, the spin operators are expressed via $\hat{e}_i$, $\hat{e}_i^\dagger$, $i = 1, 2$ as well:

$$\hat{J}_z = S\left(1 - \frac{\left\langle \hat{b}^\dagger\hat{b}\right\rangle}{S}\right) \simeq S, \tag{8.40}$$

$$\hat{J}_y = -\mathrm{i}\frac{E_J\sqrt{S}\sin\delta}{g\sqrt{\tilde{\varepsilon}_1}}\left(\hat{e}_1^\dagger - \hat{e}_1\right) + \mathrm{i}\frac{E_J\sqrt{S}\cos\delta}{g\sqrt{\tilde{\varepsilon}_2}}\left(\hat{e}_2^\dagger - \hat{e}_2\right), \tag{8.41}$$

$$\hat{J}_x = -\frac{E_J\sqrt{S}\sin\delta}{g\sqrt{\tilde{\varepsilon}_1}}\left(\hat{e}_1^\dagger + \hat{e}_1\right) + \frac{E_J\sqrt{S}\cos\delta}{g\sqrt{\tilde{\varepsilon}_2}}\left(\hat{e}_2^\dagger + \hat{e}_2\right). \tag{8.42}$$

The Bogoliubov's 'angle' δ can be found from the consistency relation:

$$\tan 2\delta = \frac{2\sqrt{2S}\,\omega\, g^2\cos^2\theta}{g^4\cos^4\theta\left(S + \frac{1}{2}\right) - 2\omega^2}. \tag{8.43}$$

We find for $g \geq \sqrt{2E_J}$ the following non-zero expectation values in the ground state of Hamiltonian (8.34). For the electric field $\hat{\vec{\mathcal{E}}}$:

$$\left\langle \hat{\vec{\mathcal{E}}}\cdot\vec{\epsilon}\right\rangle\sqrt{\frac{V}{4\pi}} = \langle\hat{p}\rangle = \sqrt{2\omega\alpha} \simeq -gS\sin\theta = \\ = \mp gS\sqrt{1 - \frac{4E_J^2}{g^4}}; \tag{8.44}$$

for the modulus of the Josephson tunneling energy of the Cooper pairs (it decreases):

$$-E_J\langle\hat{S}^z\rangle = -E_J\langle\hat{J}^z\rangle\cos\theta \simeq -S\,\frac{2E_J^2}{g^2}; \tag{8.45}$$

and a for the emergent finite mean value of the dipole moment:

$$\langle\hat{d}\rangle = 2el\langle\hat{S}^y\rangle = 2el\langle\hat{J}^z\rangle\sin\theta \simeq \pm 2elS\sqrt{1 - \frac{4E_J^2}{g^4}}. \tag{8.46}$$

Hence, results (8.44) and (8.46) indicate that upon an increase of the coupling strength $g > \sqrt{2E_J}$ there is a state with the energy given in (8.36), which is characterized by an emergent superradiant electromagnetic field $\langle \hat{p} \rangle \neq 0$ in the cavity together with a finite dipole moment of the Cooper pair boxes: $\langle \hat{d} \rangle \neq 0$. The latter means that rotation angle θ introduced in (8.25) regulates an extent of a Cooper pair wave function between the superconducting islands forming each Josephson junction in the Josephson junction array, see Figure 8.3. Namely, when θ progressively deviates from zero, the Cooper pairs become localized in one of the two superconducting islands constituting a given Josephson junction, and as a result, the latter acquires a dipole moment.

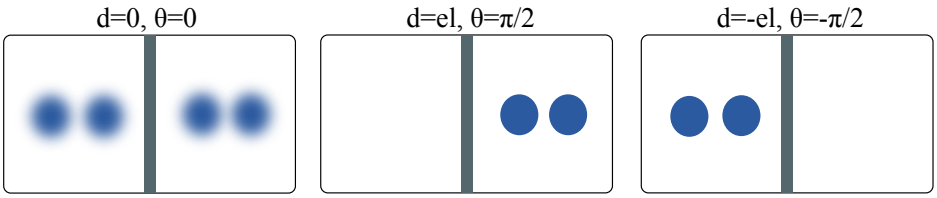

Figure 8.3. Schematic layout of the amplitude distributions of the Cooper pair's wave function in the adjacent islands of a single JJ and corresponding dipole moment values depending on the rotation angle θ, see text and equations (8.25).

8.4 First order dipolar phase transition

In this section we calculate a critical coupling g_c, at which a first order phase transition between the tunneling and dipolar states described in Sections 8.3.1 and 8.3.3 takes place.

In Figure 8.4 we plotted ground state energies calculated for tunneling and dipolar states as functions of coupling g: $E_0(S)$ and $\widetilde{E}_0(S)$, see (8.22) and (8.36) correspondingly. A dimensionless coupling constant $\lambda = g\sqrt{N/2E_J}$ is used. In the strong coupling limit, $g \gg \sqrt{2E_J}$, the g dependence of the both branches of energy is very well approximated by (8.24) and (8.37).

Hence, in the thermodynamic limit $N \to \infty$, solution of $E_0 = \widetilde{E}_0$ gives

the critical value g_c of the coupling constant:

$$g_c \simeq \sqrt{2E_J N} + \omega\sqrt{\frac{2}{NE_J}}\,. \tag{8.47}$$

Here a crucial difference with respect to [181] is that the critical point corresponds to $\lambda_c \approx N$ and not 1 as in the standard Dicke model without frustration. Hence, transition now is size-dependent, where the 'size' of the system is the total number N of Cooper pair box's inside the microwave cavity.

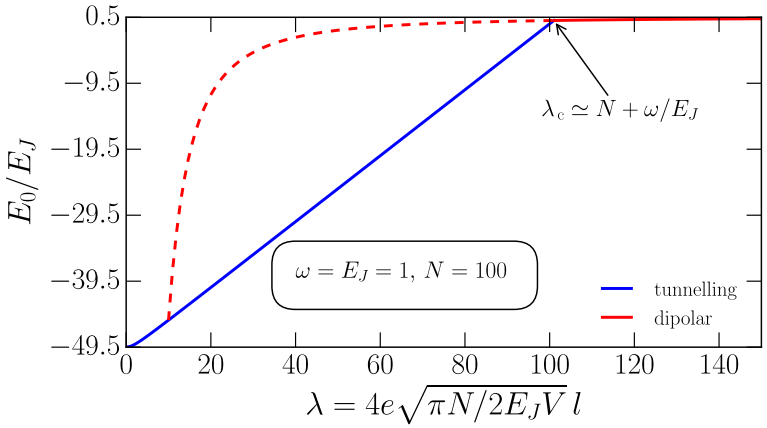

Figure 8.4. Ground state energy as a function of dimensionless coupling constant $\lambda = g\sqrt{N/2E_J}$. Blue line is for the Josephson tunneling state in the interval $\lambda < \lambda_c \approx N$. Red line is for dipolar ordered state. Red dashed line shows the dipolar state in the metastable region preceding the first order phase transition at λ_c.

At $\lambda = \sqrt{N}$, i.e. $g = \sqrt{2E_J}$, the ground state becomes degenerate and a dipolar branch $\widetilde{E}_0(S)$ first appears. For $\sqrt{N} < \lambda < N$, i.e. $\sqrt{2E_J} < g < g_c$, the dipolar state minimal energy $\widetilde{E}_0(S)$ is higher then the tunneling ground state energy $E_0(S)$. Hence, the system remains in the tunneling state (i.e. dipolar disordered). At $\lambda = \lambda_c$ the ground state energy $E_0(S)$ crosses the dipole state energy branch $\widetilde{E}_0(S)$ for the second time and goes above $\widetilde{E}_0(S)$. At the critical coupling $g = g_c$ (i.e. $\lambda = \lambda_c$) the first order phase transition from the tunneling state to dipolar ordered state takes place. It is, indeed, a first order transition, since at $g = g_c$ dipole moment in the dipolar state is already finite: $\langle \hat{d} \rangle \approx \pm 2elS$, see (8.46), while in

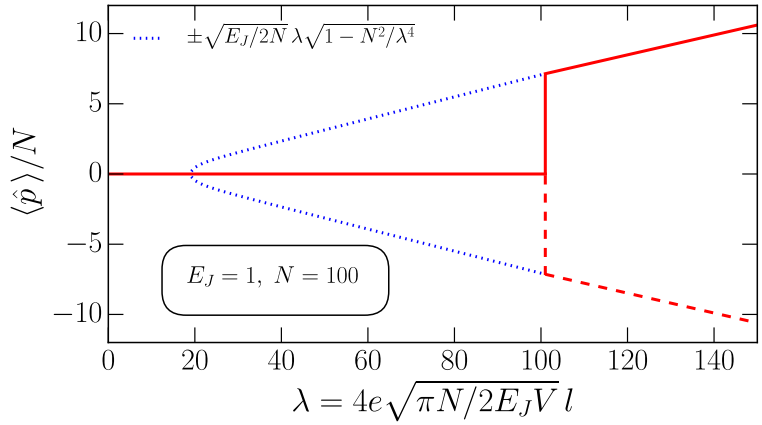

Figure 8.5. Photon field $\langle\hat{p}\rangle$ emerging in the cavity as a function of dimensionless coupling constant $\lambda = g\sqrt{N/2E_J}$. The first order transition to the state with the macroscopic photon occupation number $\langle\hat{a}^\dagger\hat{a}\rangle \neq 0$ occurs at the critical coupling $\lambda_c \simeq N + \omega/E_J$. The blue dotted line shows the metastable solution for $\langle\hat{p}\rangle$, that appears at $\lambda = \sqrt{N}$.

the tunneling state it equals zero. Namely, the first order phase transition results in

$$\langle\hat{p}\rangle = -Sg\sin\theta = \begin{cases} 0\,, & g < g_c \\ \mp Sg\sqrt{1-4E_J^2/g^4}, & g \geq g_c \end{cases} \tag{8.48}$$

see Figure 8.5, and

$$-E_J\left\langle\hat{S}^z\right\rangle = -SE_J\cos\theta = \begin{cases} -SE_J, & g < g_c \\ -E_J^2 2S/g^2, & g \geq g_c \end{cases}\,, \tag{8.49}$$

$$\left\langle\hat{d}\right\rangle = 2elS\sin\theta = \begin{cases} 0\,, & g < g_c \\ \pm 2elS\sqrt{1-4E_J^2/g^4}, & g \geq g_c \end{cases}\,. \tag{8.50}$$

The collective dipole moment (8.50) is defined by the angle θ, which is shown in the Figure 8.6.

It is important to mention here, that, comparison of (8.47) with (8.23) gives: $\tilde{g} - g_c = \sqrt{2E_J/N} > 0$. Hence, we have found the first order phase transition in the region of validity (i.e. $g < \tilde{g}$) of the large superspin limit $S = N/2 \gg 1$, that justifies the use of the HP approach. In the limit $g \to$

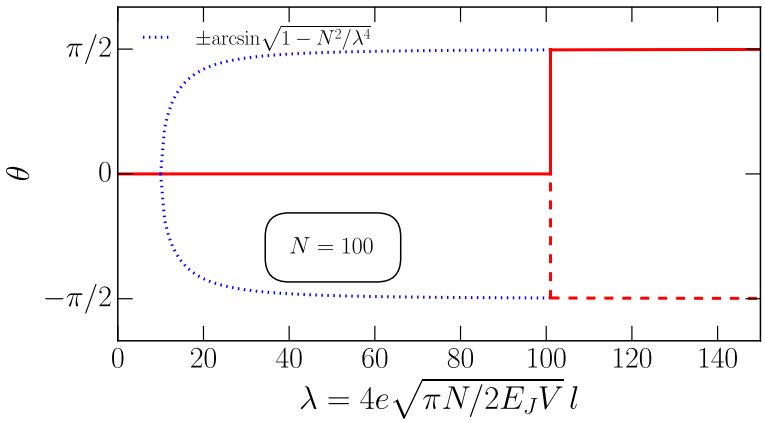

Figure 8.6. The angle θ, that characterizes rotation of HP, as a function of dimensionless coupling constant $\lambda = g\sqrt{N/2E_J}$. The colour scheme is chosen the same as for the Figure 8.5.

$+\infty$ the dipolar ordered ground state energy $\widetilde{E}_0$ approaches from below the ground state energy of a free resonant photon, $\omega/2$. Simultaneously, at $g = g_c$ the ground state energy: $\widetilde{E}_0(S) = 0 < \omega/2$. Hence, our semiclassical description indicates that after the dipole transition the system gradually approaches decoupled state $\widetilde{E}_0(S) = \omega/2$, but with saturated value of the collective dipole moment $\propto \langle \hat{S}^y \rangle \to N/2$. It is not possible to decide in the framework of our semiclassical approach whether a crossover to a state $\langle \hat{S}^y \rangle = 0$ happens in the $g \to +\infty$ limit. The latter state was predicted numerically in finite, even N spin-1/2 cluster realization of the extended Dicke model [164].

The excitations branches (8.35) of the diagonalized Hamiltonian are shown on the Figures 8.7, 8.8.
The branch ε_1, that grows with the increase of the coupling, goes to the initial photon's frequency ω after the first order transition. ε_2 approaches zero in the strong coupling limit.

Combining together (8.47) and expression $g = 2el\sqrt{4\pi}/(\sqrt{V})$, one may formulate the condition for the dipolar quantum phase transition as:

$$4el\sqrt{\pi/V} = \sqrt{2NE_J}\,, \tag{8.51}$$

where l is a penetration depth of electric field into Cooper pair box superconducting island and V is volume of the microwave cavity. Taking into

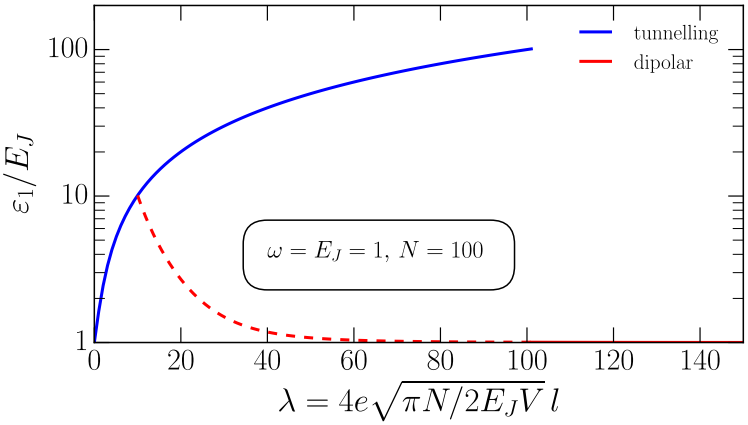

Figure 8.7. Excitation branches ε_1, $\tilde{\varepsilon}_1$ (8.21, 8.35) as the functions of dimensionless coupling constant $\lambda = g\sqrt{N/2E_J}$. The vertical axis is shown in the logarithmic scale. At the critical coupling $\lambda_c \approx N$ the frequency ε_1 jumps to $\tilde{\varepsilon}_1 \approx \omega$. The color scheme is the same as in Figure 8.4.

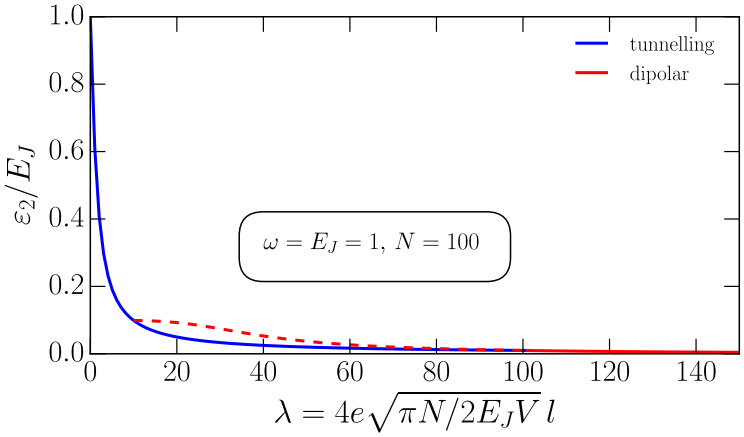

Figure 8.8. Excitation branches ε_2, $\tilde{\varepsilon}_2$ (8.21, 8.35) as a function of dimensionless coupling constant $\lambda = g\sqrt{N/2E_J}$. The frequencies ε_2, $\tilde{\varepsilon}_2$ asymptotically approach zero in the strong coupling limit. The color scheme is the same as in Figure 8.4.

account, that charging energy $E_C = (2e)^2/2C$ is of order: $E_C = 2e^2/l$,

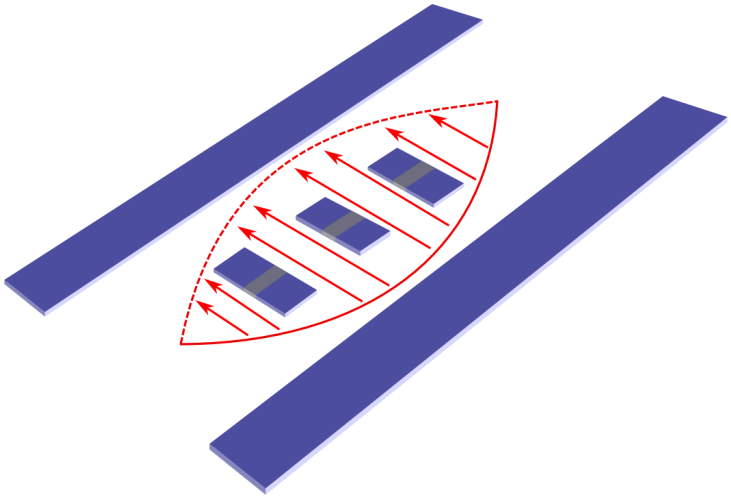

Figure 8.9. Schematic layout of a Cooper pair box array inside a microwave resonator of coplanar geometry with one-dimensional superconducting transmission line (stripline resonator), similar to proposed in [165] for achieving of a strong coupling g of two-level systems to the resonant photon in our frustrated Dicke Hamiltonian model.

one may rewrite (8.51) in the following form:

$$L \approx l \frac{E_C l^2}{E_J N \Sigma} \ , \tag{8.52}$$

where Σ and L are wave-guide (microwave cavity) cross-section area and length respectively. Assuming $L \approx Nl$ we finally find the following condition:

$$N^2 \approx \frac{E_C l^2}{E_J \Sigma} \ . \tag{8.53}$$

Hence, we come to a similar conclusion (see Figure 8.9) as was already made in [165], that in order to achieve strong coupling limit $g \geq g_{\rm c}$ for a Cooper pair box array of a 'thermodynamic size' $N \approx 10^2$ inside a microwave resonator, a coplanar geometry with one-dimensional superconducting transmission line (stripline resonator) should be used, thus providing inequality $S/l^2 \ll 1$, and Cooper pair box should have charging energy much greater than Josephson coupling energy: $E_C \gg E_J$.

8.5 Conclusions

In summary, we have demonstrated that strong enough capacitive coupling of the Cooper pair box array of low-capacitance Josephson junctions to a microwave resonant photon may lead to a first order quantum phase transition. As a result, a dipolar ordered state of Cooper pairs is formed, coupled to emerged coherent photonic condensate. The phase transition is of the first order due to infinitely coordinated antiferromagnetic (frustrating) interaction, that arises between Cooper pair dipoles of different Cooper pair boxes. This frustrating interaction is induced by the gauge-invariant coupling of the Josephson junctions to the resonant photon vector-potential in the microwave cavity. The strength of the coherent electromagnetic radiation field that emerges under the phase transition is proportional to the number N of the Cooper pair boxes in the array and is reminiscent of the superradiant state of Dicke model without frustrating term found previously [181]. Nevertheless, the phase transition into the latter state is of second order [181] (see also Figure 8.10 in the Appendix 8.7).

The analytical description of the first order quantum phase transition in the Dicke model with infinitely coordinated antiferromagnetic frustrating interaction has become possible due to a new analytic tool: self-consistently 'rotating' Holstein-Primakoff representation for the Cartesian components of the total spin, which is described in this paper. Our approach enables, as a by-product, description of the second order quantum phase transition in the Dicke model without frustrating antiferromagnetic interaction, explored previously by other authors [181]. Nevertheless, 'rotating' Holstein-Primakoff representation remains to be semiclassical ($S \to \infty$). Therefore, the region of 'spin liquid' with $S \sim 1$ is not attainable within this method.

8.6 Appendix: Bogoliubov's transformation for the frustrated Hamiltonian

Below we show in detail a diagonalization procedure of the Hamiltonian (8.19). Let's introduce

$$\hat{p}_x = \mathrm{i}\frac{1}{\sqrt{2\omega}}\left(\hat{a}^\dagger - \hat{a}\right) \quad \text{and} \quad \hat{x} = \sqrt{\frac{\omega}{2}}\left(\hat{a}^\dagger + \hat{a}\right) \tag{8.54}$$

together with

$$\hat{p}_y = \mathrm{i}\frac{1}{\sqrt{2E_J}}\left(\hat{b}^\dagger - \hat{b}\right) \quad \text{and} \quad \hat{y} = \sqrt{\frac{E_J}{2}}\left(\hat{b}^\dagger + \hat{b}\right) \tag{8.55}$$

and rewrite (8.19) in terms of (8.54, 8.55):

$$\begin{aligned}\hat{H} =& -E_J\left(S+\frac{1}{2}\right) + \frac{1}{2}\left(\hat{x}^2 + \omega^2\,\hat{p}_x^2\right) + \frac{1}{2}\left(\hat{y}^2 + E_J^2\,\hat{p}_y^2\right) \\ &+ \omega g\sqrt{SE_J}\,\hat{p}_x\hat{p}_y + \frac{g^2 S E_J}{2}\,\hat{p}_y^2 = \\ =& -E_J\left(S+\frac{1}{2}\right) + \frac{1}{2}\hat{K}_{xy} + \frac{1}{2}\hat{K}_{p_xp_y},\end{aligned} \tag{8.56}$$

where

$$\hat{K}_{xy} = \hat{x}^2 + \hat{y}^2\,, \tag{8.57}$$

$$\hat{K}_{p_xp_y} = \omega^2\hat{p}_x^2 + E_J\left(E_J + g^2 S\right)\hat{p}_y^2 + 2\,\omega g\sqrt{SE_J}\hat{p}_x\hat{p}_y\,. \tag{8.58}$$

We diagonalize (8.56) by performing a linear transformation of the quantum operators:

$$\begin{pmatrix}\hat{p}_x\\ \hat{p}_y\end{pmatrix} = \begin{pmatrix}\cos\gamma & \sin\gamma\\ -\sin\gamma & \cos\gamma\end{pmatrix}\begin{pmatrix}\hat{p}_1\\ \hat{p}_2\end{pmatrix}, \quad \begin{pmatrix}\hat{x}\\ \hat{y}\end{pmatrix} = \begin{pmatrix}\cos\gamma & \sin\gamma\\ -\sin\gamma & \cos\gamma\end{pmatrix}\begin{pmatrix}\hat{q}_1\\ \hat{q}_2\end{pmatrix}. \tag{8.59}$$

Then

$$\hat{K}_{xy} = \hat{q}_1^2 + \hat{q}_2^2\,, \tag{8.60}$$

and

$$\begin{aligned}\hat{K}_{p_xp_y} =& \left(\omega^2\cos^2\gamma + E_J\left(E_J + g^2S\right)\sin^2\gamma - 2\omega g\sqrt{SE_J}\sin\gamma\cos\gamma\right)\hat{p}_1^2 \\ &+ \left(\omega^2\sin^2\gamma + E_J\left(E_J + g^2S\right)\cos^2\gamma + 2\omega g\sqrt{SE_J}\sin\gamma\cos\gamma\right)\hat{p}_2^2 \\ &+ \left(\left(\omega^2 - E_J\left(E_J + g^2S\right)\right)\sin 2\gamma + 2\omega g\sqrt{SE_J}\cos 2\gamma\right)\hat{p}_1\hat{p}_2.\end{aligned} \tag{8.61}$$

The diagonalization condition that eliminates the cross-term $\sim \hat{p}_1\hat{p}_2$, is:

$$\tan 2\gamma = \frac{2\omega g\sqrt{SE_J}}{E_J\left(E_J + g^2 S\right) - \omega^2}\,. \tag{8.62}$$

So, diagonalized operator $\hat{K}_{p_x p_y}$ becomes:

$$\hat{K}_{p_x p_y} = \varepsilon_1^2\,\hat{p}_1^2 + \varepsilon_2^2\,\hat{p}_2^2\,, \tag{8.63}$$

where:

$$\begin{aligned} 2\varepsilon_1^2 =& E_J\left(E_J + g^2 S\right) + \omega^2 - \left(E_J\left(E_J + g^2 S\right) - \omega^2\right)\cos 2\gamma \\ & - 2\omega g\sqrt{S E_J}\sin 2\gamma\,, \end{aligned} \tag{8.64}$$

$$\begin{aligned} 2\varepsilon_2^2 =& E_J\left(E_J + g^2 S\right) + \omega^2 + \left(E_J\left(E_J + g^2 S\right) - \omega^2\right)\cos 2\gamma \\ & + 2\omega g\sqrt{S E_J}\sin 2\gamma\,. \end{aligned} \tag{8.65}$$

Substitution of (8.62) to (8.64) and (8.65) gives the eigenvalues:

$$2\varepsilon_{1,2}^2 = E_J\Big(E_J + g^2 S\Big) + \omega^2 \pm \sqrt{\left(E_J(E_J + g^2 S) - \omega^2\right)^2 + 4\omega^2 g^2 S E_J}. \tag{8.66}$$

The transformation:

$$\hat{p}_{1,2} = \mathrm{i}\frac{1}{\sqrt{2\varepsilon_{1,2}}}\left(\hat{c}_{1,2}^\dagger - \hat{c}_{1,2}\right) \quad \text{and} \quad \hat{q}_{1,2} = \sqrt{\frac{\varepsilon_{1,2}}{2}}\left(\hat{c}_{1,2}^\dagger + \hat{c}_{1,2}\right) \tag{8.67}$$

finally gives the diagonal Hamiltonian (8.20).

8.7 Appendix: Quantum phase transition in the Dicke model

We consider the standard Dicke Hamiltonian [169, 181] (modulo our notations)

$$\hat{H} = \frac{1}{2}\left(\hat{p}^2 + \omega^2\hat{q}^2\right) + g\hat{p}\,\hat{S}^y - E_J\,\hat{S}^z \tag{8.68}$$

at small coupling g. We apply (8.16, 8.17) to 8.68:

$$\begin{aligned} \hat{H} =& -E_J\left(S + \frac{1}{2}\right) + \omega\left(\hat{a}^\dagger\hat{a} + \frac{1}{2}\right) + E_J\left(\hat{b}^\dagger\hat{b} + \frac{1}{2}\right) \\ & - \frac{g\sqrt{S\omega}}{2}\left(\hat{a}^\dagger - \hat{a}\right)\left(\hat{b}^\dagger - \hat{b}\right)\,. \end{aligned} \tag{8.69}$$

The Bogoliubov's transformation, similar to those in Appendix 8.6, gives:

$$\hat{H} = -E_J\left(S + \frac{1}{2}\right) + \varepsilon_1\left(\frac{1}{2} + \hat{c}_1^\dagger\hat{c}_1\right) + \varepsilon_2\left(\frac{1}{2} + \hat{c}_2^\dagger\hat{c}_2\right)\,, \tag{8.70}$$

with the excitations spectrum described by the new oscillator frequencies:

$$2\varepsilon_{1,2}^2 = E_J^2 + \omega^2 \pm \sqrt{\left(E_J^2 - \omega^2\right)^2 + 4\omega^2 g^2 S E_J}\,. \tag{8.71}$$

The ground state energy equals:

$$E_0(S) = -E_J\left(S + \frac{1}{2}\right) + \frac{1}{2}\left(\varepsilon_1 + \varepsilon_2\right) \tag{8.72}$$

One can check that as a function of S the energy $E_0(S)$ has minimum at $S = N/2$, i.e. at the end of the interval of all possible total spin values $0 \leq S \leq N/2$. This fact justifies the Holstein-Primakoff approach (8.16-8.18) valid in the large spin limit.

However, the lowest branch of excitations becomes imaginary when $g > g_{\mathrm{c}} = \sqrt{E_J/S}$:

$$\varepsilon_2 = \sqrt{\frac{E_J^2 + \omega^2}{2} - \frac{\sqrt{\left(E_J^2 - \omega^2\right)^2 + 4\omega^2 g^2 S E_J}}{2}} \tag{8.73}$$

Thus, the ground state described above is unstable in the interval $g > g_c$, compare [181].

The method described in Section 8.3.2 (8.25-8.27) transforms the Hamiltonian (8.69) into:

$$\begin{aligned}
\hat{H} =& \omega\left(\hat{c}^\dagger\hat{c} + \mathrm{i}\sqrt{\alpha}\left(\hat{c}^\dagger - \hat{c}\right) + \alpha + \frac{1}{2}\right) - E_J\cos\theta\left(S - \hat{b}^\dagger\hat{b}\right) \\
&+ E_J\sin\theta\,\mathrm{i}\sqrt{\frac{S}{2}}\left(\hat{b}^\dagger - \hat{b}\right) - \frac{g\cos\theta\sqrt{S\omega}}{2}\left(\hat{c}^\dagger - \hat{c}\right)\left(\hat{b}^\dagger - \hat{b}\right) \\
&+ g\cos\theta\sqrt{2\omega\alpha}\,\mathrm{i}\sqrt{\frac{S}{2}}\left(\hat{b}^\dagger - \hat{b}\right) \\
&+ g\sin\theta\,\mathrm{i}\sqrt{\frac{\omega}{2}}\left(\hat{c}^\dagger - \hat{c}\right)\left(S - \left\langle\hat{b}^\dagger\hat{b}\right\rangle\right) + g\sin\theta\sqrt{2\omega\alpha}\left(S - \hat{b}^\dagger\hat{b}\right).
\end{aligned} \tag{8.74}$$

Here we have decoupled cubic in $\hat{c}, \hat{b}$ operators terms in a mean-field approximation. Conditions for vanishing of the linear terms $\propto \left(\hat{c}^\dagger - \hat{c}\right)$ and $\left(\hat{b}^\dagger - \hat{b}\right)$ in the Hamiltonian (8.74) are:

$$\sqrt{2\omega\alpha} + g\sin\theta\,\left(S - \left\langle\hat{b}^\dagger\hat{b}\right\rangle\right) = 0 \tag{8.75}$$

$$E_J\sin\theta + g\cos\theta\sqrt{2\omega\alpha} = 0 \tag{8.76}$$

Solving the system of equations (8.75) and (8.76) we find:

$$\cos\theta = \frac{E_J}{Sg^2}\left(1 - \frac{\left\langle \hat{b}^\dagger \hat{b}\right\rangle}{S}\right)^{-1} \simeq \frac{E_J}{Sg^2} \equiv \frac{g_c^2}{g^2}\,, \tag{8.77}$$

$$\sqrt{\alpha} = -\frac{gS}{\sqrt{2\omega}}\left(1 - \frac{\left\langle \hat{b}^\dagger \hat{b}\right\rangle}{S}\right)\sin\theta \simeq \frac{gS}{\sqrt{2\omega}}\sqrt{1 - \frac{g_c^4}{g^4}}, \tag{8.78}$$

where both the shift $\sqrt{\alpha}$ and rotation angle θ are non-zero when $g > g_c$. Thus, using solutions (8.77) and (8.78) we obtain the initial Hamiltonian (8.74) in the form similar to (8.69), but renormalised with $\cos\theta$ coefficients:

$$\begin{aligned}\hat{H} =& \frac{E_J S}{2\cos\theta}\left(1 - \cos^2\theta\right) - \frac{E_J}{\cos\theta}\left(S + \frac{1}{2}\right) + \omega\left(\hat{c}^\dagger \hat{c} + \frac{1}{2}\right) \\ &+ \frac{E_J}{\cos\theta}\left(\hat{b}^\dagger \hat{b} + \frac{1}{2}\right) - \frac{g\cos\theta\sqrt{S\omega}}{2}\left(\hat{c}^\dagger - \hat{c}\right)\left(\hat{b}^\dagger - \hat{b}\right).\end{aligned} \tag{8.79}$$

Next, we perform Bogoliubov's transformation that diagonalizes (8.79), by performing a linear transform of Bose-operators $\hat{c}$, $\hat{b}$ into Bose-operators $\hat{e}_{1,2}$, and obtain:

$$\begin{aligned}\hat{H} =& \frac{E_J S}{2\cos\theta}\left(1 - \cos^2\theta\right) - \frac{E_J}{\cos\theta}\left(S + \frac{1}{2}\right) \\ &+ \tilde{\varepsilon}_1\left(\frac{1}{2} + \hat{e}_1^\dagger \hat{e}_1\right) + \tilde{\varepsilon}_2\left(\frac{1}{2} + \hat{e}_2^\dagger \hat{e}_2\right)\end{aligned} \tag{8.80}$$

with the eigenvalues:

$$2\tilde{\varepsilon}_{1,2}^2 = \frac{E_J^2}{\cos^2\theta} + \omega^2 \pm \sqrt{\left(\frac{E_J^2}{\cos^2\theta} - \omega^2\right)^2 + 4\omega^2 E_J^2}\,, \tag{8.81}$$

where both branches are now real for $g > g_c = \sqrt{E_J/S}$ due to renormalisation of the coefficients with $\cos\theta$ factors. We have expressed in (8.81) the coupling constant g via $\cos\theta$ using the self-consistency relation (8.77). As is obvious from (8.77) and (8.78), both the shift $\sqrt{\alpha}$ and rotation angle θ progressively deviate from zero with increasing coupling strength g in the interval $g > g_c$, thus, providing a description of the new stable phase of the system.

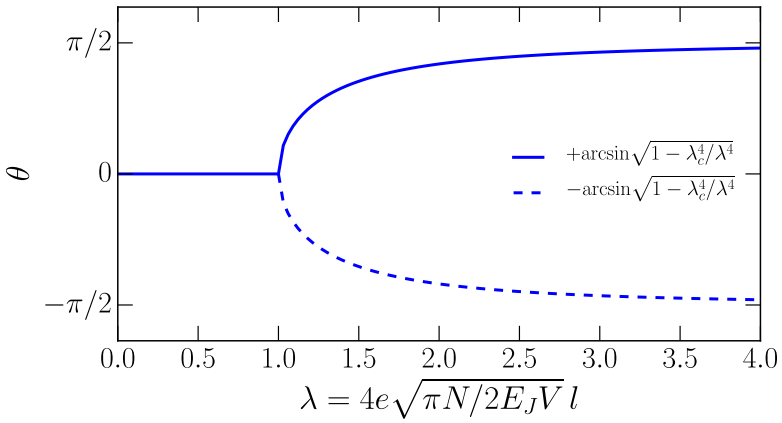

Figure 8.10. The angle θ as a function of dimensionless coupling constant $\lambda = g\sqrt{N/2E_J}$ in the Dicke model without frustration term.

The ground state energy of the system is now:

$$\widetilde{E}_0(S) = -\frac{E_J}{2\cos\theta}(S+1) - \frac{E_J S}{2}\cos\theta + \frac{1}{2}(\tilde{\varepsilon}_1 + \tilde{\varepsilon}_2)\ , \tag{8.82}$$

which always has a minimum at the end of the spin interval, at $S = N/2$, thus justifying the Holstein-Primakoff approximation at finite angles θ.

Thus, we found the second order phase transition that is manifested by a gradual rotation of the total spin expectation value in the $y-z$ plane by an angle θ:

$$\langle\hat{p}\rangle = -Sg\sin\theta = \begin{cases} 0, & g < g_c \\ \mp Sg\sqrt{1 - g_c^4/g^4}, & g \geq g_c \end{cases} \tag{8.83}$$

and

$$\left\langle\hat{d}\right\rangle = 2eSl\sin\theta = \begin{cases} 0\,, & g < g_c \\ \pm 2elS\sqrt{1 - g_c^4/g^4}, & g \geq g_c \end{cases} \tag{8.84}$$

where $g_c = \sqrt{2E_J/N}$ and $S = N/2$. The angle θ, that describes the transition is plotted in the Figure 8.10.

Bibliography

[1] E. Majorana. *Teoria simmetrica dell'elettrone e del positrone.* Il Nuovo Cimento (1924-1942) **14**, 171 (1937).

[2] P. A. M. Dirac and R. H. Fowler. *A theory of electrons and protons.* Proceedings of the Royal Society of London. Series A, Containing Papers of a Mathematical and Physical Character **126**, 360–365 (1930).

[3] G. E. Volovik. *Fermion zero modes on vortices in chiral superconductors.* Journal of Experimental and Theoretical Physics Letters **70**, 609–614 (1999).

[4] N. Read and D. Green. *Paired states of fermions in two dimensions with breaking of parity and time-reversal symmetries and the fractional quantum Hall effect.* Phys. Rev. B **61**, 10267–10297 (2000).

[5] D. A. Ivanov. *Non-Abelian Statistics of Half-Quantum Vortices in p-Wave Superconductors.* Phys. Rev. Lett. **86**, 268–271 (2001).

[6] A. Y. Kitaev. *Unpaired Majorana fermions in quantum wires.* Physics-Uspekhi **44**, 131–136 (2001).

[7] T. Senthil and M. P. A. Fisher. *Quasiparticle localization in superconductors with spin-orbit scattering.* Phys. Rev. B **61**, 9690–9698 (2000).

[8] L. Fu and C. L. Kane. *Superconducting Proximity Effect and Majorana Fermions at the Surface of a Topological Insulator.* Phys. Rev. Lett. **100**, 096407 (2008).

[9] R. M. Lutchyn, J. D. Sau, and S. Das Sarma. *Majorana Fermions and a Topological Phase Transition in Semiconductor-Superconductor Heterostructures.* Phys. Rev. Lett. **105**, 077001 (2010).

[10] X.-L. Qi and S.-C. Zhang. *Topological insulators and superconductors*. Rev. Mod. Phys. **83**, 1057–1110 (2011).

[11] C. Beenakker. *Search for Majorana Fermions in Superconductors*. Annual Review of Condensed Matter Physics **4**, 113–136 (2013).

[12] C. W. J. Beenakker. *Random-matrix theory of Majorana fermions and topological superconductors*. Rev. Mod. Phys. **87**, 1037–1066 (2015).

[13] G. Moore and N. Read. *Nonabelions in the fractional quantum hall effect*. Nuclear Physics B **360**, 362 –396 (1991).

[14] J. Alicea, Y. Oreg, G. Refael, F. von Oppen, and M. P. A. Fisher. *Non-Abelian statistics and topological quantum information processing in 1D wire networks*. Nature Physics **7**, 412–417 (2011).

[15] S. Das Sarma, M. Freedman, and C. Nayak. *Majorana zero modes and topological quantum computation*. npj Quantum Information **1**, 15001 (2015).

[16] M. Z. Hasan and C. L. Kane. *Colloquium: Topological insulators*. Rev. Mod. Phys. **82**, 3045–3067 (2010).

[17] M. Sato and S. Fujimoto. *Majorana Fermions and Topology in Superconductors*. Journal of the Physical Society of Japan **85**, 072001 (2016).

[18] C. Beenakker and L. Kouwenhoven. *A road to reality with topological superconductors*. Nature Physics **12**, 618–621 (2016).

[19] A. R. Akhmerov, J. Nilsson, and C. W. J. Beenakker. *Electrically Detected Interferometry of Majorana Fermions in a Topological Insulator*. Phys. Rev. Lett. **102**, 216404 (2009).

[20] L. Fu and C. L. Kane. *Probing Neutral Majorana Fermion Edge Modes with Charge Transport*. Phys. Rev. Lett. **102**, 216403 (2009).

[21] X.-L. Qi, T. L. Hughes, and S.-C. Zhang. *Chiral topological superconductor from the quantum Hall state*. Phys. Rev. B **82**, 184516 (2010).

[22] Q. L. He, L. Pan, A. L. Stern, E. C. Burks, X. Che, G. Yin, J. Wang, B. Lian, Q. Zhou, E. S. Choi, K. Murata, X. Kou, Z. Chen, T. Nie, Q. Shao, Y. Fan, S.-C. Zhang, K. Liu, J. Xia, and K. L. Wang. *Chiral Majorana fermion modes in a quantum anomalous Hall insulator-superconductor structure*. Science **357**, 294–299 (2017).

[23] A. Belavin, A. Polyakov, and A. Zamolodchikov. *Infinite conformal symmetry in two-dimensional quantum field theory*. Nuclear Physics B **241**, 333 –380 (1984).

[24] H. W. J. Blöte, J. L. Cardy, and M. P. Nightingale. *Conformal invariance, the central charge, and universal finite-size amplitudes at criticality*. Phys. Rev. Lett. **56**, 742–745 (1986).

[25] H. Sumiyoshi and S. Fujimoto. *Quantum Thermal Hall Effect in a Time-Reversal-Symmetry-Broken Topological Superconductor in Two Dimensions: Approach from Bulk Calculations*. Journal of the Physical Society of Japan **82**, 023602 (2013).

[26] B. Bradlyn and N. Read. *Low-energy effective theory in the bulk for transport in a topological phase*. Phys. Rev. B **91**, 125303 (2015).

[27] A. Kitaev. *A simple model of quantum holography*. KITP Program: Entanglement in Strongly-Correlated Quantum Matter (Apr 6 - Jul 2, 2015).

[28] S. Sachdev and J. Ye. *Gapless spin-fluid ground state in a random quantum Heisenberg magnet*. Phys. Rev. Lett. **70**, 3339–3342 (1993).

[29] J. Maldacena and D. Stanford. *Remarks on the Sachdev-Ye-Kitaev model*. Phys. Rev. D **94**, 106002 (2016).

[30] J. Polchinski and V. Rosenhaus. *The spectrum in the Sachdev-Ye-Kitaev model*. Journal of High Energy Physics **2016**, 1 (2016).

[31] A. Chew, A. Essin, and J. Alicea. *Approximating the Sachdev-Ye-Kitaev model with Majorana wires*. Phys. Rev. B **96**, 121119 (2017).

[32] D. I. Pikulin and M. Franz. *Black Hole on a Chip: Proposal for a Physical Realization of the Sachdev-Ye-Kitaev model in a Solid-State System*. Phys. Rev. X **7**, 031006 (2017).

[33] Y. S. Hor, A. J. Williams, J. G. Checkelsky, P. Roushan, J. Seo, Q. Xu, H. W. Zandbergen, A. Yazdani, N. P. Ong, and R. J. Cava. *Superconductivity in $Cu_xBi_2Se_3$ and its Implications for Pairing in the Undoped Topological Insulator*. Phys. Rev. Lett. **104**, 057001 (2010).

[34] S. Sasaki, M. Kriener, K. Segawa, K. Yada, Y. Tanaka, M. Sato, and Y. Ando. *Topological Superconductivity in $Cu_xBi_2Se_3$*. Phys. Rev. Lett. **107**, 217001 (2011).

[35] N. Levy, T. Zhang, J. Ha, F. Sharifi, A. A. Talin, Y. Kuk, and J. A. Stroscio. *Experimental Evidence for s-Wave Pairing Symmetry in Superconducting $Cu_xBi_2Se_3$ Single Crystals Using a Scanning Tunneling Microscope*. Phys. Rev. Lett. **110**, 117001 (2013).

[36] K. Matano, M. Kriener, K. Segawa, Y. Ando, and G.-q. Zheng. *Spin-rotation symmetry breaking in the superconducting state of $Cu_xBi_2Se_3$*. Nature Physics **12**, 852–854 (2016).

[37] T. Asaba, B. J. Lawson, C. Tinsman, L. Chen, P. Corbae, G. Li, Y. Qiu, Y. S. Hor, L. Fu, and L. Li. *Rotational Symmetry Breaking in a Trigonal Superconductor Nb-doped Bi_2Se_3*. Phys. Rev. X **7**, 011009 (2017).

[38] A. R. Akhmerov, J. P. Dahlhaus, F. Hassler, M. Wimmer, and C. W. J. Beenakker. *Quantized Conductance at the Majorana Phase Transition in a Disordered Superconducting Wire*. Phys. Rev. Lett. **106**, 057001 (2011).

[39] Y. Blanter and M. Büttiker. *Shot noise in mesoscopic conductors*. Physics Reports **336**, 1 –166 (2000).

[40] C. Beenakker and C. Schönenberger. *Quantum Shot Noise*. Physics Today **56**, 5, 37 (2003).

[41] S. F. Edwards and P. W. Anderson. *Theory of spin glasses*. Journal of Physics F: Metal Physics **5**, 965–974 (1975).

[42] D. Sherrington and S. Kirkpatrick. *Solvable Model of a Spin-Glass*. Phys. Rev. Lett. **35**, 1792–1796 (1975).

[43] G. Gur-Ari, R. Mahajan, and A. Vaezi. *Does the SYK model have a spin glass phase?*, Journal of High Energy Physics **2018**, 70 (2018).

[44] H. Wang, D. Bagrets, A. L. Chudnovskiy, and A. Kamenev. *On the replica structure of Sachdev-Ye-Kitaev model*. (2018) arXiv:`1812.02666 [hep-th]`.

[45] J. Maldacena, S. H. Shenker, and D. Stanford. *A bound on chaos.* Journal of High Energy Physics **2016**, 106 (2016).

[46] S. A. Hartnoll, A. Lucas, and S. Sachdev. *Holographic quantum matter.* (2016) arXiv:1612.07324 [hep-th].

[47] S. Sachdev. *Bekenstein-Hawking Entropy and Strange Metals.* Phys. Rev. X **5**, 041025 (2015).

[48] S. Sachdev and B. Keimer. *Quantum Criticality.* Physics Today **64 (2)**, 29 (2011).

[49] J. Zaanen. *Why the temperature is high.* Nature **430**, 512–513 (2004).

[50] X.-Y. Song, C.-M. Jian, and L. Balents. *Strongly Correlated Metal Built from Sachdev-Ye-Kitaev Models.* Phys. Rev. Lett. **119**, 216601 (2017).

[51] A. I. Larkin and Y. N. Ovchinnikov. *Quasiclassical Method in the Theory of Superconductivity.* Sov. Phys. JETP **28**, 1200 (1969).

[52] B. Swingle. *Unscrambling the physics of out-of-time-order correlators.* Nature Physics **14**, 988–990 (2018).

[53] A. Chen, R. Ilan, F. de Juan, D. I. Pikulin, and M. Franz. *Quantum Holography in a Graphene Flake with an Irregular Boundary.* Phys. Rev. Lett. **121**, 036403 (2018).

[54] I. Danshita, M. Hanada, and M. Tezuka. *Creating and probing the Sachdev–Ye–Kitaev model with ultracold gases: Towards experimental studies of quantum gravity.* Progress of Theoretical and Experimental Physics **2017** (2017).

[55] M. Franz and M. Rozali. *Mimicking black hole event horizons in atomic and solid-state systems.* Nature Reviews Materials **3**, 491–501 (2018).

[56] A. Georges, O. Parcollet, and S. Sachdev. *Quantum fluctuations of a nearly critical Heisenberg spin glass.* Phys. Rev. B **63**, 134406 (2001).

[57] A. H. Castro Neto, F. Guinea, N. M. R. Peres, K. S. Novoselov, and A. K. Geim. *The electronic properties of graphene.* Rev. Mod. Phys. **81**, 109–162 (2009).

[58] Y. Aharonov and A. Casher. *Ground state of a spin-½ charged particle in a two-dimensional magnetic field.* Phys. Rev. A **19**, 2461–2462 (1979).

[59] M Diez, I. C. Fulga, D. I. Pikulin, J Tworzydło, and C. W. J. Beenakker. *Bimodal conductance distribution of Kitaev edge modes in topological superconductors.* New Journal of Physics **16**, 063049 (2014).

[60] K. Nomura, S. Ryu, A. Furusaki, and N. Nagaosa. *Cross-Correlated Responses of Topological Superconductors and Superfluids.* Phys. Rev. Lett. **108**, 026802 (2012).

[61] U. Sivan and Y. Imry. *Multichannel Landauer formula for thermoelectric transport with application to thermopower near the mobility edge.* Phys. Rev. B **33**, 551–558 (1986).

[62] M. P. Anantram and S. Datta. *Current fluctuations in mesoscopic systems with Andreev scattering.* Phys. Rev. B **53**, 16390–16402 (1996).

[63] N. V. Gnezdilov, B. van Heck, M. Diez, J. A. Hutasoit, and C. W. J. Beenakker. *Topologically protected charge transfer along the edge of a chiral p-wave superconductor.* Phys. Rev. B **92**, 121406 (2015).

[64] G. E. Volovik. *The Universe in a Helium Droplet.* (Oxford University Press, 2009).

[65] M. S. Foster, H.-Y. Xie, and Y.-Z. Chou. *Topological protection, disorder, and interactions: Survival at the surface of three-dimensional topological superconductors.* Phys. Rev. B **89**, 155140 (2014).

[66] R. Queiroz and A. P. Schnyder. *Helical Majorana surface states of strongly disordered topological superconductors with time-reversal symmetry.* Phys. Rev. B **91**, 014202 (2015).

[67] R. Nakai and K. Nomura. *Disorder effects on thermal transport on the surface of topological superconductors by the self-consistent Born approximation.* Phys. Rev. B **89**, 064503 (2014).

[68] C. Mahaux and H. A. Weidenmüller. *Shell-Model Approach to Nuclear Reactions.* (Interscience (Wiley), North-Holland, Amsterdam, 1969).

[69] J. Tworzydło, B. Trauzettel, M. Titov, A. Rycerz, and C. W. J. Beenakker. *Sub-Poissonian Shot Noise in Graphene.* Phys. Rev. Lett. **96**, 246802 (2006).

[70] H.-Y. Xie, Y.-Z. Chou, and M. S. Foster. *Surface transport coefficients for three-dimensional topological superconductors*. Phys. Rev. B **91**, 024203 (2015).

[71] M. I. Katsnelson. *Zitterbewegung, chirality, and minimal conductivity in graphene*. The European Physical Journal B - Condensed Matter and Complex Systems **51**, 157–160 (2006).

[72] C. W. Groth, M. Wimmer, A. R. Akhmerov, and X. Waintal. *Kwant: a software package for quantum transport*. New Journal of Physics **16**, 063065 (2014).

[73] S. Ryu, A. P. Schnyder, A. Furusaki, and A. W. W. Ludwig. *Topological insulators and superconductors: tenfold way and dimensional hierarchy*. New Journal of Physics **12**, 065010 (2010).

[74] M. Titov, P. M. Ostrovsky, I. V. Gornyi, A. Schuessler, and A. D. Mirlin. *Charge Transport in Graphene with Resonant Scatterers*. Phys. Rev. Lett. **104**, 076802 (2010).

[75] L. S. Levitov and G. B. Lesovik. *Charge distribution in quantum shot noise*. JETP Lett. **58**, 230 (1993).

[76] B. A. Muzykantskii and D. E. Khmelnitskii. *Quantum shot noise in a normal-metal–superconductor point contact*. Phys. Rev. B **50**, 3982–3987 (1994).

[77] A. F. Andreev. *The thermal conductivity of the intermediate state in superconductor*. Sov. Phys. JETP **19**, 1228 (1964).

[78] Z.-Z. Li, C.-H. Lam, and J. Q. You. *Probing Majorana bound states via counting statistics of a single electron transistor*. Sci. Rep. **5**, 11416 (2015).

[79] H. Soller and A. Komnik. *Charge transfer statistics of transport through Majorana bound states*. Physica E: Low-dimensional Systems and Nanostructures **63**, 99 –104 (2014).

[80] D. E. Liu, M. Cheng, and R. M. Lutchyn. *Probing Majorana physics in quantum-dot shot-noise experiments*. Phys. Rev. B **91**, 081405 (2015).

[81] I. Klich. *Full Counting Statistics: An elementary derivation of Levitov's formula*. (2002) arXiv:`cond - mat / 0209642 [cond-mat.mes-hall]`.

[82] J. E. Avron, S. Bachmann, G. M. Graf, and I. Klich. *Fredholm Determinants and the Statistics of Charge Transport.* Communications in Mathematical Physics **280**, 807–829 (2008).

[83] V. Mourik, K. Zuo, S. M. Frolov, S. R. Plissard, E. P. A. M. Bakkers, and L. P. Kouwenhoven. *Signatures of Majorana Fermions in Hybrid Superconductor-Semiconductor Nanowire Devices.* Science **336**, 1003–1007 (2012).

[84] S. Nadj-Perge, I. K. Drozdov, J. Li, H. Chen, S. Jeon, J. Seo, A. H. MacDonald, B. A. Bernevig, and A. Yazdani. *Observation of Majorana fermions in ferromagnetic atomic chains on a superconductor.* Science **346**, 602–607 (2014).

[85] G. Strübi, W. Belzig, M.-S. Choi, and C. Bruder. *Interferometric and Noise Signatures of Majorana Fermion Edge States in Transport Experiments.* Phys. Rev. Lett. **107**, 136403 (2011).

[86] G. Strübi, W. Belzig, T. L. Schmidt, and C. Bruder. *Full counting statistics of Majorana interferometers.* Physica E: Low-dimensional Systems and Nanostructures **74**, 489 –495 (2015).

[87] M. Stone and R. Roy. *Edge modes, edge currents, and gauge invariance in $p_x + ip_y$ superfluids and superconductors.* Phys. Rev. B **69**, 184511 (2004).

[88] D. Wang, Z. Huang, and C. Wu. *Fate and remnants of Majorana zero modes in a quantum wire array.* Phys. Rev. B **89**, 174510 (2014).

[89] R. Wakatsuki, M. Ezawa, and N. Nagaosa. *Majorana fermions and multiple topological phase transition in Kitaev ladder topological superconductors.* Phys. Rev. B **89**, 174514 (2014).

[90] I. Seroussi, E. Berg, and Y. Oreg. *Topological superconducting phases of weakly coupled quantum wires.* Phys. Rev. B **89**, 104523 (2014).

[91] I. C. Fulga, B. van Heck, J. M. Edge, and A. R. Akhmerov. *Statistical topological insulators.* Phys. Rev. B **89**, 155424 (2014).

[92] J. Li, T. Neupert, Z. J. Wang, A. H. MacDonald, A. B. Yazdani, and B. A. Bernevig. *Two-dimensional chiral topological superconductivity in Shiba lattices.* Nature Communications **7**, 12297 (2016).

[93] Y. Lu, W.-Y. He, D.-H. Xu, N. Lin, and K. T. Law. *Platform for engineering topological superconductors: Superlattices on Rashba superconductors*. Phys. Rev. B **94**, 024507 (2016).

[94] A. Milsted, L. Seabra, I. C. Fulga, C. W. J. Beenakker, and E. Cobanera. *Statistical translation invariance protects a topological insulator from interactions*. Phys. Rev. B **92**, 085139 (2015).

[95] A. Rahmani, X. Zhu, M. Franz, and I. Affleck. *Phase diagram of the interacting Majorana chain model*. Phys. Rev. B **92**, 235123 (2015).

[96] J. Röntynen and T. Ojanen. *Topological Superconductivity and High Chern Numbers in 2D Ferromagnetic Shiba Lattices*. Phys. Rev. Lett. **114**, 236803 (2015).

[97] T. Scaffidi and S. H. Simon. *Large Chern Number and Edge Currents in Sr_2RuO_4*. Phys. Rev. Lett. **115**, 087003 (2015).

[98] J. R. Schaibley, H. Yu, G. Clark, P. Rivera, J. S. Ross, K. L. Seyler, W. Yao, and X. Xu. *Valleytronics in 2D materials*. Nature Reviews Materials **1**, 16055 (2016).

[99] S. K. Wang and J. Wang. *Valley precession in graphene superlattices*. Phys. Rev. B **92**, 075419 (2015).

[100] F. Xu, Z. Yu, Y. Ren, B. Wang, Y. Wei, and Z. Qiao. *Transmission spectra and valley processing of graphene and carbon nanotube superlattices with inter-valley coupling*. New Journal of Physics **18**, 113011 (2016).

[101] X. Wu and H. Meng. *Tunable valley filtering in graphene with intervalley coupling*. EPL (Europhysics Letters) **114**, 37008 (2016).

[102] Q.-P. Wu, Z.-F. Liu, A.-X. Chen, X.-B. Xiao, H. Zhang, and G.-X. Miao. *Valley precession and valley polarization in graphene with inter-valley coupling*. Journal of Physics: Condensed Matter **29**, 395303 (2017).

[103] Y. Ren, X. Deng, Z. Qiao, C. Li, J. Jung, C. Zeng, Z. Zhang, and Q. Niu. *Single-valley engineering in graphene superlattices*. Phys. Rev. B **91**, 245415 (2015).

[104] G. Giovannetti, M. Capone, J. van den Brink, and C. Ortix. *Kekulé textures, pseudospin-one Dirac cones, and quadratic band crossings in a graphene-hexagonal indium chalcogenide bilayer*. Phys. Rev. B **91**, 121417 (2015).

[105] J. W. F. Venderbos, M. Manzardo, D. V. Efremov, J. van den Brink, and C. Ortix. *Engineering interaction-induced topological insulators in a $\sqrt{3} \times \sqrt{3}$ substrate-induced honeycomb superlattice*. Phys. Rev. B **93**, 045428 (2016).

[106] F. de Juan. *Non-Abelian gauge fields and quadratic band touching in molecular graphene*. Phys. Rev. B **87**, 125419 (2013).

[107] W. Han, R. K. Kawakami, M. Gmitra, and J. Fabian. *Graphene spintronics*. Nature Nanotechnology **9**, 794–807 (2014).

[108] A. Altland and M. R. Zirnbauer. *Nonstandard symmetry classes in mesoscopic normal-superconducting hybrid structures*. Phys. Rev. B **55**, 1142–1161 (1997).

[109] I. Snyman, J. Tworzydło, and C. W. J. Beenakker. *Calculation of the conductance of a graphene sheet using the Chalker-Coddington network model*. Phys. Rev. B **78**, 045118 (2008).

[110] S. Sachdev. *Holographic Metals and the Fractionalized Fermi Liquid*. Phys. Rev. Lett. **105**, 151602 (2010).

[111] A. Kitaev and S. J. Suh. *The soft mode in the Sachdev-Ye-Kitaev model and its gravity dual*. Journal of High Energy Physics **2018**, 183 (2018).

[112] R. A. Davison, W. Fu, A. Georges, Y. Gu, K. Jensen, and S. Sachdev. *Thermoelectric transport in disordered metals without quasiparticles: The Sachdev-Ye-Kitaev models and holography*. Phys. Rev. B **95**, 155131 (2017).

[113] P. Zhang. *Dispersive Sachdev-Ye-Kitaev model: Band structure and quantum chaos*. Phys. Rev. B **96**, 205138 (2017).

[114] Y. Gu, X.-L. Qi, and D. Stanford. *Local criticality, diffusion and chaos in generalized Sachdev-Ye-Kitaev models*. Journal of High Energy Physics **2017**, 125 (2017).

[115] X. Chen, R. Fan, Y. Chen, H. Zhai, and P. Zhang. *Competition between Chaotic and Nonchaotic Phases in a Quadratically Coupled Sachdev-Ye-Kitaev Model*. Phys. Rev. Lett. **119**, 207603 (2017).

[116] D. Ben-Zion and J. McGreevy. *Strange metal from local quantum chaos*. Phys. Rev. B **97**, 155117 (2018).

[117] A. Haldar, S. Banerjee, and V. B. Shenoy. *Higher-dimensional Sachdev-Ye-Kitaev non-Fermi liquids at Lifshitz transitions.* Phys. Rev. B **97**, 241106 (2018).

[118] Y. Zhong. *Periodic Anderson model meets Sachdev-Ye-Kitaev interaction: a solvable playground for heavy fermion physics.* Journal of Physics Communications **2**, 095014 (2018).

[119] D. Bagrets, A. Altland, and A. Kamenev. *Sachdev–Ye–Kitaev model as Liouville quantum mechanics.* Nuclear Physics B **911**, 191 –205 (2016).

[120] D. Bagrets, A. Altland, and A. Kamenev. *Power-law out of time order correlation functions in the SYK model.* Nuclear Physics B **921**, 727 –752 (2017).

[121] A. V. Lunkin, K. S. Tikhonov, and M. V. Feigel'man. *Sachdev-Ye-Kitaev Model with Quadratic Perturbations: The Route to a Non-Fermi Liquid.* Phys. Rev. Lett. **121**, 236601 (2018).

[122] S. Banerjee and E. Altman. *Solvable model for a dynamical quantum phase transition from fast to slow scrambling.* Phys. Rev. B **95**, 134302 (2017).

[123] L. V Keldysh. *Diagram technique for nonequilibrium processes.* Sov. Phys. JETP **20**, 1018 (1965).

[124] L. S. Levitov, H. Lee, and G. B. Lesovik. *Electron counting statistics and coherent states of electric current.* Journal of Mathematical Physics **37**, 4845–4866 (1996).

[125] A. Kamenev. *Field Theory of Non-Equilibrium Systems.* (Cambridge University Press, 2011).

[126] A. Eberlein, V. Kasper, S. Sachdev, and J. Steinberg. *Quantum quench of the Sachdev-Ye-Kitaev model.* Phys. Rev. B **96**, 205123 (2017).

[127] A. I. Larkin and Y. N. Ovchinnikov. *Nonlinear conductivity of superconductors in the mixed state.* Sov. Phys. JETP **41**, 960 (1975).

[128] O. Parcollet, A. Georges, G. Kotliar, and A. Sengupta. *Overscreened multichannel $SU(N)$ Kondo model: Large-N solution and conformal field theory.* Phys. Rev. B **58**, 3794–3813 (1998).

[129] U. Fano. *Effects of Configuration Interaction on Intensities and Phase Shifts.* Phys. Rev. **124**, 1866–1878 (1961).

[130] J. Zaanen and G. A. Sawatzky. *Strong interference between decay channels and valence-electron rearrangements in core-hole spectroscopy*. Phys. Rev. B **33**, 8074–8083 (1986).

[131] A. E. Miroshnichenko, S. Flach, and Y. S. Kivshar. *Fano resonances in nanoscale structures*. Rev. Mod. Phys. **82**, 2257–2298 (2010).

[132] C. M. Varma, P. B. Littlewood, S. Schmitt-Rink, E. Abrahams, and A. E. Ruckenstein. *Phenomenology of the normal state of Cu-O high-temperature superconductors*. Phys. Rev. Lett. **63**, 1996–1999 (1989).

[133] S. Sachdev. *Quantum Phase Transitions*. 2nd ed. (Cambridge University Press, 2011).

[134] B. Keimer, S. A. Kivelson, M. R. Norman, S. Uchida, and J. Zaanen. *From quantum matter to high-temperature superconductivity in copper oxides*. Nature **518**, 179–186 (2015).

[135] E. Uspesnkiy. *Crocodile Gena and His Friends*. (Sov. DETGIZ, 1966).

[136] A. A. Patel, J. McGreevy, D. P. Arovas, and S. Sachdev. *Magnetotransport in a Model of a Disordered Strange Metal*. Phys. Rev. X **8**, 021049 (2018).

[137] J. Zaanen, Y. Liu, Y.-W. Sun, and K. Schalm. *Holographic Duality in Condensed Matter Physics*. (Cambridge University Press, 2015).

[138] M. Čubrović, J. Zaanen, and K. Schalm. *String Theory, Quantum Phase Transitions, and the Emergent Fermi Liquid*. Science **325**, 439–444 (2009).

[139] T. Faulkner, N. Iqbal, H. Liu, J. McGreevy, and D. Vegh. *Strange Metal Transport Realized by Gauge/Gravity Duality*. Science **329**, 1043–1047 (2010).

[140] T. Faulkner, H. Liu, J. McGreevy, and D. Vegh. *Emergent quantum criticality, Fermi surfaces, and AdS_2*. Phys. Rev. D **83**, 125002 (2011).

[141] N. Iqbal, H. Liu, and M. Mezei. *Semi-local quantum liquids*. Journal of High Energy Physics **2012**, 86 (2012).

[142] Y. Liu, K. Schalm, Y.-W. Sun, and J. Zaanen. *Lattice potentials and fermions in holographic non Fermi-liquids: hybridizing local quantum criticality*. Journal of High Energy Physics **2012**, 36 (2012).

[143] Y. Ling, C. Niu, J.-P. Wu, Z.-Y. Xian, and H. Zhang. *Holographic fermionic liquid with lattices.* Journal of High Energy Physics **2013**, 45 (2013).

[144] S. Cremonini, L. Li, and J. Ren. *Holographic fermions in striped phases.* Journal of High Energy Physics **2018**, 80 (2018).

[145] F. Balm, A. Krikun, A. Romero-Bermúdez, K. Schalm, and J. Zaanen. *Isolated zeroes destroy Fermi surface in holographic models with lattice.* (manuscript in preparation).

[146] A. A. Abrikosov and L. P. Gor'kov. *Contribution to the theory of superconducting alloys with paramagnetic impurities.* Sov. Phys. JETP **12**, 1243 (1961).

[147] F. Reif and M. A. Woolf. *Energy Gap in Superconductors Containing Paramagnetic Impurities.* Phys. Rev. Lett. **9**, 315–316 (1962).

[148] L. P. Gor'kov. *On the energy spectrum of superconductors.* Sov. Phys. JETP **7**, 505 (1958).

[149] A. Altland and B. D. Simons. *Condensed Matter Field Theory.* 2nd ed. (Cambridge University Press, 2010).

[150] V. L. Berezinskii. *New model of the anisotropic phase of superfluid He^3.* JETP Lett. **20**, 287 (1974).

[151] J. Linder and A. V. Balatsky. *Odd-frequency superconductivity.* (2017) arXiv:1709.03986 [cond-mat.supr-con].

[152] S.-P. Lee, R. M. Lutchyn, and J. Maciejko. *Odd-frequency superconductivity in a nanowire coupled to Majorana zero modes.* Phys. Rev. B **95**, 184506 (2017).

[153] Y. Tanaka and A. A. Golubov. *Theory of the Proximity Effect in Junctions with Unconventional Superconductors.* Phys. Rev. Lett. **98**, 037003 (2007).

[154] Y. Tanaka, M. Sato, and N. Nagaosa. *Symmetry and Topology in Superconductors –Odd-Frequency Pairing and Edge States–.* Journal of the Physical Society of Japan **81**, 011013 (2012).

[155] L. Kouwenhoven and C. Marcus. *Quantum dots.* Physics World **11**, 35–40 (1998).

[156] L. Fidkowski, J. Alicea, N. H. Lindner, R. M. Lutchyn, and M. P. A. Fisher. *Universal transport signatures of Majorana fermions in superconductor-Luttinger liquid junctions.* Phys. Rev. B **85**, 245121 (2012).

[157] M. Cheng, M. Becker, B. Bauer, and R. M. Lutchyn. *Interplay between Kondo and Majorana Interactions in Quantum Dots.* Phys. Rev. X **4**, 031051 (2014).

[158] Z. Huang, P. Wölfle, and A. V. Balatsky. *Odd-frequency pairing of interacting Majorana fermions.* Phys. Rev. B **92**, 121404 (2015).

[159] O. Viehmann, J. von Delft, and F. Marquardt. *Superradiant Phase Transitions and the Standard Description of Circuit QED.* Phys. Rev. Lett. **107**, 113602 (2011).

[160] S. I. Mukhin and M. V. Fistul. *Generation of non-classical photon states in superconducting quantum metamaterials.* Superconductor Science and Technology **26**, 084003 (2013).

[161] M. A. Iontsev, S. I. Mukhin, and M. V. Fistul. *Double-resonance response of a superconducting quantum metamaterial: Manifestation of nonclassical states of photons.* Phys. Rev. B **94**, 174510 (2016).

[162] M. Bamba, K. Inomata, and Y. Nakamura. *Superradiant Phase Transition in a Superconducting Circuit in Thermal Equilibrium.* Phys. Rev. Lett. **117**, 173601 (2016).

[163] P. Nataf and C. Ciuti. *No-go theorem for superradiant quantum phase transitions in cavity QED and counter-example in circuit QED.* Nature Communications **1**, 72 (2010).

[164] T. Jaako, Z.-L. Xiang, J. J. Garcia-Ripoll, and P. Rabl. *Ultrastrong-coupling phenomena beyond the Dicke model.* Phys. Rev. A **94**, 033850 (2016).

[165] A. Blais, R.-S. Huang, A. Wallraff, S. M. Girvin, and R. J. Schoelkopf. *Cavity quantum electrodynamics for superconducting electrical circuits: An architecture for quantum computation.* Phys. Rev. A **69**, 062320 (2004).

[166] A. Wallraff, D. I. Schuster, A. Blais, L. Frunzio, R.-S. Huang, J. Majer, S. Kumar, S. M. Girvin, and S. R. J. *Strong coupling of a single photon to a superconducting qubit using circuit quantum electrodynamics.* Nature **431**, 162–167 (2004).

[167] J. M. Raimond, M. Brune, and S. Haroche. *Manipulating quantum entanglement with atoms and photons in a cavity.* Rev. Mod. Phys. **73**, 565–582 (2001).

[168] L. DiCarlo, M. D. Reed, L. Sun, B. R. Johnson, J. M. Chow, J. M. Gambetta, L. Frunzio, S. M. Girvin, M. H. Devoret, and R. J. Schoelkopf. *Preparation and measurement of three-qubit entanglement in a superconducting circuit.* Nature **467**, 574–578 (2010).

[169] R. H. Dicke. *Coherence in Spontaneous Radiation Processes.* Phys. Rev. **93**, 99–110 (1954).

[170] K. Rzażewski, K. Wódkiewicz, and W. Żakowicz. *Phase Transitions, Two-Level Atoms, and the A^2 Term.* Phys. Rev. Lett. **35**, 432–434 (1975).

[171] I. Bialynicki-Birula. *No-go theorem concerning the superradiant phase transition in atomic systems.* Phys. Rev. A **19**, 301–303 (1979).

[172] J. Keeling. *Coulomb interactions, gauge invariance, and phase transitions of the Dicke model.* Journal of Physics: Condensed Matter **19**, 295213 (2007).

[173] M. C. Cassidy, A. Bruno, S. Rubbert, M. Irfan, J. Kammhuber, R. N. Schouten, A. R. Akhmerov, and L. P. Kouwenhoven. *Demonstration of an ac Josephson junction laser.* Science **355**, 939–942 (2017).

[174] H. Asai, S. Savel'ev, S. Kawabata, and A. M. Zagoskin. *Effects of lasing in a one-dimensional quantum metamaterial.* Phys. Rev. B **91**, 134513 (2015).

[175] W. Kopylov, C. Emary, E. Schöll, and T. Brandes. *Time-delayed feedback control of the Dicke–Hepp–Lieb superradiant quantum phase transition.* New Journal of Physics **17**, 013040 (2015).

[176] O. Astafiev, K. Inomata, A. O. Niskanen, T. Yamamoto, Y. A. Pashkin, Y. Nakamura, and J. S. Tsai. *Single artificial-atom lasing.* Nature **449**, 588–590 (2007).

[177] S Ashhab, J. R. Johansson, A. M. Zagoskin, and F. Nori. *Single-artificial-atom lasing using a voltage-biased superconducting charge qubit.* New Journal of Physics **11**, 023030 (2009).

[178] S. André, V. Brosco, M. Marthaler, A. Shnirman, and G. Schön. *Few-qubit lasing in circuit QED*. Physica Scripta **T137**, 014016 (2009).

[179] E. Almaas and D. Stroud. *Dynamics of a Josephson array in a resonant cavity*. Phys. Rev. B **65**, 134502 (2002).

[180] W. A. Al-Saidi and D. Stroud. *Eigenstates of a small Josephson junction coupled to a resonant cavity*. Phys. Rev. B **65**, 014512 (2001).

[181] C. Emary and T. Brandes. *Chaos and the quantum phase transition in the Dicke model*. Phys. Rev. E **67**, 066203 (2003).

[182] N. Lambert, C. Emary, and T. Brandes. *Entanglement and the Phase Transition in Single-Mode Superradiance*. Phys. Rev. Lett. **92**, 073602 (2004).

[183] A. Shnirman, G. Schön, and Z. Hermon. *Quantum Manipulations of Small Josephson Junctions*. Phys. Rev. Lett. **79**, 2371–2374 (1997).

[184] T. Holstein and H. Primakoff. *Field Dependence of the Intrinsic Domain Magnetization of a Ferromagnet*. Phys. Rev. **58**, 1098–1113 (1940).

[185] Y. Todorov, A. M. Andrews, R. Colombelli, S. De Liberato, C. Ciuti, P. Klang, G. Strasser, and C. Sirtori. *Ultrastrong Light-Matter Coupling Regime with Polariton Dots*. Phys. Rev. Lett. **105**, 196402 (2010).

Summary

Majorana fermions in superconductors are the subgap quasiparticle excitations that are their own antiparticles. They are an equal weight quantum superposition of a positively charged electron and a negatively charged hole, that makes them charge-neutral but not an eigenstate of charge. Although the expectation value of charge is therefore zero, there are fluctuations of charge. This would enable a purely electrical detection of Majorana states, outdoing low-temperature thermal measurements. The fluctuations of the charge carried by Majorana fermions in superconductors are studied in the first two chapters of this thesis.

Majorana fermions occur on the boundary of so-called topological superconductors, either the one-dimensional edge of a two-dimensional system or the two-dimensional surface of a three-dimensional system. In chapter 2 we show that the charge fluctuations (electrical shot noise) are proportional to the thermal conductance, with a coefficient made up only from fundamental constants and the temperature. This result stems from the combination of time reversal and electron-hole symmetries.

The electrical shot noise (the second moment of the charge fluctuations) generated by the Majorana fermion in a single edge channel is quantised in units of $\frac{1}{2} \times e^2/h$ per eV voltage bias. In chapter 3 we extend the quantization to all even moments of the charge fluctuations. At low temperatures the full probability distribution of the charge fluctuations is trinomial: a Majorana fermion transfers either $-e$, 0 or $+e$ charge, with the corresponding probabilities 1/4, 1/2 and 1/4. This result is drastically different from the usual binomial statistics of electrons.

In chapter 4 we proceed from topological superconductors to graphene, which is a single carbon layer. Although graphene is not superconducting, we demonstrate that there exists an analogy with Andreev reflection in a topological superconductor. In a superlattice of graphene on a suitable substrate an anti-unitary symmetry occurs. The latter one is mathemati-

cally equivalent to electron-hole symmetry in a superconductor. The "valley index" K, K' in graphene then plays the role of the electron-hole degree of freedom. Thus, the electron approaching perpendicularly to the interface between pristine graphene and a graphene superlattice is reflected in the opposite valley, just as Andreev reflection scatters an electron into a hole and vice versa.

The properties of the systems mentioned above can be captured by non-interacting theories at low energy scale. In the second part of the thesis, we deal with the effects of strong interactions between the particles. In particular we focus on the Sachdev-Ye-Kitaev (SYK) model that describes a metal with strong infinite-range interactions (mean strength J) between N fermions (Dirac/Majorana). The model is solvable in the large N limit, where a conformal symmetry emerges in the infrared. The transport observables resulting from the SYK model are considered in the three following chapters.

In chapter 5 we predict that the tunneling spectroscopy of the complex-valued SYK model shows a duality between low and high voltage: The differential conductance G depends on the applied voltage eV only through the dimensionless parameter $\xi = eVJ/\Gamma^2$ and obeys the duality relation $G(\xi) = G(\pi/\xi)$, where Γ characterizes coupling to the probe. This property of the current-voltage characteristic reveals the underlying conformal symmetry of the SYK model.

In chapter 6 we show that in a system that contains at least two discrete states that are coupled to a quantum continuum, one can see the isolated zero point in the spectral function of one of the states at the frequency of the other state. This phenomenon makes it possible to test the continuous behavour of the spectral function of the SYK model. An electron propagating through a lattice of the SYK nodes is scattered by those in a way that produces a characteristic "holographic" spectral function with a line of zeros.

In chapter 7 we point out that a quantum dot becomes superconducting close to Majorana fermions described by the SYK model. Despite the induced superconducting order parameter, which is an odd function of frequency, there is no excitation gap. The occurrence of "gapless superconductivity" can be measured spectroscopically.

In the final chapter of this thesis, we consider a system with an infinitely ranged interaction without disorder, in contrast with the SYK model. The interaction arises from the gauge-invariant coupling of N

low-capacitance Josephson junctions to a photon in a microwave cavity. The effective theory of the system turns out to be an extended Dicke Hamiltonian of N spins-1/2 with all-to-all repulsive interaction. We propose a rotating Holstein-Primakoff representation for the total spin of N particles, which enables us to uncover the first-order phase transition in the large N limit.

Samenvatting

Majorana-fermionen in supergeleiders zijn deeltjes die hun eigen antideeltje zijn. Het zijn deeltjes in een quantumsuperpositie met gelijk gewicht van positief geladen elektronen en negatief geladen gaten, waardoor ze ladingsneutraal zijn maar geen eigentoestand van lading. Hoewel de verwachtingswaarde van de lading dus gelijk is aan nul, zijn er fluctuaties van de lading. Dit maakt het mogelijk om Majorana-fermionen langs elektrische weg te detecteren, hetgeen bij lage temperaturen veel eenvoudiger is dan detectie via thermische geleiding. De fluctuaties van de lading gedragen door Majorana-fermionen in supergeleiders worden bestudeerd in de eerste twee hoofdstukken van dit proefschrift.

Majorana-fermionen treden op aan de buitenkant van zogenaamde topologische supergeleiders. Dat kan de één-dimensionale rand zijn van een twee-dimensionaal systeem of het twee-dimensionale oppervlak van een drie-dimensionaal systeem. In hoofdstuk 2 leiden we af dat de ladingsfluctuaties (hagelruis) direct gerelateerd zijn aan de thermische geleiding, via een relatie die alleen fundamentele constantes en de temperatuur bevat. Deze relatie volgt uit de combinatie van tijdomkeersymmetrie en elektron-gat symmetrie.

Het hagelruisvermogen (het tweede moment van de ladingsfluctuaties) dat wordt gegenereerd door de Majorana-fermionen in een enkel randkanaal is gequantiseerd in eenheden van $\frac{1}{2} \times e^2/h$ per eV aangelegde spanning. In hoofdstuk 3 breiden we de quantisatie uit naar alle even momenten van de ladingsfluctuaties. Bij lage temperaturen is de volledige kansverdeling van de ladingsfluctuaties trinominaal: een Majoranafermion zorgt voor een ladingsoverdracht van hetzij $-e$, 0 of $+e$ lading, met de bijbehorende kansen 1/4, 1/2 en 1/4. Dit resultaat is fundamenteel anders dan de gangbare binomiale statistiek van gewone fermionen.

In hoofdstuk 4 maken we de overstap van topologische supergeleiders naar grafeen, wat een enkele koolstoflaag is. Hoewel grafeen niet super-

geleidend is, laten we zien dat er een analogie is met Andreev reflectie in een topologische supergeleider. In een superrooster van grafeen op een geschikt substraat ontstaat een anti-unitaire symmetrie die wiskundig gezien geheel analoog is aan elektron-gat symmetrie in een supergeleider. De "valley index" K, K' in grafeen speelt dan de rol van de elektron-gat vrijheidsgraad. Aldus wordt het elektron dat het grensvlak loodrecht nadert gereflecteerd in de tegenovergestelde valley, net zoals bij Andreev reflectie van een elektron als een gat.

Tot zover hebben we vrije deeltjes beschreven. In het tweede deel van het proefschrift behandelen we de effecten van wisselwerking tussen de deeltjes. Een specifiek voorbeeld waar we ons op richten is het Sachdev-Ye-Kitaev (SYK)-model, dat een metaal beschrijft met sterke lange-dracht interacties (gemiddelde sterkte J) tussen N fermionen (Dirac-fermionen of Majorana-fermionen). Het model is oplosbaar in de grote-N-limiet, wanneer een conforme symmetrie optreedt. De experimenteel waarneembare effecten volgend uit het SYK-model worden in de drie volgende hoofdstukken behandeld.

In hoofdstuk 5 voorspellen we dat de tunneling spectroscopie van het SYK-model een dualiteit tussen lage en hoge spanning laat zien: het differentiële geleidingsvermogen G hangt alleen af van de toegepaste spanning V via de dimensieloze parameter $\xi = eVJ/\Gamma^2$ en voldoet aan de dualiteitsrelatie $G(\xi) = G(\pi/\xi)$, waarbij Γ de sterkte van de tunnelkoppeling karakteriseert. Deze eigenschap van de stroomspanningskarakteristiek onthult de onderliggende conforme symmetrie van het SYK-model.

Hoofdstuk 6 bestudeert de spectrale functie in het SYK-model. Voor een systeem dat ten minste twee geïsoleerde toestanden bevat die zijn gekoppeld aan een kwantumcontinuüm, kan men het geïsoleerde nulpunt in de spectrale functie van één van de toestanden waarnemen met behulp van de frequentie van de andere toestand. Dit verschijnsel maakt het mogelijk om de machtwetschaling van de spectrale functie van het SYK-model te testen. Een elektron dat gekoppeld is aan een "quantum dot" in de SYK-toestand wordt door de quantum dot verstrooid op een manier die een karakteristieke "holografische" spectrale functie voortbrengt.

In hoofdstuk 7 wijzen we erop dat een quantum dot supergeleidend wordt in de nabijheid van Majorana-fermionen die wisselwerken volgens het SYK-model. Ondanks de geïnduceerde supergeleidende ordeparameter is er geen excitatiekloof. Het optreden van "gapless superconductivity" kan spectroscopisch worden gemeten.

In het laatste hoofdstuk van dit proefschrift beschouwen we een geheel ander type wisselwerkend systeem zonder wanorde, dit in tegenstelling tot het wanordelijke SYK-model. De wisselwerking komt voort uit de koppeling van N Josephson-juncties aan fotonen in een microgolfresonator. De lage energietheorie van het systeem blijkt een gegeneraliseerde Dicke Hamiltoniaan te zijn van N deeltjes met spin $1/2$ die elkaar afstoten. We gebruiken een zogenaamde Holstein-Primakoff-representatie voor de totale spin van de N deeltjes, waarmee we een eerste orde fase-overgang in de grote-N-limiet kunnen vaststellen.

Curriculum Vitæ

I was born on the 16th of September 1991 in Novosibirsk, Russia. I went to primary school there, but in 2001 my family moved to Moscow, where I attended middle and high school.

In 2008 I entered the Faculty of Theoretical and Experimental Physics of the Moscow Engineering Physics Institute (State University). I was studying at the Department of Theoretical Nuclear Physics, where I completed my bachelor (2012) and master (2014) theses under the supervision of Dr. E. E. Saperstein from the Kurchatov Institute. After my undergraduate studies, I joined the Laboratory of Many-Particle Systems in the Kurchatov Institute as a part-time researcher. During my master's I worked on spectral properties of finite Fermi systems combining field theoretical and density functional approaches.

In 2015 I started my Ph.D. studies at the University of Leiden in the Theoretical Nanophysics group led by Prof. Dr. C. W. J. Beenakker. I investigated the transport properties of topological superconductors and graphene superlattices. Another direction of my research is transport signatures of the absence of quasiparticles in low-dimensional systems. I was also actively collaborating with Prof. Dr. S. I. Mukhin from the Moscow Institute of Steel and Alloys (State University) on the light-matter interactions with infinitely coordinated potentials. The results of my research are presented in this thesis.

During my Ph.D. studies, I presented my research in The Netherlands, Germany, Spain, and France. I was a teaching assistant for several courses: Quantum Mechanics I, Superconductivity, and Introduction to Solid State Physics.

After finishing the Ph.D., I am moving to the Department of Physics of Yale University to join the group of Prof. Dr. L. I. Glazman as a postdoc.

List of Publications

[1] N. V. Gnezdilov and E. E. Saperstein. *Calculation of double mass differences for near-magic nuclei on the basis of a semimicroscopic model.* JETP Lett. **95**, 603 (2012).

[2] N. V. Gnezdilov, I. N. Borzov, E. E. Saperstein and S. V. Tolokonnikov. *Self-consistent description of single-particle levels of magic nuclei.* Phys. Rev. C **89**, 034304 (2014).

[3] N. V. Gnezdilov, E. E. Saperstein and S. V. Tolokonnikov. *Spectroscopic factors of magic and semimagic nuclei within the self-consistent theory of finite Fermi systems.* EPL **107**, 62001 (2014).

[4] N. V. Gnezdilov, B. van Heck, M. Diez, J. A. Hutasoit, and C. W. J. Beenakker. *Topologically protected charge transfer along the edge of a chiral p-wave superconductor.* Phys. Rev. B **92**, 121406(R) (2015) [Chapter 3].

[5] E. E. Saperstein, M. Baldo, N. V. Gnezdilov, and S. V. Tolokonnikov. *Phonon effects on the double mass differences in magic nuclei.* Phys. Rev. C **93**, 034302 (2016).

[6] N. V. Gnezdilov, M. Diez, M. J. Pacholski, and C. W. J. Beenakker. *Wiedemann-Franz-type relation between shot noise and thermal conduction of Majorana surface states in a three-dimensional topological superconductor.* Phys. Rev. B **94**, 115415 (2016) [Chapter 2].

[7] O. V. Gamayun, V. P. Ostroukh, N. V. Gnezdilov, İ. Adagideli and C. W. J. Beenakker. *Valley-momentum locking in a graphene superlattice with Y-shaped Kekulé bond texture.* New Journal of Physics **20**, 023016 (2018).

[8] S. I. Mukhin and N. V. Gnezdilov. *First-order dipolar phase transition in the Dicke model with infinitely coordinated frustrating interaction.* Phys. Rev. A **97**, 053809 (2018) [Chapter 8].

[9] C. W. J. Beenakker, N. V. Gnezdilov, E. Dresselhaus, V. P. Ostroukh, Y. Herasymenko, İ. Adagideli, and J. Tworzydło. *Valley switch in a graphene superlattice due to pseudo-Andreev reflection.* Phys. Rev. B **97**, 241403(R) (2018), [Editors' Suggestion] [Chapter 4].

[10] N. V. Gnezdilov, J. A. Hutasoit, and C. W. J. Beenakker. *Low-high voltage duality in tunneling spectroscopy of the Sachdev-Ye-Kitaev model.* Phys. Rev. B **98**, 081413(R) (2018) [Chapter 5].

[11] N. Gnezdilov, A. Krikun, K. Schalm, and J. Zaanen. *Isolated zeros in the spectral function as signature of a quantum continuum.* Phys. Rev. B **99**, 165149 (2019) [Chapter 6].

[12] N. V. Gnezdilov. *Gapless odd-frequency superconductivity induced by the Sachdev-Ye-Kitaev model.* Phys. Rev. B **99**, 024506 (2019) [Chapter 7].